# PROGRESS TOWARDS A MEASUREMENT OF THE ELECTRON'S ELECTRIC DIPOLE MOMENT USING THE EDM$^3$ METHOD

ZACHARY CORRIVEAU

A Dissertation Submitted To The Faculty of Graduate Studies In Partial Fulfillment Of The Requirements For The Degree Of

Doctor Of Philosophy

Graduate Program in Physics and Astronomy
York University
Toronto, Ontario
June 2025

# ABSTRACT

This dissertation reports the progress made towards measuring the electron's electric dipole moment ($d_e$) using a novel method dubbed the Electric Dipole Measurements using Molecules within a Matrix (EDM$^3$) method, first proposed by the EDM$^3$ collaboration in Ref. [1]. The measurement of a non-zero value of $d_e$ has long been sought after as a measure of charge-parity violation, a phenomenon necessary to explain the observed asymmetry of matter and antimatter in the universe.

This work presents the production of a beam of cold barium monofluoride (BaF) molecules using a buffer-gas-cooled laser-ablation source and the subsequent implantation of BaF molecules into neon solids suitable for use in a measurement of $d_e$. Identification of several electronic and vibrational excited states of BaF within a neon matrix is demonstrated and the characteristics of these states are studied. The rate of the excitation for BaF molecules excited to the $B^2\Sigma_{1/2}(v = 0)$

state is determined and this result is used to estimate a density of BaF molecules of $N_{\text{total}} \geq (5 \pm 3) \times 10^{10}/\text{mm}^2$, which is near the targeted value for a first measurement of $d_e$.

Preliminary experiments demonstrate optical pumping of the embedded BaF molecules with circularly-polarized light. Further experiments show that the hyperfine structure of the ground state can be directly targeted using radio-frequency (RF) pulses that transfer population between the hyperfine states of the $X^2\Sigma_{1/2}(v = 0)$ ground state. These RF experiments show that population in the $F = 0, m_f = 0$ sublevel of the ground state can be maintained for times on the order of 3 ms in a neon matrix held at 5.8 K.

With the results demonstrated in this work, the remaining task prior to a measurement of the electron's electric dipole moment using the EDM$^3$ method will be to demonstrate precession and observe the coherence time associated with the solids produced. Further purification of the molecular beam will be necessary to reach the desired precession times of $t_p \geq 10$ ms. Improvements to the apparatus are underway

by the EDM$^3$ group and their completion could remove the last barriers to a measurement of $d_e$.

*Dedicated to Kilborn "Kibby" Lutz.*

*1958 – 2025*

# ACKNOWLEDGEMENTS

Firstly, I would like to thank my supervisor Eric Hessels for the opportunity to be a part of this research group and of the EDM$^3$ collaboration. There never seemed to be a problem for which he could not give an insightful idea or thoughtful advice towards resolving. I feel truly honoured to have been able to study physics under his guidance.

I would like to thank Daniel Heinrich, who during the years spent with our group as a postdoctoral fellow was an integral part of the design and implementation of the experiments reported in this work.

I would also like to thank Ricardo Lambo, our current postdoctoral fellow, who is an invaluable driving force behind the research performed by the group with his many hours working in the laboratory, analysis of data obtained, and for providing our group with his expertise in matrix isolation

experiments.

I would like to thank my fellow graduate students: Jorge Perez-Garcia, Hin-Man Yau, and Neil McCall. All of them have helped ensure the continuous advancement of the research towards our shared measurement goal and have made the laboratory a fun place to work.

I would like to thank Matthew George who, since the very beginning of this project, has always made time to come visit the laboratory and provide advice on the many problems that have been encountered over the years.

I would like to thank Greg Koyanagi for his advice and insight on the many engineering problems that arise when building the infrastructure and instrumentation needed to support this experiment and for the important reminder on the need for diligence when conducting research.

I would like to thank Cody Storry for his many contributions to the experiment. His expertise with the design and implementation of cryogenic systems has helped move our

research forward immensely.

I would like to thank all remaining members of the EDM$^3$ collaboration. A project of this scale would not be possible without the dedication of the many collaborative researchers and theorists who have progressed this project over the years.

Thank you to my parents Jill and Kibby; and Fernand and Brigitte who have all supported me and helped me to become the person that I am today.

Most importantly, I would like to thank my wife Anne. Without her support during both undergraduate and post-graduate studies I would not have been able to complete this work. In particular, I would like to thank her for her patience during the many hours I have spent hiding away, writing and refining this dissertation.

# CONTENTS

# LIST OF TABLES

# LIST OF FIGURES

# 1 INTRODUCTION

## 1.1 MOTIVATION

### 1.1.1 *The Standard Model*

The Standard Model (SM) of physics is a theory of all known elementary particles and their relation to the fundamental forces (excluding gravity) that mediate the interactions between them. This modern theory of fundamental physics has been very successful in making predictions on the properties, and even the very existence, of particles which can then be tested experimentally. However, fundamental questions pertaining to the nature of the observable universe remain unanswered. Chief among these are the nature of dark matter and of dark energy, and the apparent matter/antimatter asymmetry that persists in the observable universe. The SM is inadequate for answering these questions; thus the search for

new physics to extend the model is ongoing. These extended theories are labelled with the catch-all moniker: beyond-the-Standard-Model (BSM) theories of physics. Fundamentally the search for an electron electric dipole moment (eEDM) is a test for new BSM physics and, in particular, a search for a possible solution to the problem posed by the imbalance of the quantities of matter/antimatter in the universe–a problem known as baryogenesis. To better understand the relation of the eEDM to matter and antimatter asymmetry, the widely-held axiom of physics known as charge-parity-time (CPT) invariance is examined in the following subsection.

### 1.1.2 *Charge, parity, and time symmetries*

In the realm of particle physics, there are three known and discrete symmetries of great importance: that of charge conjugation (C; the transmutation of a particle into its antiparticle counterpart), parity transformation (P; the act of inverting all spatial coordinates), and time reversal (T; a transformation which reverses the arrow of time). The product of these three transformations leads to CPT symmetry. CPT-invariance is

strongly believed to be preserved for all physical processes and systems. A violation of CPT-invariance would cause the breakdown of Lorentz invariance in current quantum field models [2].

Up until the 1950s it was thought that all physical processes were invariant under all three transformations separately. In 1956, it was realized [3] that parity can be violated by processes mediated by the weak force. In 1957, an experiment was performed [4] in which P-symmetry was found to be violated while studying the beta decay of nuclear-spin-polarized $^{60}$Co. It was also noted [5] in this experiment that C-symmetry was broken. However, both CP- and T-invariance still held.

### 1.1.3 *The Sakharov conditions*

While physicists explored the ramifications of these symmetries and the violation of the various combinations of them, Sakharov stipulated [6] three conditions that must have been satisfied in the early universe in order to achieve the imbalance of particles and antiparticles that is observed today. The three conditions are:

1. Baryon number is not conserved.

2. A strongly CP-violating process must exist to generate a baryon surplus.

3. There existed a time period during which the universe was not in thermal equilibrium such that, even in a dense universe, newly created particles and antiparticles did not simply annihilate.

It is the search for processes that satisfy the second condition that inspires experiments to detect an eEDM larger than predicted by the SM.

The SM does provide observable CP-violating processes, notably encapsulated in the Cabbibo-Kobayashi-Maskawa (CKM) matrix, which describes [7] the flavour-changing decay of freely-propagating quarks. This CP-violating process may seem to be encouraging for a within-the-Standard-Model explanation of the second Sakharov condition; however, after careful study, it has been found [8] that the these processes are far too small to explain the asymmetry of matter and antimatter that is observed today.

### 1.1.4 *The electron's electric dipole moment as a CP-violating quantity*

The idea of testing fundamental particles for an electric dipole moment began in 1950 in a brief letter [9] penned by Purcell and Ramsey. In this letter, Purcell and Ramsey note that if such a moment were to exist it would be odd under parity inversion. The Hamiltonian of an elementary particle with both magnetic and electric dipole moments can be written as

$$H = -(\vec{\mu} \cdot \vec{B} + \vec{d} \cdot \vec{E}). \tag{1.1}$$

Here, both the magnetic dipole moment $\vec{\mu}$ and the electric dipole moment $\vec{d}$ must be directed along the axis of the particle's spin angular momentum $\vec{S}$, therefore Eq. (1.1) can be equivalently expressed as:

$$H = -(\mu\vec{S} \cdot \vec{B} + d\vec{S} \cdot \vec{E})/|\vec{S}|. \tag{1.2}$$

Table 1.1 summarizes the result of applying charge-conjugation, parity-inversion, and time-reversal transformations to each term in Equation 1.2 (where $+$ denotes an even quantity under a given transformation and $-$ denotes an odd quan-

| | C | P | T | CP | CPT |
|---|---|---|---|---|---|
| $\mu\vec{S}$ | $-$ | $+$ | $-$ | $-$ | $+$ |
| $d\vec{S}$ | $-$ | $+$ | $-$ | $-$ | $+$ |
| $\vec{B}$ | $-$ | $+$ | $-$ | $-$ | $+$ |
| $\vec{E}$ | $-$ | $-$ | $+$ | $+$ | $+$ |
| $\mu\vec{S}\cdot\vec{B}$ | $+$ | $+$ | $+$ | $+$ | $+$ |
| $d\vec{S}\cdot\vec{E}$ | $+$ | $-$ | $-$ | $-$ | $+$ |

Table 1.1: CPT transformations on the electron's Hamiltonian. A summary of the effect of charge-conjugation, parity-inversion, and time-reversal transformations on a particle described by Equation 1.2. Because $\mu\vec{S}\cdot\vec{B}$ is even under all three transformations, charged particles with spin and magnetic moments are not inherently CP-violating quantities. However, the electric dipole moment term $d\vec{S}\cdot\vec{E}$ is even $(+)$ under charge conjugation and odd $(-)$ under both parity inversion and time reversal. All terms of the Hamiltonian are CPT invariant.

tity) to show that the addition of the second term ($d\vec{S} \cdot \vec{E}/|\vec{S}|$) introduces a CP-violating contribution. An elementary particle with only a magnetic dipole moment has no such CP-violating contribution. The Hamiltonian of an elementary particle is CPT invariant regardless of the inclusion of a electric dipole moment term.

## 1.2 REQUIRED PRECISION

### 1.2.1 *Current best measurements of the electron's electric dipole moment*

The most precise measurement of $d_e$ is performed by the JILA collaboration, who measured [10] a value of $d_e = (-1.3 \pm 1.4) \times 10^{-30} e$ cm, placing a 90% confidence upper bound on the magnitude of $d_e$ of

$$|d_e| \leq 4.1 \times 10^{30} e\ cm. \tag{1.3}$$

This impressive measurement already excludes a vast array of BSM theories. However, the possible gain in precision from the EDM$^3$ method presents an opportunity to achieve a

measurement which could further test BSM theories and thus guide the course of theoretical understanding of the universe.

### 1.2.2 *The expected value of the electron's electric dipole moment*

To the best of current knowledge, the electron behaves as a point particle, yet it is not expected that the electron's charge distribution (if the cloud of virtual particles that surround it are included) is perfectly spherical in nature and an electric dipole moment is predicted. Using the SM, calculations have been performed which predict [11] the magnitude of the electron's electric dipole moment to be

$$d_e \approx 10^{-35} e\ cm, \tag{1.4}$$

owing to CP-violation associated with the CKM matrix. Previous calculations of CP-violating processes within the SM predicted [12] orders of magnitude smaller values for $d_e$. Although Equation 1.4 is still far too small for current sensitivities of experimental measurements, it provides a useful floor for which to compare BSM theories not excluded by the current experimental sensitivity. These BSM theories predict [13–15] much larger $d_e$ values. The values predicted depend

on the precise BSM theory, but are generally orders of magnitude larger than the SM prediction. This tension between SM and BSM theories, creates an environment in which improved experimental determinations are of utmost interest, as a measured value of $d_e$ could severely constrain the class of theories that accurately describe the observed universe.

### 1.2.3 *The feasibility of a measurement of $d_e$*

A measurement of the electron's electric dipole moment has been performed by many groups since the search for larger CP-symmetry-violating processes began. Precision has steadily, though perhaps slowly, increased as the experimental techniques and technologies behind such measurements have improved. Figure 1.1 shows the upper bound placed on the magnitude of $d_e$ by various measurements performed in the last thirty years.

The most precise $d_e$ determinations come from measurements using polar molecules or molecular ions. The large internal electric fields within these molecules provides increased sensitivity for measurements of $d_e$ (compared to experiments using atoms). This fact is further discussed in

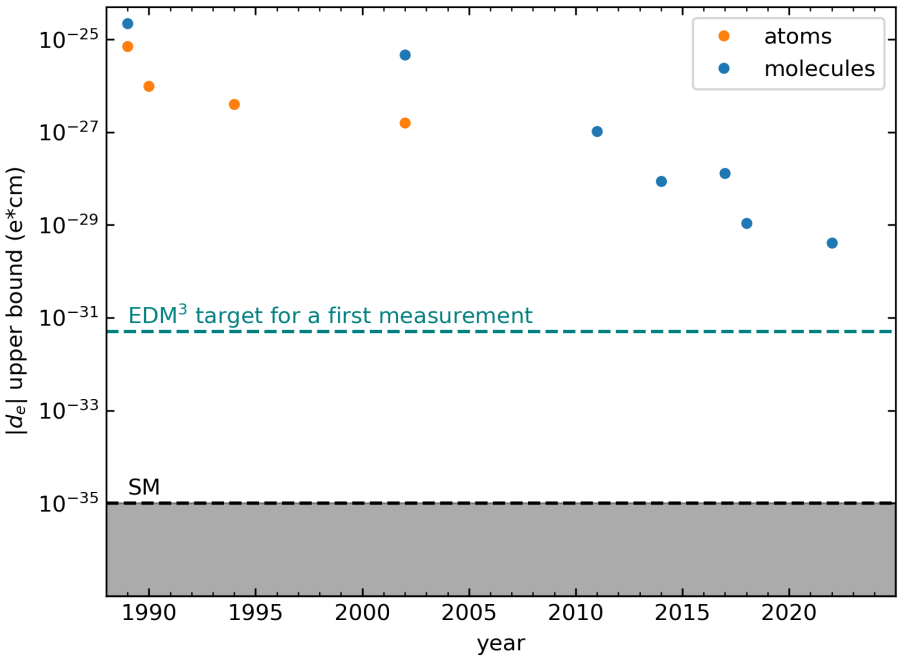


Figure 1.1: Results from selected measurements of the electron's electric dipole moment. The implied upper bounds are based on data taken from Refs. [10, 16–25]. Measurements using molecules and those using atoms are shown in different colours. The SM value is taken from the calculations performed in Ref. [11]. Note that the y-axis is presented on a logarithmic scale.

Section 1.3.1. Molecular beam experiments, such as the experiments of the ACME collaboration [16] and the group from Imperial College London [19], send a group of polar molecules down a designated path where their states are prepared and made to precess for some time ($t_p \approx 1$ ms for the ACME experiment) before being probed to extract phase shifts in precession due to the presence of $d_e$. Molecular-beam experiments have a limited precession time and require a homogeneous magnetic field over a large volume.

The molecular-ion experiment of the JILA collaboration [10] uses ions confined within an ion trap to increase the precession time (the JILA experiment has precession times of $t_p \approx 1$ s). However ion-trap experiments are limited in the density of ions that may be confined, ultimately limiting the number of electrons that may be studied.

### 1.2.4 *Statistically-limited precision*

To better understand the limiting precision of a measurement of $d_e$, the uncertainty that a statistically-limited measurement of $d_e$ would yield is examined. The ultimate uncertainty ($\delta d_e$)

of any statistically-limited measurement (i.e., the case where systematic uncertainties are controlled below the level of this intrinsic uncertainty) is given by

$$\delta d_e = \frac{\hbar}{2\mathcal{E}_{\text{eff}} t_p \sqrt{N}}, \tag{1.5}$$

where N is the number of electrons studied, $t_p$ is the precession time, and $\mathcal{E}_{\text{eff}}$ is the effective electric field seen by the electron. Equation 1.5 implies it is imperative to design experiments which maximize $\mathcal{E}_{\text{eff}}$, N, and $t_p$.

### 1.2.5 *Improvements required to increase the precision of a measurement of $d_e$*

The most precise measurements to date [10, 16, 19] have all managed to control the systematic uncertainties to below the level of the statistical uncertainty of Equation 1.5. Table 1.2 shows the approximate values, for each quantity in Eq. 1.5, on which $\delta d_e$ ultimately rests in each experiment and provides a comparison for the corresponding value that may be achieved in an initial measurement using the EDM$^3$ method. In Section 1.3.6 the EDM$^3$ method is described in greater

detail and in Section 1.3.7 the presented values are motivated as reasonable estimates of precision.

## 1.3 THE EDM$^3$ METHOD

The EDM$^3$ method was first proposed by the EDM$^3$ collaboration in 2017 [1] and sought to reduce both statistical and systematic uncertainties in a measurement of $d_e$. It proposes using a novel method of trapping the electrons that are to be studied in two nested layers. The first layer, as with other modern eEDM measurements, is within polar molecules, giving the benefit of large effective electric fields experienced by the valence electron within the molecule. The second is to confine the molecules within trapping sites in a cryogenic crystal lattice. This lattice is composed of an inert-gas solid, which has only a limited effect on the local environment of the trapped molecules. This limited effect on the molecule means that experiments on polar-molecules within inert-gas matrices are similar to measurement methods which use free polar-molecules, with the additional benefit that the polar-molecules within a matrix are stationary and have a fixed orientation. Additionally inert-gas solids, as their name sug-

| Collaboration | $\mathcal{E}_{\text{eff}}$ / $(\frac{GV}{cm})$ | $t_p$ / (ms) | N | Ref. |
|---|---|---|---|---|
| ACME (actual) | 78 | 1 | $10^{12}$ | [16] |
| JILA (actual) | 23 | 3,000 | $10^{8}$ | [10] |
| EDM$^3$ (initial goal) | 6 | 10 | $10^{15}$ | |

Table 1.2: Values from which statistical uncertainties for $d_e$ measurements are derived. The first two rows are the values achieved in recent experiments, while the third row is the estimate from the EDM$^3$ collaboration for a potential first measurement. As in Eq. (1.5), $\mathcal{E}_{\text{eff}}$ is the effective field the electron experiences, $t_p$ is the precession time of the measurement, and N is the number electrons studied.

gests, have the benefit of being chemically inert, allowing for the confinement of radical polar molecules. These solids are transparent to light within the visible and near-infrared spectrum, which allows for laser spectroscopy experiments on the confined molecules.

For this work the radical polar molecule chosen is barium monofluoride (BaF). The motivations for this choice of molecule are discussed in Section 1.3.2. Neon is chosen as the inert-gas host matrix (although argon has also been considered [26, 27] by the EDM$^3$ collaboration).

### 1.3.1 *Polar molecules and the fields within them*

Because the goal of the EDM$^3$ method is to trap an ensemble of electrons and probe their electric dipole moments, it is important to properly motivate why molecules in a matrix are suitable to measurements of $d_e$. Although it is possible to trap atoms within inert-gas matrices and such systems have been the subject of experiments probing the properties of confined atoms [28–33], atomic systems have several drawbacks in comparison to their molecular counterparts. Atoms

lack the large internal electric field that is intrinsic to polar molecules and therefore an externally applied electric field is necessary to observe the electron's electric dipole moment in an experiment. Certain atomic candidates, such as cesium, introduce electric dipole moment enhancement factors of on the order of 100 [34], which aid in the detection of $d_e$; however, considering that electric fields created within the laboratory are limited to on the order of 10 kV/cm, even atoms with these large enhancement factors are far less sensitive than experiments performed on electrons within polar molecules. The effective electric field experienced by the electron within a well-chosen polar molecules is on the order of 10 GV/cm, which leads to several orders of magnitude larger sensitivity compared to atomic experiments. Large externally applied electric fields contribute to the systematic uncertainty of eEDM measurements and so the elimination of this external field (as is possible for matrix-isolated molecules) also eliminates a significant potential systematic effect.

Once embedded within the matrix, polar molecules are firmly locked in place, with librator states replacing the free-molecule rotational states. Theoretical understanding of li-

brator states within inert-gas matrices has been studied by others [35–38]. The additional confinement experienced by the molecules is ideal, as the measurement of the electron's electric dipole moment requires that the molecules be fixed in orientation with respect to the magnetic field. With fixed molecule orientation, the EDM$^3$ collaboration plans to selectively address molecules oriented in directions where the effective electric field experienced by the electron is either approximately aligned or counter-aligned to the applied magnetic field (as will be described in Section 1.3.6).

### 1.3.2 *BaF as a choice of polar molecule*

The polar molecule chosen for a measurement of $d_e$ must have one unpaired electron whose spin will be allowed to precess. Preferably, this electron will be as close as possible to a heavy nucleus so that the effective electric field is maximized. A molecule with a heavy nucleus and an unpaired valence electron in an s-orbital is the ideal candidate. Such molecules typically tend to be chemically reactive and therefore are more difficult to prepare. However, laser-ablation techniques

are able to produce large quantities of these molecules.

Table 1.3 shows a list of some candidate molecules that have been considered for a measurement of $d_e$. From this list of polar molecules BaF has been chosen as the molecule for a first measurement of $d_e$ using the EDM$^3$ method. Although it is tempting to focus solely on the effective electric field ($\mathcal{E}_{\text{eff}}$), due to its direct relation to the statistically-limited uncertainty on a measurement of $d_e$ (see Equation 1.5), there are other practical factors in assessing polar-molecule candidates.

The $^{138}$Ba and $^{19}$F isotopes have nuclear spins of 0 and $\frac{1}{2}$, respectively. For the electronic ground state $X^2\Sigma^+$, this total nuclear spin of 1/2, along with the 1/2 spin from the unpaired electron creates a four-level hyperfine structure. This structure has been precisely measured [44–47]. The BaF molecule has several electronic transitions which can be laser-excited with near-infrared laser radiation; a wavelength range that is accessible with readily-available lasers. The accessibility of these electronic transitions enables and facilitates control of the molecule using well-established spectroscopic

| Molecule | $\mathcal{E}_{\text{eff}}$ ($\frac{GV}{cm}$) | Ref. |
|---|---|---|
| CaF | 0.28 | [39] |
| SrF | 2.2 | [39] |
| BaF | 6.5 | [39] |
| YbF | 23 | [40] |
| RaF | 52 | [41] |
| ThO | 55 | [42] |
| HgI | 109 | [39, 43] |
| HgBr | 109 | [39, 43] |
| HgCl | 114 | [39, 43] |
| HgF | 116 | [39, 43] |

Table 1.3: A list of molecules considered for an eEDM measurement. Their effective electric fields ($\mathcal{E}_{\text{eff}}$) are calculated in the specified references. Each molecule contains an unpaired electron which would be allowed to precess in a measurement of $d_e$.

techniques. Additionally, the structure of BaF is calculable [48–51] and the molecule is extensively studied [52–58].

### 1.3.3 *Neon as a host matrix*

Although solids such as gadolinium-iron garnet and gadolinium-gallium garnet [59, 60] have previously been used to study the electron electric dipole moment, a cryogenic neon matrix has several advantages. A cryogenic neon matrix is optically transparent and allows for laser excitation and induced fluorescence to be observed for BaF molecules within the matrix. The neon matrix also exerts minimal influence on the BaF molecules due to the relatively large separation between the neon atoms in the lattice (neon matrices have a lattice constant of 4.5 Å [61]), meaning only relatively small perturbations to the molecular structure must be studied and understood. Because of the trapped BaF molecule's similarity to its free counterpart, a measurement for the matrix-isolated molecule is similar to that of beam-line experiments utilizing free molecules. However, BaF molecules confined within a neon matrix are stationary, oriented by the matrix, and can be highly concentrated (compared to the density in molecular

beams or ion traps).

There are three stable isotopes of neon: $^{20}$Ne,$^{21}$Ne, and $^{22}$Ne (with approximately 90%, 0.25%, and 9.3% natural abundances [62], respectively). To ensure uniformity of the lattice spacing of the cryogenic matrix, it is ideal to use isotopically pure $^{20}$Ne (the most abundant isotope), eliminating any distortion caused by the presence of the heavier neon atoms. Additionally, $^{21}$Ne has a magnetic moment [63] and this magnetic moment will distort the magnetic field for nearby BaF molecules, reducing the maximum possible precession time ($t_p$) for a measurement of $d_e$. A phase diagram for pure $^{20}$Ne is presented in Figure 1.2, which demonstrates the suitability of $^{20}$Ne as a host matrix based on its phase boundaries. The system presented in this work allows for matrices cooled below 7 K to be held and probed continually for months with virtually no loss due to sublimation.

### 1.3.4 *Assembly of a BaF-doped neon matrix*

Both the properties of inert-gas matrices [61, 65, 66] and the atoms or molecules [28, 30, 67–69] that have been confined

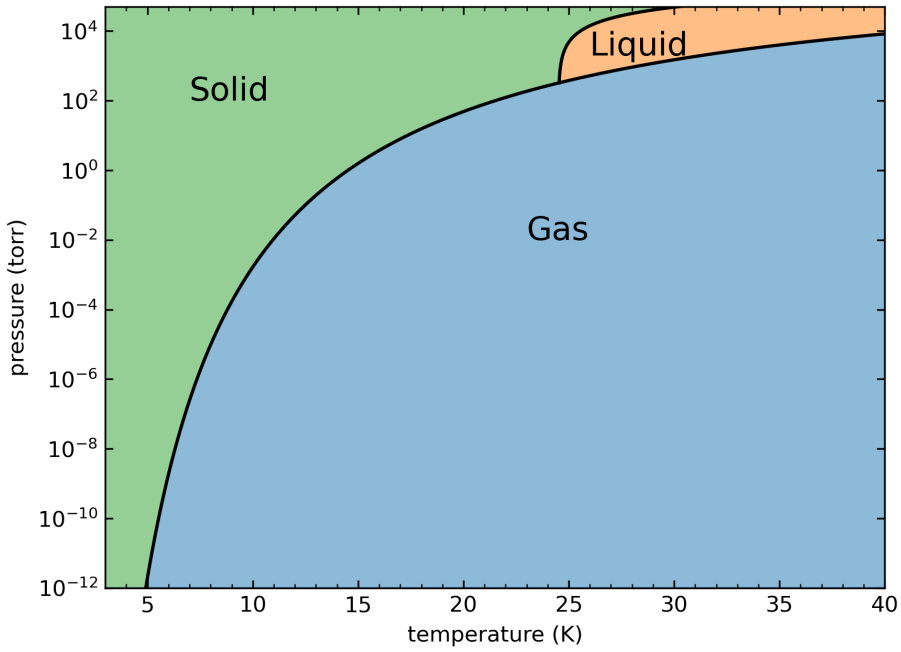


Figure 1.2: Phase diagram for pure $^{20}$Ne. The diagram spans the pressure and temperature regimes of interest to the EDM$^3$ collaboration. The y-axis has a logarithmic scale. The diagram was constructed by using properties of neon detailed in Ref. [64]. The three phases present are shaded individually and labelled. The triple point of neon is located at the intersection of the phase transition lines.

within them have been extensively studied and these previous studies are used as a guide for the research conducted in this work. Vapour deposition of neon gas in the presence of a small stream of BaF molecules onto on a cryogenic surface is used to form the solids presented in this work.

The adjustment of vapour-deposition parameters allows the neon-solid growth to be controlled precisely. After growth, annealing is performed on the assembled solid, which allows for the neon atoms and BaF molecules in the matrix to resettle into energetically-favourable sites (similar to the process observed for atoms in inert-gas matrices [31]). Annealing in this manner helps to reduce the differences in trapping environments produced during the growth process.

Solid neon has a number density of $4.5 \times 10^{19}$ neon atoms per $mm^3$. Thus, even at a BaF:Ne dilution of 1 ppb, the number of trapped BaF molecules within a 1 $mm^3$ volume of neon matrix is $N = 4.5 \times 10^{10}$. The low density of BaF molecules within the matrix, will help to ensure that they see only small magnetic fields from the other BaF molecules, leading to longer possible coherence times.

### 1.3.5 *Measurement process*

Measurements of the electric dipole moment of the electron are performed by observing the precession of electron spins within prepared ensembles. This precession is affected by both the coupling of a magnetic field to the electron spin and the coupling of an electric field to the electric dipole moment. The angle of precession is given by

$$\phi_p = \frac{(g\mu_B \vec{B} \cdot \vec{S} \pm d_e \vec{\mathcal{E}}_{\text{eff}} \cdot \vec{S}) t_p}{\hbar |\vec{S}|}, \tag{1.6}$$

where $\vec{S}$ is the electron spin, $\vec{B}$ is the applied magnetic field, $g\mu_B$ is the magnetic moment of the electron, $\vec{\mathcal{E}}_{\text{eff}}$ is the effective electric field within the molecule that the electron is subjected to, $t_p$ is the precession time for the electron, and $d_e$ is the electric dipole moment of the electron. In the case of aligned and counter-aligned $\vec{B}$ and $\vec{\mathcal{E}}_{\text{eff}}$, Equation 1.6 becomes

$$\phi_p = (g\mu_B B \pm d_e \mathcal{E}_{\text{eff}}) t_p / \hbar. \tag{1.7}$$

The sign in Equation 1.7 shows the cases in which the electric and magnetic fields are aligned (+) and counter-aligned (−).

In Section 1.3.6 it is discussed how the EDM$^3$ method exploits the differing rates of precession caused by aligned and counter-aligned magnetic and electric fields to engineer a measurement that is sensitive to the effect of $d_e$ (the second term in Equation 1.7), but not sensitive to $\mu_B$ (the first term in Equation 1.7).

### 1.3.6 *Time sequence for an EDM$^3$ measurement*

A proposed time sequence for an eEDM measurement using the EDM$^3$ method is shown in Figure 1.3. These steps are also discussed in Ref. [26], where it was first proposed as a method of measuring the electron's electric dipole moment using BaF molecules in an argon host matrix.

The four states that make up the hyperfine structure of the $X^2\Sigma^+_{1/2}(v = 0)$ ground state of BaF are shown as the four lowest energy levels in each panel of Figure 1.3. The total nuclear spin of the molecule is $I = 1/2$ and combines with the electron spin of $S = 1/2$ causing the electronic ground state $X^2\Sigma_{1/2}$ to have a four-level hyperfine structure with quantum numbers $F = 0, m_f = 0$ and $F = 1, m_f = \pm 1$. To

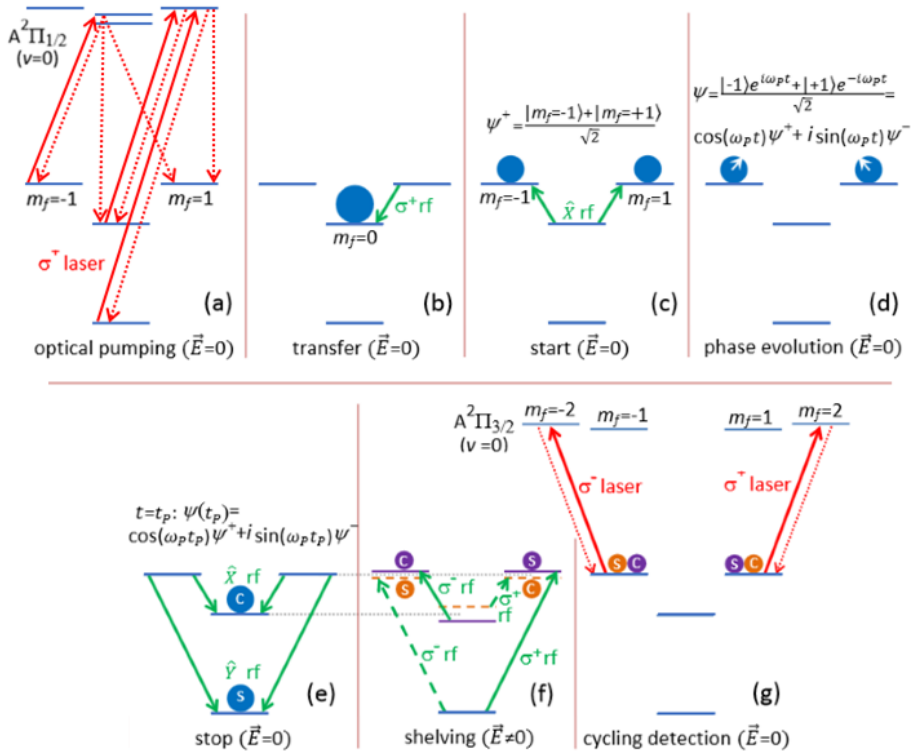


Figure 1.3: Proposed sequence to perform a measurement of the electron's electric dipole moment. Modified from Ref. [26]. The BaF molecules are prepared in steps (a) - (c) using optical and RF transitions. In step (d), the phases of the two components of $\psi$ evolve for time $t_p$. In steps (e) and (f), the molecules are selected, based on orientation, and prepared for detection. Finally, the molecules are detected in (g) using cycling transitions using the $A^2\Pi_{3/2}(v = 0)$ state.

the extent that the BaF molecule has its orientation fixed by the matrix it only has azimuthal symmetry and the Hamiltonian commutes with $F_z$ (making it a good quantum number), while it does not commute with $F^2$ (allowing for a mixture between the $F = 0, m_f = 0$ state and the $F = 1, m_f = 0$ state). Because this mixing is small these states are still referred to using the $F = 0$ and $F = 1$ labels. It is this mixture that leads to the energy difference between the $F = 1, m_f = 0$ state and the $F = 1, m_f = 0, \pm 1$ states shown in Figure 1.3. The $A^2\Pi_{1/2}(v = 0)$ state similarly has four hyperfine levels, also shown in Figure 1.3.

The steps required for performing a eEDM measurement are shown in (a) through (g) of Figure 1.3. In (a) the BaF molecules are optically pumped using a laser excitation from the electronic ground state, $X^2\Sigma^+_{1/2}(v = 0)$, to the electronically excited $A^2\Pi_{1/2}(v = 0)$ state using $\sigma_+$-polarized laser light. As the molecules are excited by the laser light, they gain $\Delta m_f \hbar = +\hbar$ of angular momenta and eventually the molecular population is transferred to the $X^2\Sigma_{1/2}(F = 1, m_f = 1)$ state, where the BaF molecules are no longer accessible to

laser excitation.

Figure 1.3 (b) shows the use of a $\pi$-pulse to transfer the BaF molecular population from the $F = 1, m_f = 1$ sublevel to the $F = 1$, $m_f = 0$ sublevel using $\sigma_+$-polarized RF radiation. This step is immediately followed by step (c) which uses an $\hat{X}$-polarized RF $\pi$-pulse to place the molecules into an even superposition of the $m_f = \pm 1$ states:

$$|\psi^+\rangle = \frac{|m_f = -1\rangle + |m_f = +1\rangle}{\sqrt{2}} \tag{1.8}$$

(Alternatively a $\hat{Y}$-polarized RF pulse could be used to transfer the population into an odd superposition of the $m_f = \pm 1$ states:

$$|\psi^-\rangle = \frac{|m_f = -1\rangle - |m_f = +1\rangle}{\sqrt{2}}). \tag{1.9}$$

After the BaF molecules are prepared into this superposition of states, step (d) in Figure 1.3 shows how the system evolves freely in the presence of the applied magnetic

field with the total time-dependent wavefunction during this quantum-mechanical phase progression described by

$$|\psi(t_p)\rangle = \frac{|m_f = -1\rangle e^{i\omega_p t_p} + |m_f = +1\rangle e^{-i\omega_p t_p}}{\sqrt{2}}, \quad (1.10)$$

or, equivalently,

$$|\psi(t_p)\rangle = cos(\omega_p t_p)|\psi^+\rangle + i\, sin(\omega_p t_p)|\psi^-\rangle. \quad (1.11)$$

Here

$$\omega_p^{\pm} = (g\mu_B B \pm d_e \mathcal{E}_{\text{eff}})/\hbar \quad (1.12)$$

is the angular frequency of precession due to the magnetic and electric fields and is related to the angle of precession of Equation 1.7 by $\phi_p = \omega_p t$.

Step (e) of Figure 1.3 shows how the phase evolution is stopped after time $t_p$ by applying $\hat{X}$-polarized and $\hat{Y}$-polarized RF pulses which independently shelve the $|\psi^+\rangle$ and $|\psi^-\rangle$ components of $|\psi(t_p)\rangle$ into the two $m_f = 0$ states. After this step, the populations in the two $m_f = 0$ states are

$s \equiv sin^2(\omega_p t_p)$ and $c \equiv cos^2(\omega_p t_p)$.

Step (f) of Figure 1.3 shows the application of an electric field that causes a Stark shift in the hyperfine sublevels. These shifts for BaF molecules confined within a matrix have been calculated [26] and have a linear relation to the applied electric field $\Delta E_{\text{stark}} \propto \mathcal{E}_{\text{applied}}$. The sign of the shift is dependent on the orientation of the molecule (and therefore its electric dipole moment) relative to the applied electric field. This shift allows RF $\pi$-pulses to independently address BaF molecules which are aligned and those which are counter-aligned with respect to the magnetic field.

Figure 1.3 step (f) shows a series of four different RF pulses, all tuned to different Stark-shifted transitions, which serves to shelve the molecules according to their orientation. Molecules aligned with the magnetic field have the $|\psi_+\rangle$ component placed into the same $m_f = 1$ sublevel. The $|\psi_-\rangle$ component for molecules counter-aligned to the magnetic field is shelved in this same $m_f = 1$ sublevel. Similarly, the $|\psi_-\rangle$ component for molecules aligned with the magnetic field and the $|\psi_+\rangle$ component for counter-aligned molecules are placed in the

$m_f = -1$ sublevel. This selective placement of molecular populations allows for the extraction of the component of the phase evolution caused by $d_e$ from the observed fluorescence in step (g) of Figure 1.3.

Figure 1.3 (g) shows the optical cycling transition $X^2\Sigma_{1/2}(v = 0) \rightarrow A'\,^2\Pi_{3/2}(v = 0)$, which is used for detection. This transition has favourable Frank-Condon factors – returning $\approx 95\%$ of the population to the $X^2\Sigma_{1/2}(v = 0)$ state (with most of the remaining 5% going to the $X^2\Sigma_{1/2}(v = 1)$) – meaning every molecule will cycle, on average, 20 times (each time emitting a photon) before being lost to a higher-vibrational $X^2\Sigma_{1/2}$ state. With a fluorescence collection efficiency of 5%, this allows for detection with near unity efficiency (without the aid of any re-pump lasers to recapture the higher-vibrational populations).

As described above, step (f) of Figure 1.3 populates the $m_f = \pm 1$ states in a precise manner. The phase contribution from an electric dipole moment of the electron is added to the magnetic-dipole contribution when the magnetic field and the electric field are aligned (see Equation 1.7) and the phase

contributions subtract when the fields are counter-aligned. By tuning the magnetic field ($B$) and the precession time( $t_p$), $\phi_p$ can be set to

$$\phi_p^{\pm} = \omega_p^{\pm} t_p = 2\pi n + \frac{\pi}{4} + \delta_{\pm}, \tag{1.13}$$

where $\delta_+$ and $\delta_-$ are small. Here,

$$\delta_{\pm} = \delta_B \pm \delta_{\mathcal{E}} = \delta_B \pm d_e \mathcal{E}_{\text{eff}} t_p / \hbar, \tag{1.14}$$

where $\delta_B$ results from applying a slightly incorrect magnetic field, $\delta_{\mathcal{E}} = d_e \mathcal{E}_{\text{eff}} t_p / \hbar$ results from the electric dipole moment of the electron, and the $\pm$ refers to the molecules which are aligned and counter-aligned to the magnetic field. The desired information is contained entirely within $\delta_{\pm}$, and this information can be extracted by exploiting the relation of the even, odd, aligned, and counter-aligned molecular populations. Examining the even component of populations ($c_{\pm}$):

$$\begin{aligned} c_{\pm} &= cos^2 \omega_p^{\pm} t_p \\ &= \frac{1}{2}(1 + cos(2[2\pi n + \frac{\pi}{4} + \delta_{\pm}])) \\ &= \frac{1}{2}(1 - sin(2\delta_{\pm})) \\ &= \frac{1}{2} - \delta_{\pm} + \mathcal{O}(\delta_{\pm}^3). \end{aligned} \tag{1.15}$$

Similarly, the odd components give

$$s_{\pm} = \frac{1}{2} + \delta_{\pm} - \mathcal{O}(\delta_{\pm}^3). \tag{1.16}$$

The total populations that end up in the $m_f = +1$ sublevel of the ground state is

$$P_1 = f^+ c_+ + f^- s_-, \tag{1.17}$$

whereas

$$P_2 = f^- c_- + f^+ s_+ \tag{1.18}$$

is the total population in the $m_f = -1$ sublevel. Here, $f^{\pm}$ is the fraction of molecules oriented with their effective electric field aligned ($f^+$) and counter-aligned ($f^-$) with the magnetic field. The difference between the two populations is

$$\begin{aligned} P_1 - P_2 &= (f^+ c_+ + f^- s_-) - (f^- c_- + f^+ s_+) \\ &= 2f^- \delta_- - 2f^+ \delta_+ \\ &= 2f^-(\delta_B - \delta_{\mathcal{E}}) - 2f^+(\delta_B + \delta_{\mathcal{E}}) \\ &= 2\delta_B(f^- - f^+) - 2\delta_{\mathcal{E}}(f^- + f^+). \end{aligned} \tag{1.19}$$

In the approximation that the same fraction of BaF molecules are in both orientations (i.e., $f^+ = f^-$) the magnetic field term falls away from Equation 1.19 and what remains is a measurement that is only sensitive to $d_e$

$$P_1 - P_2 = -\frac{2d_e\mathcal{E}_{\text{eff}}t_p}{\hbar}. \tag{1.20}$$

However, it is not necessary to assume that $f^+ = f^-$. If a subsequent experiment is performed with an inverted magnetic field, the population difference for this new experiment is given by

$$P_1' - P_2' = -2\delta_B(f^- - f^+) - 2\delta_{\mathcal{E}}(f^- + f^+). \tag{1.21}$$

The sum of the population difference in Equation 1.19 and Equation 1.21 is

$$(P_1 - P_2) + (P_1' - P_2') = -\frac{4d_e\mathcal{E}_{\text{eff}}t_p}{\hbar}, \tag{1.22}$$

which gives a measurement of the electron's electric dipole moment that is insensitive to the magnetic field applied as well as being insensitive to the fractions $f^+$ and $f^-$.

### 1.3.7 *Targeted sensitivity for the EDM$^3$ method*

The systematic tests possible with the EDM$^3$ method should allow for the study and reduction of systematic effects with a goal of having the statistical limit of Equation 1.5 as the dominant uncertainty (similar to previous high precision measurements of $d_e$ [10, 16, 19]). In Section 1.3.8 the advantages of using the EDM$^3$ method for reducing systematic effects are discussed in greater detail.

To estimate a statistical uncertainty obtainable with the EDM$^3$ method, it is necessary to determine a reasonable estimate for each contributing quantity in Equation 1.5. In inert-gas solids, coherence times of order 100 ms have been observed [29, 32, 70] with times approaching 1 s for other solids [71]. Here, it is assumed that a precession time of $t_p = 10$ ms is possible for cryogenic neon cooled below 4 K for an initial measurement. Although the effective electric field in molecules cannot be directly measured, calculations have been performed by a number of groups for many polar molecules. The effective electric field for BaF has been calculated [39, 42] to be $\mathcal{E}_{\text{eff}} = 6$ GV/cm. A sample of BaF-doped

solid neon with a concentration of 1 part per billion (ppb) and a volume of 1 $mm^3$ would provide $4.5 \times 10^{10}$ confined molecules. To estimate the number of measurements that can be performed on a single solid, use is made of the fact that a single solid can be kept frozen and used for experiments for many weeks. It is possible to envision performing measurements, each taking 100 ms to perform (10 ms precessions and a duty cycle of 10%), continually for a month. This would result in 26 million experiments, which gives a value of as large as $N = (4.5 \times 10^{10}) \times (26 \times 10^6) = 10^{18}$ precessions observed. However, it may be that only a fraction of the implanted BaF molecules are suitable for a measurement of $d_e$. Only molecules whose orientation has a component aligned or counter-aligned to the applied magnetic field will participate in the measurement. Variance in trapping sites within the neon may play a role, calculations [72] show that while a site with ten neon atoms substituted for a single BaF molecule is the lowest-energy configuration for BaF in a pure $^{20}$Ne matrix, a thirteen-substitution is also a stable trapping site (as it is a local minimum in the energy favourability curve). Additionally, neon and barium have other stable isotopes at natural abundances of approximately 10% and 30%, respec-

tively, which will affect any measurement performed. This will lead to slightly altered sites (due to other Ne isotopes) and unusable BaF molecules. To account for these potential sources of loss, an assumption is made that only 1 in 100 BaF molecules participates in the measurement, $N$ is reduced to $10^{16}$. The estimated statistical uncertainty for an initial measurement using the EDM$^3$ method is then

$$\begin{aligned} \delta d_e &= \frac{\hbar}{2(6\ GV/cm)(10\ ms)\sqrt{10^{16}}} \\ &= 5 \times 10^{-32}\ e\ cm. \end{aligned} \tag{1.23}$$

This is an improvement to the current most precise measurement by two orders of magnitude. Additionally, it is imaginable that further improvements to the experiment (such as larger samples, molecules with larger $\mathcal{E}_{\text{eff}}$, longer coherence times, and many months of measurements) may be able to bridge the gap that remains between the measured value and the value of $d_e$ predicted by the SM.

### 1.3.8 *The study of systematic effects*

To reach the desired precision, it is paramount to test all systematic effects to limit their contributions to the uncertainty.

The EDM$^3$ method has a number of advantages that may lead to smaller systematic effects. A non-exhaustive list of these advantages has been presented in Ref. [26] and is repeated here. They are:

1. A small experiment volume over which the applied magnetic field must be controlled.

2. There is no applied electric field during precession (Figure 1.3 (d)).

3. The BaF molecules are fixed in orientation and position by the matrix.

4. Oppositely oriented molecules serve as co-magnetometers eliminating the effects of the applied magnetic field.

5. The cryogenic environment suppresses motion, thermal voltages, and currents, as well as allowing the possibility of shielding of magnetic fields using super-conductors.

6. A large number of reversals (e.g., magnetic field direction, the orientation of the sample) may be performed alongside a measurement to limit systematic effects.

7. A large dynamic range of experimental parameters (e.g., size of the magnetic field, time of precession) can be used.

8. Matrices may be grown repeatedly with different concentrations of BaF molecules, concentrations of impurities, and imperfections to study the effects on a measurement.

9. The modularity of the experiment allows for a change of polar molecule or inert-gas host to perform comparative measurements.

With the context of the EDM$^3$ method, this work reports on the progress towards a measurement of $d_e$. Chapter 2 of this work describes the experimental apparatus used in pursuit of a measurement. Chapter 3 reports on the progress made towards this measurement and the results used to better understand BaF molecules within neon matrices are shown. Finally, Chapter 4 summarizes these results, reports on the tasks that remain before a measurement using the EDM$^3$ method can be performed, and discusses the steps underway to achieve these goals.

# 2 EXPERIMENTAL APPARATUS

## 2.1 EXPERIMENTAL OVERVIEW

The BaF molecules for this experiment are produced inside of a cryogenic helium-buffer-gas cell via laser ablation of a barium rod in the presence of a small flow of sulphur hexafluoride ($SF_6$) gas. The cell design used in the present work is based on the one developed [73] by the group at Imperial College London. A cutaway view of this cell is shown at the left of Figure 2.1. The BaF molecules, which are entrained in the flow of helium through the cell, exit the buffer-gas cell and are sent downstream to be co-deposited on a cryogenic sapphire substrate alongside neon gas, as shown at the right of Figure 2.1. Both freeze onto the substrate with the neon acting as a host matrix for the BaF molecules. After producing this solid, the BaF molecules trapped within the neon matrix can be excited with a single-frequency widely-tunable

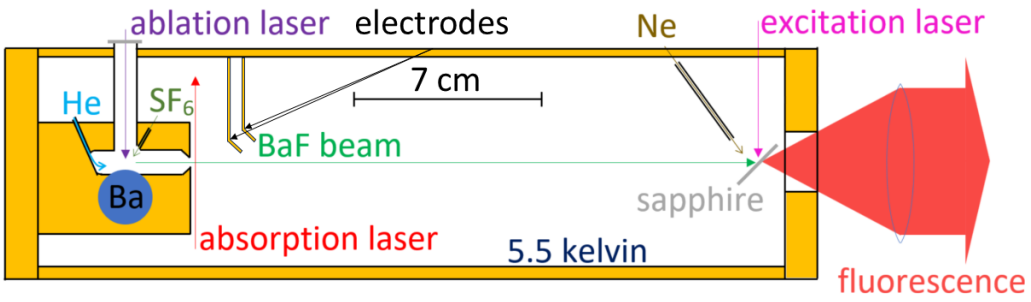


Figure 2.1: Cross-sectional diagram of the 5.5-kelvin section of the apparatus. BaF molecules are produced by ablating a pure barium rod in the presence of a 0.06 sccm flow of $SF_6$ gas. These molecules are swept out of the buffer-gas cell by a steady flow (of 10 sccm) of cryogenic helium gas and travel 20 cm downstream to the sapphire substrate on which neon is co-deposited during the growth procedure. After producing and annealing the doped neon solid laser-induced fluorescence is observed.

laser, with the resulting laser-induced fluorescence detected.

The cryogenic apparatus used for producing and studying these BaF-doped solids consists of two nested layers: the inner layer which is held at a temperature of as low as 5.5 K (as shown in Figure 2.1), and a 60-K outer layer (see Figure 2.2), which serves to protect the inner layer from room-temperature black-body radiation. The details of these layers are discussed in Section 2.2.4 and Section 2.2.3.

The buffer-gas cell shown on the left side of Figure 2.1 has entry ports for helium and $SF_6$ gases (marked with arrows corresponding to their direction of flow). The barium rod is at the base of the buffer-gas cell and a pulsed laser beam, used for laser ablation, passes through the top of the cell down a long cylindrical protrusion capped by a sapphire window. The helium entering the buffer-gas cell is precooled to the base temperature of the apparatus (6.8 K during operation of the buffer-gas cell). The helium flow rate is set to 10 standard cubic centimetres per minute (sccm) during laser ablation. A constant flow of $SF_6$ is also provided during laser ablation at a rate of 0.06 sccm, allowing for the ablated

barium to react and form BaF radicals. The BaF molecules are quickly thermalized and entrained within the helium flow. The helium gas and BaF molecules exit the buffer-gas cell via a 3.5-mm-diameter orifice. The measured forward velocity for the BaF molecules ranges from 150 to 300 m/s. Molecular beam velocity measurements are discussed in greater detail in Section 3.1.3.

The beam of BaF molecules is observed using an absorption laser tuned to 859.839 nm, which is in resonance with the transition from the lowest vibrational and second lowest rotational state of the ground electronic state of BaF to the lowest-lying $\Pi$ state ( $X^2\Sigma_{1/2}(v = 0, N = 1) \rightarrow A^2\Pi_{1/2}(v = 0, j = 1/2^+)$). The resonance structure and broadening for the observed absorption feature is discussed in Section 3.1.2.The absorption-laser beam is a distance of 1.5 mm away from the output of the buffer-gas cell, intersecting the beam of BaF molecules at a angle perpendicular to the forward velocity of the molecules (as shown in Figure 2.1). The absorbed light from this laser beam provides an estimate of the total number of BaF molecules produced and this estimate is discussed in

detail in Section 3.1.4.

The BaF molecules travel 20 cm downstream to a cryogenic sapphire substrate (see Figure 2.1), where a flow of neon gas is co-deposited at a rate of 20 sccm on the substrate to grow a neon matrix doped with BaF molecules. Growth continues for approximately one hour, in which time the solid reaches a thickness of approximately 1 mm. In the 20-cm region between the buffer-gas cell and the sapphire substrate, the sides of the 5.5-K cryogenic enclosure of Figure 2.1 are coated with a layer of activated charcoal, which reduces the partial pressure of helium and other contaminants by efficiently cryopumping the helium gas ejected from the buffer-gas cell.

The intensity of the laser-induced fluorescence from BaF molecules within the solid is monitored and is found to increase approximately proportionally to the time since the start of growth. From this proportionality it is deduced that the solid is sufficiently transparent for efficient transmission of the laser and fluorescence light. Fluorescence detection during solid growth is discussed in greater detail in Section 3.2.2. Once a BaF-doped neon matrix is grown, the solid is allowed

to cool to a temperature of 5.8 K. Several annealing cycles (in which the temperature of the substrate is raised to 8.4 K at a rate of 2 K per minute, left at this temperature for 5 minutes then once again cooled, at the same rate, back to 5.8 K) are performed. In Section 3.2.4 this annealing procedure and the resulting solids produced are discussed in greater detail.

The annealed BaF-doped neon solid is illuminated with a tightly focused laser beam (with a diameter of 40 microns for intensity to be reduced to $1/e^2$) with a maximum beam-centre intensity of 80 kW/cm$^2$ in order to induce fluorescence from the embedded BaF molecules. The fluorescence is collected at an angle perpendicular to the excitation laser propagation direction using a 2-inch-diameter lens (see Figure 2.2) located 6 cm beyond the substrate. The light collimated by this lens is sent through a vacuum window at the far end of the experiment chamber. The fluorescence collection system collects approximately 1% of the total fluorescence emitted from the solid (4.5% of $4\pi$ steradians with an 84% loss). Outside of vacuum, wavelength filtering and subsequent focusing onto the detection instrument is performed. The filtered and focused light is observed by one of two spectrom-

eters (whose characteristics are discussed in Section 2.6.2), a liquid-nitrogen-cooled indium-gallium-arsenide (InGaAs) detector (discussed in Section 2.6.3), or a single-photon counter (discussed in Section 2.6.4).

## 2.2 VACUUM SYSTEM AND CRYOGENIC COMPONENTS

### 2.2.1 *Vacuum system*

Figure 2.2 presents a diagram, drawn to scale, of the full vacuum chamber, magnetic coils, and cryogenic apparatus to provide a relative sense of scale between components. The vacuum system is composed of three identical super-cross vacuum chambers. Each super-cross vacuum chamber consists of an 18-inch-diameter spherical body intersected by three orthogonal 12-inch-diameter cylinders of 20 inches in length. The full cryogenic apparatus (left side of Figure 2.2) is contained entirely within the first chamber while the two remaining chambers are used for connection of essential instruments for maintaining and monitoring the vacuum environment of the experiment. These two additional vacuum chambers have the added benefit of being easily adaptable

to future experimental modifications. The vacuum system is designed to use stainless steel flanges with all-metal seals and is capable of ultimate pressures of below $10^{-9}$ torr using a single Edwards 1000 L/s turbo-molecular pump. For convenience some all-metal seals have been temporarily replaced with viton seals which are capable of an ultimate pressure of $5 \times 10^{-9}$ torr, which is sufficient for the current experiments. These viton seals allow the use of lighter, and more easily modified, aluminum flanges on the vacuum chamber.

### 2.2.2 *External components for the cryogenic system*

Figure 2.3 shows a simplified diagram of the cryogenic system, which consists of a cryocooler (Sumitomo Heavy Industries Gifford-McMahon model RDK-408D2) connected to a compressor (Sumitomo model F70L) by way of 20-foot-long pressurized helium gas lines. The cryocooler extracts heat from the apparatus and transfers this heat to the F70L compressor which unloads the excess energy into a closed-loop water system. A steady supply of $23^{o}$C water from a water-to-air compact chiller (SMC-automation model HRSH090) is used. By using a closed-loop, this system is able to contin-

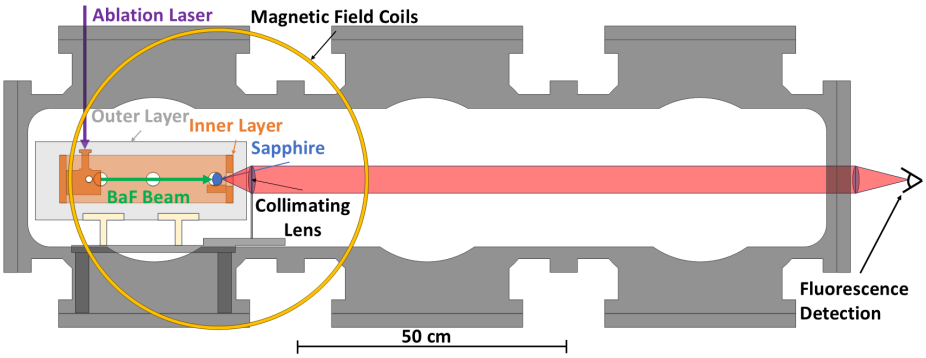


Figure 2.2: Experimental vacuum chamber cross-section. This diagram, drawn to scale, depicts the vacuum system, magnetic field coils, and the experimental apparatus contained within the vacuum chamber. The vacuum system is composed of three identical super-cross vacuum chambers. The diagram provides a relative sense of scale for the cryogenic region (the rectangular region on the left) and the total volume available within the vacuum chamber. The BaF-doped matrices grown are illuminated with laser light (directed into the page at the sapphire substrate) and the induced fluorescence is collimated with a single 2-inch-diameter lens in the vacuum system placed 6 cm away from the matrix. The collimated light passes more than 1 m through the vacuum system and is focused onto a detection instrument outside of vacuum.

uously run the experiment with only basic monitoring of water flow and temperature. This cooling system allows for cryogenic temperatures to be maintained continuously for over six months.

The cryocooler provides cooling to two distinct stages: the first stage, which has a base temperature of 32 K when subjected to heat loads of 50 W or less, and the second stage, which has a base temperature of 3 K. The first and second stages of the cryocooler are independently attached to the outer and inner layer of the cryogenic apparatus, respectively, using flexible 57-mm-long copper braids ( Technology Applications, Inc. model P50-502). These flexible copper braids limit the transfer of vibrations from the cryocooler to the apparatus while ensuring efficient heat transfer between the cryocooler and custom cryogenic apparatus.

### 2.2.3 *Outer layer of the cryogenic apparatus*

Figure 2.4 shows the outer layer of the cryogenic apparatus, which is connected to the first stage of the cryocooler. The outer layer's main body is constructed from aluminum pan-

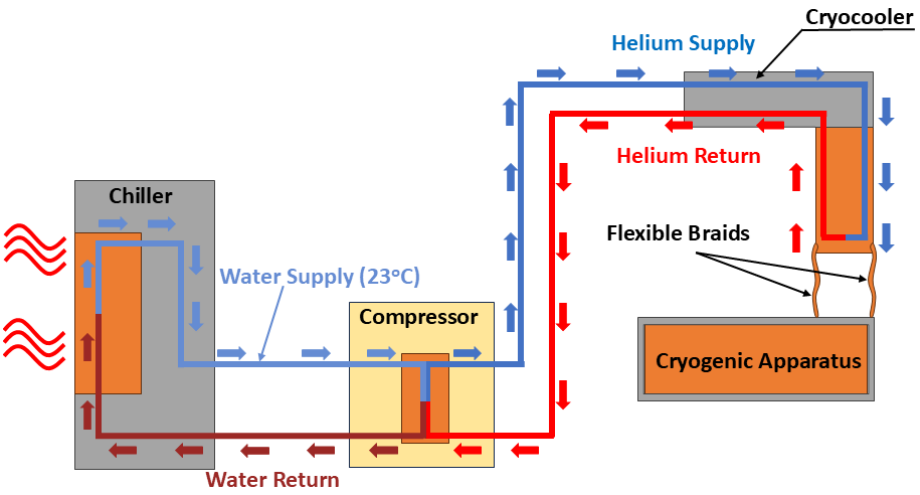


Figure 2.3: Cryogenic system schematic. A simplified diagram showing the active components used in the cryogenic system. The arrows indicate the direction of flow for helium and water, which are used as media to transfer heat from the cryogenic apparatus in the experiment to the air of the laboratory. The components are individually labelled from left to right: the SMC-automation water-to-air compact chiller supplying 23 $^{o}$C water for the closed loop system, the Sumitomo compressor transferring heat from the warm helium to the closed-loop water circuit, the Sumitomo cryocooler which carries heat out of the experiment chamber, and the custom cryogenic apparatus described in Section 2.2.3 and Section 2.2.4. The diagram is not to scale.

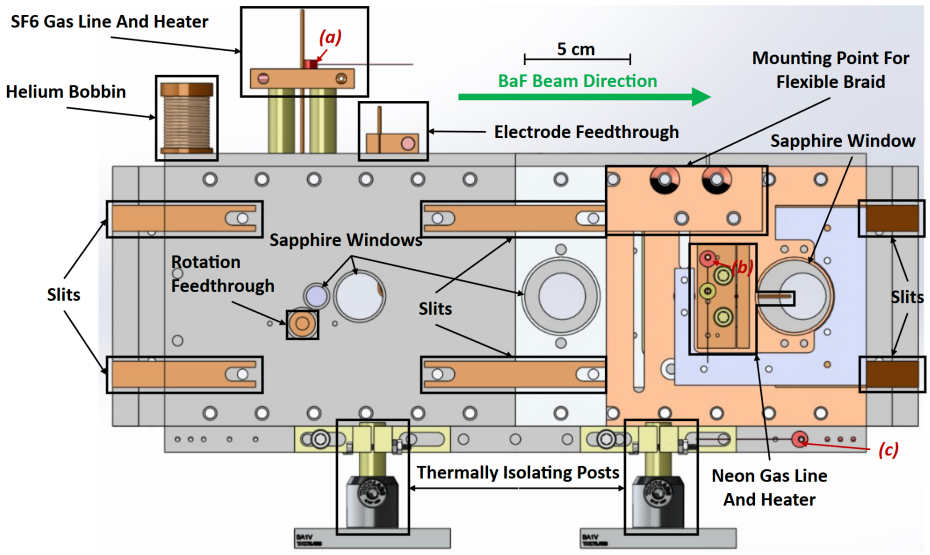


Figure 2.4: Outer layer of the cryogenic apparatus. A diagram of the outer layer of the cryogenic apparatus, drawn to scale, with various components and feedthroughs highlighted. Silicon-diode temperature sensors, each near an accompanying heater, are highlighted in red and labelled: *(a)*, *(b)*, and *(c)*. This outer layer is kept at a temperature of 60 K and protects the inner layer from the ambient room-temperature thermal radiation. The sapphire windows provide optical access for absorption and excitation lasers and for fluorescence, while blocking most of the room-temperature black-body radiation from the surrounding environment.

els that are easily removable for modification purposes. This outer layer is thermally stood off from the room-temperature vacuum chamber by way of four 0.5-inch-diameter polyether ether ketone (PEEK) posts that are 6 cm in length (see Figure 2.4). These posts serve as thermal breaks to minimize points of contact between the chamber and cryogenic apparatus while maintaining enough structural integrity to fix the cryogenic apparatus firmly in place. The thermal conduction from the vacuum chamber to the outer layer through the thermally-isolating posts has been modelled and the estimated heat flow is $\leq 10$ W.

Optical access through the outer layer is via sapphire windows, which are able to transmit light in the wavelength regions of interest for spectroscopic studies of BaF molecules, while blocking most of the black-body radiation emitted by the surrounding room-temperature chamber. Multiple openings (denoted as slits in Figure 2.4 ) are strategically placed on every side of the outer layer to allow for sensor and heater wires to pass through. These openings are carefully covered with thin strips of copper (shown in Figure 2.4), after all routing of the sensor and heater wires is completed, to ensure

no direct lines of sight are available for black-body radiation from the room-temperature vacuum chamber to the inner layer.

The outer layer of the cryogenic system is maintained at a temperature of 60 K (read by sensor (c) in Figure 2.4), while components that are thermally stood off from the outer layer (such as those with at the locations of sensors (a) and (b) in Figure 2.4) are heated to warmer temperatures of approximately 100 K. Even at 100 K, these components produce thermal radiation at an intensity of 1% of that emitted from room-temperature bodies.

### 2.2.4 *Inner layer of the cryogenic apparatus*

Figure 2.5 shows the inner layer of the cryogenic apparatus, which is constructed from oxygen-free high-thermal-conductivity (OFHC) copper and maintained at a base temperature of 5.5 K. The base temperature of the cryocooler with no external heat load is 3 K, indicating that the apparatus may yet be further cooled by further isolating it from ambient heat loads.

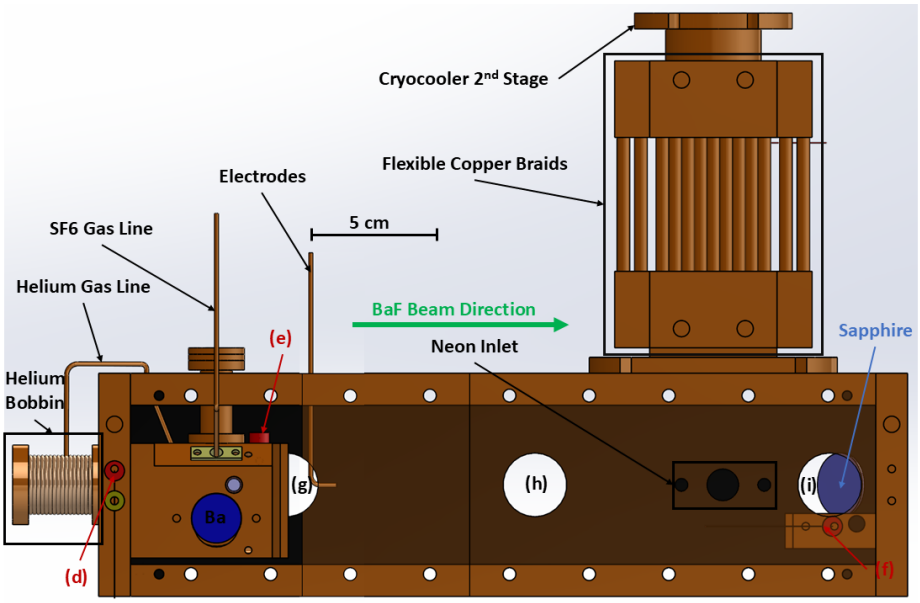


Figure 2.5: Inner layer of the cryogenic apparatus. A diagram of the inner layer of the cryogenic apparatus, drawn to scale, with critical components highlighted and annotated. In this figure the front wall of this layer has been made partially transparent to provide a view into the central volume of the apparatus. Three silicon-diode temperature sensors are highlighted in red and labelled: (d), (e), and (f). Three circular cutouts that provide optical access to the molecular beam path and sapphire substrate are labelled: (g), (h), and (i). This layer is constructed from OFHC copper and activated charcoal is epoxied to the inner panels to efficiently cryopump helium from the operation of the buffer-gas cell.

The inner layer of the cryogenic apparatus is bolted together with a thin layer of indium placed between components to ensure good thermal connectivity, creating a uniform temperature for the entire layer. The inner-layer box has inner dimensions of 33.3 cm in length, 8.9 cm in width, and 8.9 cm in height. The relatively large volume enclosed within it houses the buffer-gas cell and the sapphire substrate, separated by a distance of 20 cm.

A series of three circular holes (see (g), (h), (i) in Figure 2.5) in the front panel (and three similar holes in the back panel) of the inner layer provide optical access. The large distance between the buffer-gas cell and the sapphire substrate provides the required space to implement a system to deflect the BaF molecules in order to separate them from other unwanted ablation products. Three such deflection schemes have been proposed by the EDM$^3$ collaboration [74–76]. The furthest circular hole from the output of the buffer-gas cell, (i) in Figure 2.5, is used for the excitation laser beam incident on the sapphire substrate on which the BaF-doped neon matrices are grown. A 2-inch-diameter sapphire window is located

at the end of the inner layer (this window is embedded into the panel to the right of the sapphire substrate in Figure 2.5) and allows for the laser-induced fluorescence from the BaF molecules to be collected with a lens placed in vacuum (see Figure 2.2).

Activated charcoal is epoxied to the inside surfaces of the panels of the inner layer of the cryogenic apparatus to cryopump helium gas during operation of the buffer-gas cell. Silver-infused epoxy is used to maintain good thermal contact between the charcoal and the inner-layer copper, as the the capture efficiency for helium gas in charcoal is strongly temperature dependent. The epoxy is cured by heating the panels in an oven at 400 K for several hours. Once the apparatus is placed in the vacuum system it is further baked at 330 K for 48 hours under vacuum, to expel any residual water vapour (or other gases) condensed within the charcoal and on the surface of the apparatus. It is found that the output of the buffer-gas cell is strongly dependent on whether the system has been baked in this manner. Efficient cryopumping of helium gas by the activated charcoal layer is necessary as, if not captured by the charcoal, the partial pressure of helium

gas in the apparatus during growth is sufficient to thermally connect the inner and outer layers.

Two thin copper tubes serve as electrodes (see Figure 2.5) to deflect any positive or negative ions (or electrons) exiting the buffer-gas cell. The electrodes carry voltages of $\pm 15$ V, and are fed into the inner layer through a thin slot. They are thermally anchored to the 60-K outer layer to reduce the emission of black-body radiation. These electrodes are held at a distance of 1.2 cm from the output of the buffer gas cell and 1.5 cm to either side of the beam of BaF molecules.

## 2.3 BUFFER-GAS CELL AS A SOURCE OF POLAR MOLECULES

### 2.3.1 *Buffer-gas cell design and operating conditions*

Figure 2.6 shows the buffer-gas cell used for this experiment. The design is based on a cell first developed by the group at Imperial College London [19, 73, 77–80]. The buffer-gas cell consists of a 10-mm-diameter chamber (see Figure 2.6b) carefully sculpted using electrical discharge machining, from a solid block of OFHC copper to create a smooth flow of

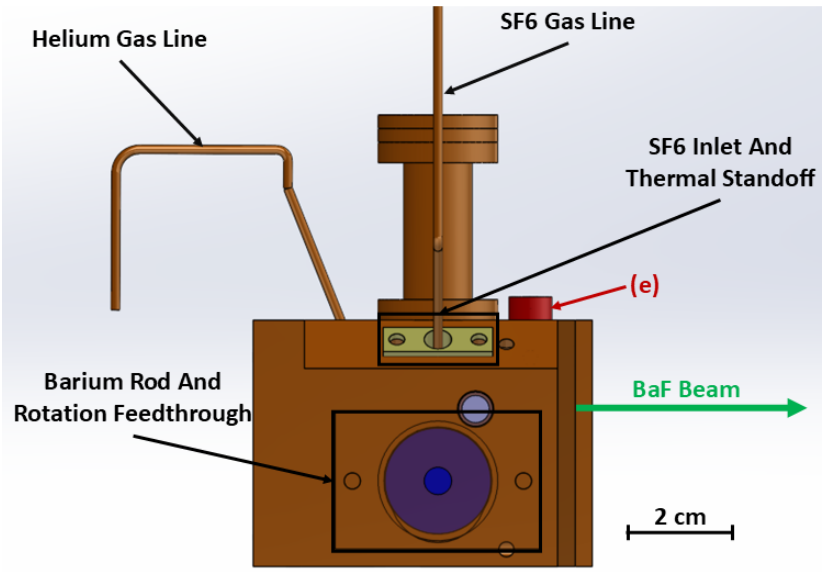


(a) Buffer-gas cell

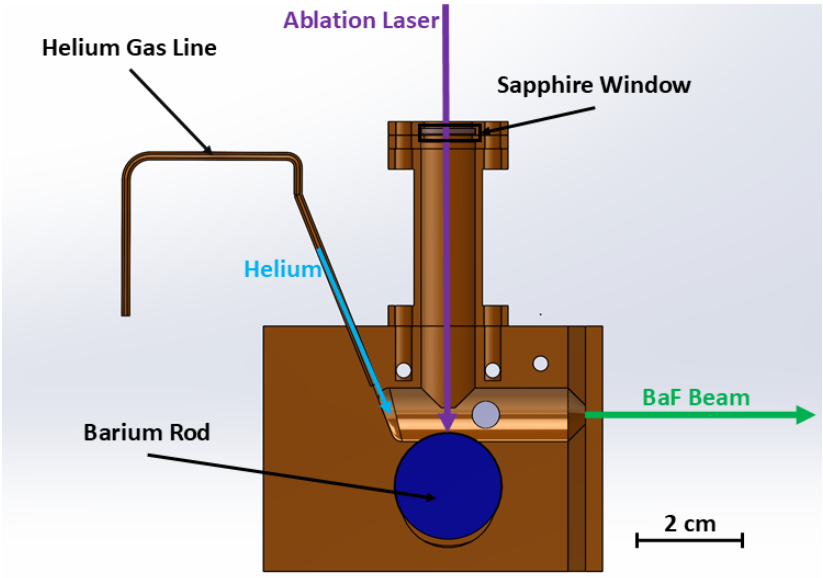


(b) Buffer-gas cell cross-section

Figure 2.6: The buffer-gas cell. Panel (a) shows the buffer-gas cell with the rotation-feedthrough housing made partially transparent. Panel (b) provides a cross-sectional view into the cell with a clear view of the 10-mm-diameter ablation chamber where BaF molecules are formed.

precooled helium gas injected at the back of the cell. The helium gas is cooled by wrapping (and bonding) the 0.0625-inch-inner-diameter-copper gas feed line around two bobbins thermally anchored to the outer layer and inner layer (as shown in Figures 2.4 and 2.5, respectively).

The ablation-laser beam comes from above and passes through an extended cylindrical protrusion of the cell which is capped by a transparent sapphire window (shown in Figure 2.6b). The protrusion is designed to reduce the amount of ablation products that are able to reach this sapphire window. These ablation products create a cloudy film on the sapphire window, which reduces the intensity of the ablation laser on the barium surface below. The 20-mm-diameter barium rod is at the base of the cell (see Figure 2.6b) and can be rotated from outside the vacuum chamber using a rotation shaft and a rotational feedthrough. This rotation shaft attaches to the housing shown in Figure 2.6a.

The rotational shaft is thermally anchored to the outer layer (its position is annotated in Figure 2.4) of the cryogenic apparatus and constructed from insulating materials to limit

the transmission of heat between the two cryogenic layers.

An $SF_6$ gas inlet (see Figure 2.6a), directed at the ablation spot allows an ablated barium atom to form a BaF molecule by stripping a fluorine atom from an $SF_6$ molecule. During growth, the $SF_6$ gas line is held at 300 K to keep the $SF_6$ in a gaseous state. The $SF_6$ gas inlet is thermally stood off from the buffer-gas cell by way of a thin PEEK fitting (see Figure 2.6a) to limit the heat transfer from this gas line.

### 2.3.2 *Spectroscopic absorption and molecular beam velocity*

To detect buffer-gas-cell-emitted BaF molecules and determine the efficacy of the production of BaF molecules, an absorption laser is employed. The multiple laser-beam paths along which absorption is detected are show in Figure 2.7 (labelled: (1), (2), and (3)). An external-cavity diode laser (Toptica Photonics model DL-Pro / LD-0860-0080-AR-1) is used to excite the $^{138}$BaF $X^2\Sigma_{1/2}(v = 0, N = 1) \rightarrow A^2\Pi_{1/2}$ $(v = 0, j = 1/2^+)$ transition (as discussed in more detail in Section 3.1.2). This transition is well-studied and used in many laser-cooling and laser-manipulation schemes [47, 50,

81, 82].

The output of this laser is coupled into a single-mode optical fibre which transmits the light to an optical breadboard just outside of the vacuum system. This laser light is split into three separate paths along the BaF beam line and sent through the vacuum chamber and cryogenic apparatus through sapphire windows in the outer layer (see Figure 2.4) and circular holes in the inner layer (highlighted in Figure 2.7). The absorption laser beams (1), (2), and (3) of Figure 2.7 intersect the molecular beam at distances of 0.15 cm, 10 cm, and 20 cm from the output of the buffer-gas cell. Once it passes through the apparatus, the laser light for each path is focused onto an amplified photodiode (Thorlabs model PDA36A). A band-pass filter, which filters light outside of a 850-nm-to-870-nm wavelength band, and a notch filter at 1064 nm (used to specifically attenuate the light produced from the powerful ablation laser) are placed in front of each photodiode to ensure that only the light from the absorption laser is detected. The laser beam passing through the BaF molecular beam is focused to a $1/e^2$ intensity diameter of 1.75 mm and a laser power of 10 $\mu$W is used for the

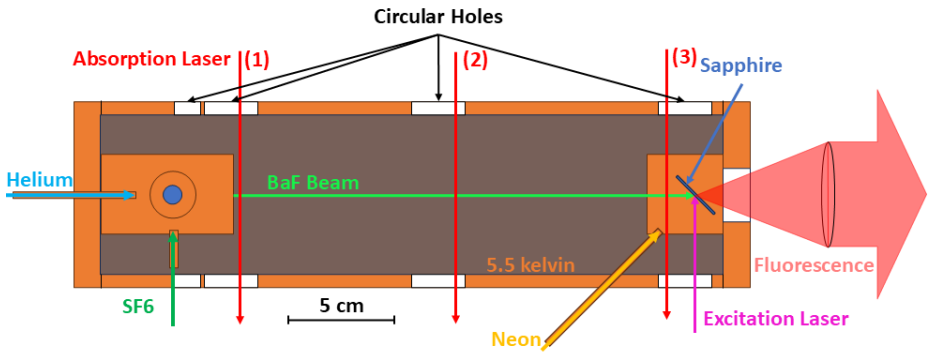


Figure 2.7: Laser paths. A diagram, drawn to scale, providing a top-down cross-sectional view of the inner layer of the cryogenic system and the various laser paths used throughout this work. The absorption laser branches into three different paths (labelled (1), (2), and (3)) that intersect the beam of BaF molecules at locations, 0.15 cm, 10 cm , and 20 cm downstream from the output of the buffer-gas cell. The excitation laser enters the apparatus using the farthest circular hole and illuminates the neon solid at an angle of $45^{o}$ relative to the sapphire substrate.

absorption measurements.

In Section 3.1.2 the results from absorption experiments are used to determine the total number of BaF molecules exiting the buffer-gas cell and in Section 3.1.3 laser absorption signals from the three locations along the trajectory of the BaF molecular beam (see Figure 2.7: (1), (2), and (3)) are used to perform a coarse measurement of the forward velocity of the beam of BaF molecules.

## 2.4 Magnetic field and radio-frequency generation

### 2.4.1 *Magnetic field generation*

Figures 2.2 and 2.8 show the coils used to produce magnetic fields in the apparatus. Four coils provide a uniform magnetic field at the location of the substrate with field strengths of up to 30 G. These four coils are placed symmetrically, in pairs, around the substrate and are aligned so that the magnetic field will be parallel (or anti-parallel) to the direction of the axis of the excitation-laser propagation. The coils are 56 cm

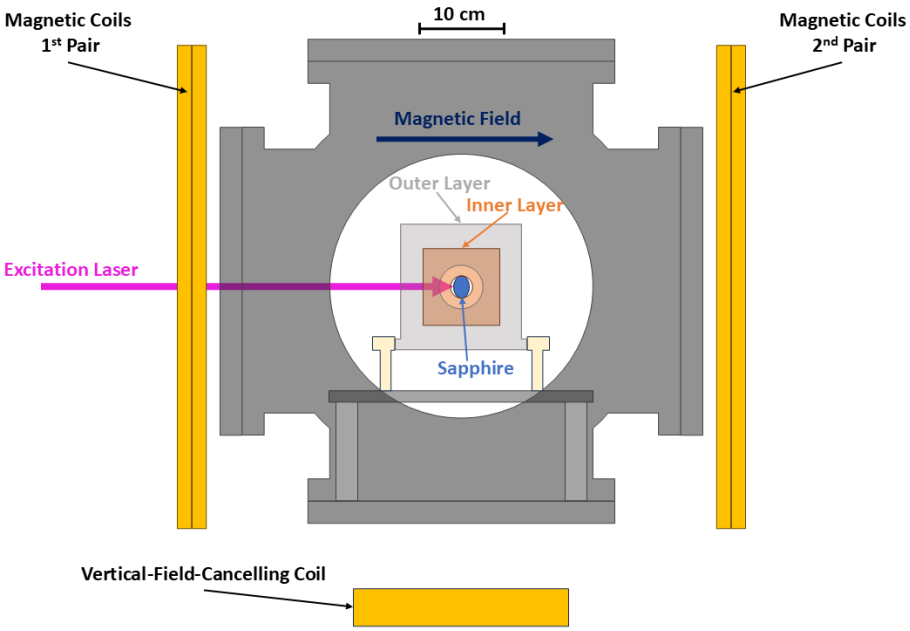


Figure 2.8: A diagram, drawn to scale, showing the four magnetic field coils used to generate a magnetic field. The coils are placed in two pairs symmetrically around the BaF-doped neon solid on the sapphire substrate. The coils allow for the application of magnetic fields aligned or counter-aligned to the excitation laser propagation axis. An additional coil cancels the small vertical component of the Earth's magnetic field.

in diameter and the pairs are placed at a distance of 30 cm from the location of the substrate. An additional coil, located beneath the vacuum chamber, is used to cancel the vertical component of the Earth's magnetic field.

The pairs of coils create a homogeneous field (with a field strength calibrated using Gauss-meter measurements at several locations) in the small volume of interest at the sapphire substrate. The direction of the current through the coils can be inverted allowing the generated magnetic field to be aligned or counter-aligned with the propagation axis of the excitation laser.

### 2.4.2 *Radio-frequency systems*

Figure 2.9 shows a diagram, drawn to scale, of the coils used to produce radio-frequency (RF) fields. Two circular coils are situated near the sapphire substrate, with the neon gas flow aimed through the centre of the coils. The coils have a diameter of 1 inch and are placed in orientations that are perpendicular with respect to each other, with one of the coils parallel to the surface of the sapphire substrate. The RF field

is produced using one of the two coils and pick-up by the other coil is used to provide a measure of the field present.

A two-channel radio-frequency generator (Instrument Flight Research (IFR) model 2026B) along with an amplifier capable of outputting up to 46 decibel-milliwatts (dBm) of RF power (for a frequency range of 1 MHz to 120 MHz) is employed to provide the radio-frequency field required for experiments described in Section 3.6. These coils are removable, between matrix growths, and are only installed when experiments requiring RF fields are performed.

## 2.5 LASER SYSTEMS

### 2.5.1 *Nd:YAG ablation laser*

We employ a 1064-nm neodymium-doped yttrium aluminum garnet (Nd:YAG) laser (Litron Lasers model Nano L 90-100, capable of producing 6-ns-long pulses at a repetition rate of up to 100 Hz and a maximum energy of 90 mJ per pulse) for laser ablation. This laser is located on an isolated, fully-enclosed, optics table mounted directly to the top of the

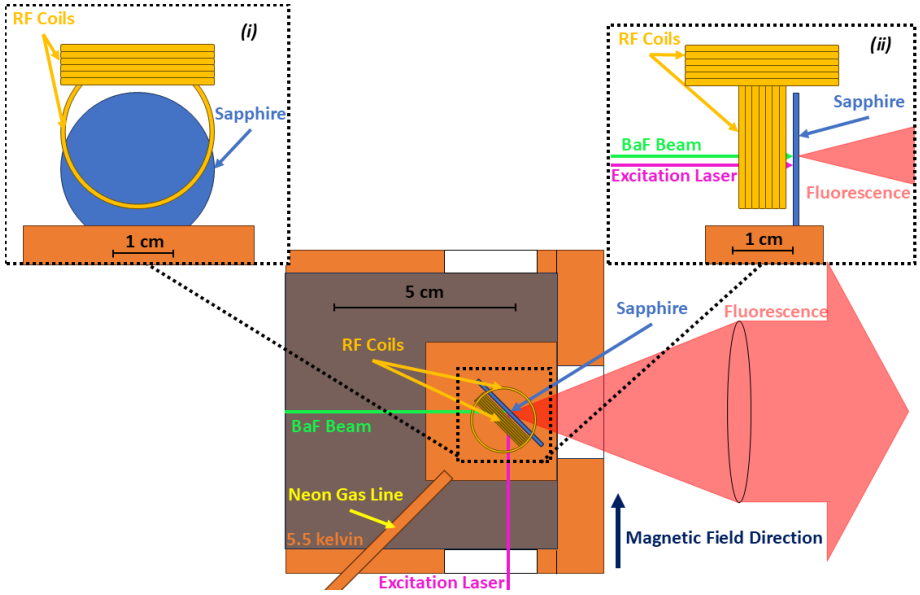


Figure 2.9: Diagram of the circular RF coils and their placement. The main panel provides a top-down cross-sectional view of the cryogenic apparatus where the circular coils used to produce RF fields are installed. The insets provide rotated and magnified views of the coils for clarity. Inset (i) is rotated $45^o$ away from the excitation laser and directly faces the sapphire substrate providing a view as perceived by a viewer at the position of the neon gas line. Inset (ii) is rotated $45^o$ away from the excitation laser in the opposite direction providing a view of the sapphire along the edge of the substrate.

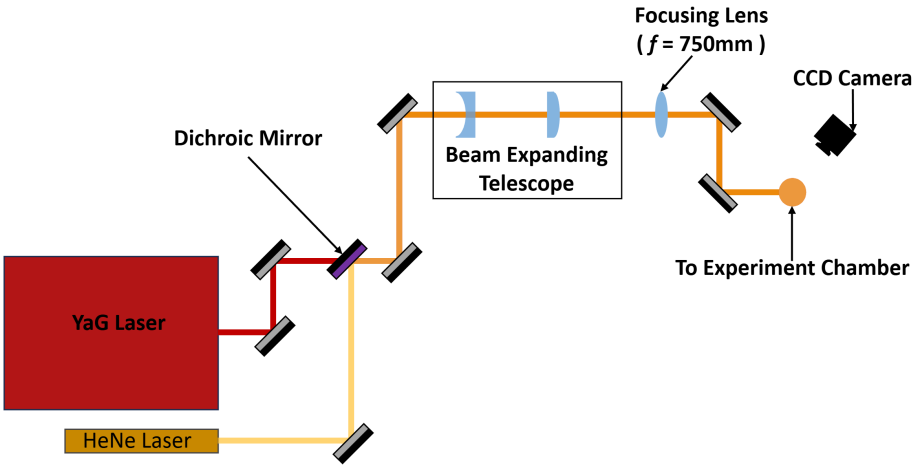


Figure 2.10: The beam path of the Nd:YAG ablation laser beam. A helium-neon (HeNe) laser beam is overlapped with the ablation laser using a dichroic mirror and the co-propagating beams are aligned through the apparatus. The combination of the beam-expanding telescope and focusing lens allows for a beam diameter of 3.3 mm at the barium surface to achieve the desired fluence on the surface of the barium rod. The dichroic mirror, which overlaps the beams, is removed after coarse alignment and before ablation begins. This diagram is not drawn to scale.

vacuum system. Figure 2.10 shows the optical path of the ablation laser. The beam is focused using a $f = 750$ mm lens outside of the vacuum chamber and passes through a window at the top of the chamber which provides a direct line-of-sight optical path to the barium rod at the base of the buffer-gas cell.

The initial alignment of the laser is performed by using a dichroic mirror to overlap a HeNe laser beam with a low-power Nd:YAG laser beam and using the visible light of the HeNe laser to guide the co-propagating beams through the apparatus. Following this alignment, the dichroic mirror is removed from the laser path to avoid damage due to the powerful Nd:YAG laser. Fine adjustments to the ablation laser path are performed by imaging the Nd:YAG beam spot on the barium rod using a charge-coupled device (CCD) camera (see Figure 2.10).

The focusing lens in the path of the Nd:YAG laser beam is positioned such that the beam diameter ($1/e^2$ of intensity) is 3.3 mm at the surface of the barium rod, a spot size which leads to a fluence of $I_{Nd:YAG} = 2.1$ J/cm$^2$ if this laser is run at

full power. It is observed, however, that such a high fluence is not necessary to efficiently ablate the barium in this system.

Initially, the threshold for ablation is found to be at approximately 0.6 J/cm$^2$ of pulse energy, with the maximum amount of ablation occurring at approximately 1.5 J/cm$^2$. The sapphire window that sits at the top of the buffer-gas cell (see Figure 2.6b) becomes cloudy and attenuates the ablation laser significantly after many pulses of the ablation laser, which significantly impedes the ablation process. This cloudiness can only be fully resolved by opening the vacuum system and replacing the polluted sapphire window, attempts to clean the particulate from the sapphire have failed to render it sufficiently transparent to the ablation laser light.

### 2.5.2 *Titanium-sapphire laser*

To study the laser-induced fluorescence from BaF molecules in the neon matrix, a titanium-sapphire continuous-wave widely-tunable laser (Spectra-Physics model Matisse CS) is employed. This titanium-sapphire laser can produce at least 1 W of power over the wavelength range of 700 nm to

1000 nm, with a peak output power of 7.2 W. This laser is used in a variety of applications and in many configurations depending on the particular experiment being performed on the BaF-doped neon solid. The preparation of the laser light (one or multiple beams) is performed on a 4-foot-by-12-foot optics table and the laser beams are then coupled into single-mode polarization-maintaining optical fibres, which serve to transmit the light onto a smaller optics board directly attached to the vacuum chamber where the free-space laser beam is carefully directed onto the substrate.

### 2.5.3 *Diode lasers*

For the purpose of laser-absorption spectroscopy an external-cavity diode laser (Toptica Photonics model DL-Pro / LD-0860-0080-AR-1) is employed, with a tunable wavelength (840 nm to 875 nm) to observe the BaF molecules after they exit the buffer-gas cell. This laser has a maximum output power of 90 mW and linewidth of 5 kHz. The laser is fibre coupled and attenuated to a power of 10 $\mu$W. Its free-running stability at the desired wavelength of 859.839 nm is such that it can

be left unattended while a matrix growth is performed with no feedback required.

## 2.6 FLUORESCENCE DETECTION SYSTEMS

### 2.6.1 *Fluorescence collection beam path*

The fluorescence emitted from the BaF molecules within the solid is collected using a 2-inch-diameter lens that is 5 cm away from the sapphire substrate (see Figure 2.7), which collimates the laser induced-fluorescence. The collimated light travels 1.1 m through the vacuum system before exiting through a quartz window on the far side of the vacuum system, as shown in Figure 2.2. Outside of vacuum, the collimated light is focused down to a diameter of approximately 2.5 cm, re-collimated, passed through a series of wavelength filters and focused onto the light-detection device in use.

### 2.6.2 *Spectrometers*

Two different spectrometers are used, each covering different wavelength ranges of fluorescence light. The first spectrome-

ter (Ocean optics model QE Pro) is capable of detecting light from 350 nm to 1125 nm. The QE Pro is actively cooled using a thermoelectric cooler (TEC) and is kept at a temperature of $-30^{o}$C during operation, which provides excellent suppression of the dark current. To maintain a temperature of $-30^{o}$C, the entire spectrometer is placed inside of a refrigerator. This instrument is capable of integration periods of between 8 ms and 1 hour.

The QE Pro spectrometer has a set of entrance slits for the incoming light, with widths ranging from 5 $\mu$m to 200 $\mu$m, which provide wavelength resolutions ranging from 1.1 nm to 4.8 nm (with the higher resolution coming at the cost of photon detection efficiency). All data presented in this work is collected with the minimum slit size in order to maximize the wavelength resolution of the spectrometer. To compensate for the reduction in efficiency, low-intensity experiments used longer integration times to achieve the desired signal-to-noise.

For wavelength ranges extending deeper into the infrared, a second spectrometer (Optosky model ATP8200) is used. The

ATP8200 spectrometer covers the wavelength region from 900 nm to 2500 nm, with integration times of 1 ms to 500 ms. The slit width of the spectrometer is fixed at 50 $\mu$m and the wavelength resolution is fixed at 3 nm. The TEC within the ATP8200 can only cool the InGaAs CCD to a temperature of $-10^{o}$C, which leads to a dramatically higher dark current (compared to the QE-Pro spectrometer).

Both spectrometers are calibrated using the wavelength profile of a well-characterized thermal light source (Thorlabs model QTH10). This quartz tungsten-halogen lamp emits black-body radiation at a temperature of 2800 K. Each channel of the spectrometers is assigned a relative-efficiency factor to match the measured spectrum with the known emission characteristics of the thermal source. The calibration procedure is verified by comparing measured laser powers at various wavelengths with the relative signal, recorded by the spectrometers at these wavelengths.

### 2.6.3 *Indium-gallium-arsenide photodetector*

For applications in which the highest signal-to-noise is required, a 3-mm-diameter liquid-nitrogen-cooled InGaAs photodiode (Electro-optical systems model IGA-030-E-LN6N) is used. This detector is sensitive to light in the spectral range of 900 nm to 1500 nm. Its built-in amplifier has a gain of $10^9$ V/A, a bandwidth of 300 Hz, and a noise-equivalent-power of $1.5 \times 10^{-15}$ W/$\sqrt{\text{Hz}}$.

### 2.6.4 *Single-photon counter*

In applications where precise timing of photon arrival is required, a single-photon counter (Excitas model SPCM-AQRH-16-FC), is used in conjunction with a time tagger (Cronologic model 4-2G). The combination of these devices is able to record the arrival time of photons, within a wavelength range of 400 nm to 1100 nm, with a timing precision of $\leq$ 500 ps.

# 3 RESULTS

## 3.1 PRODUCTION OF BAF MOLECULES SUITABLE FOR EDM$^3$

### 3.1.1 *Ablation parameters*

To optimize the yield of BaF molecules produced by the buffer-gas ablation cell, the ablation laser is setup as described in Section 2.5.1 and a range of buffer-gas-cell-operation parameters are tested. Table 3.1 summarizes the optimal values used in experiments presented in this work .

The ablation laser is pulsed at a rate of 5 Hz. During the growth procedure, it is observed that the absorption signal diminishes over a time scale of 20 to 30 minutes (approximately 7,500 pulses), requiring the ablation-laser beam to be relocated to a fresh spot on the surface of the barium rod.

| Ablation Laser Parameter | Optimal Value |
|---|---|
| Pulse Energy (mJ) | 27 to 90 |
| Wavelength (nm) | 1064 |
| Spot Diameter (mm) | 3.3 |
| Pulse Fluence ($J/cm^2$) | 0.6 to 2.1 |
| Repetition Rate (Hz) | 5 |

Table 3.1: Ablation parameters used during the growth of matrices. The total energy per pulse varied during growths, with the absorption signal (see Section 3.1.2) used as a guide to determine the efficacy of the ablation. The efficacy is also dependent on the number of growths conducted since the buffer-gas cell has been cleaned.

An example of such a movement is shown in Figure 3.1 as seen by a CCD camera positioned above the apparatus (see Figure 2.10).

### 3.1.2 *Absorption signal of BaF at the buffer-gas cell output*

To study the molecular yield of the buffer-gas cell an absorption-laser beam is placed 1.5 mm away from the output of the buffer-gas cell (see Figure 2.7). The diode-laser beam used for absorption has a gaussian profile with a central beam intensity of $I_{\text{centre}} = 0.83\ \text{mW/cm}^2$, a 1.75 mm beam diameter, and power of 10 $\mu$W. The absorption laser beam is tuned to a measured (vacuum) wavelength of 859.839 nm to drive the $X^2\Sigma_{1/2}(v = 0, N = 1) \rightarrow A^2\Pi_{1/2}(v = 0, j = 1/2^+)$ transition, which is a well-studied [57, 58] transition used in laser cooling of BaF. Due to its low power, the laser addresses only one sublevel of the hyperfine structure of the $X^2\Sigma_{1/2}(v = 0, N = 1)$ electronic ground state (see Figure 3.2) for each Doppler group of the BaF beam. When scanning the frequency of the absorption laser the hyperfine structure is only partially resolved (as shown in Figure 3.3), due to

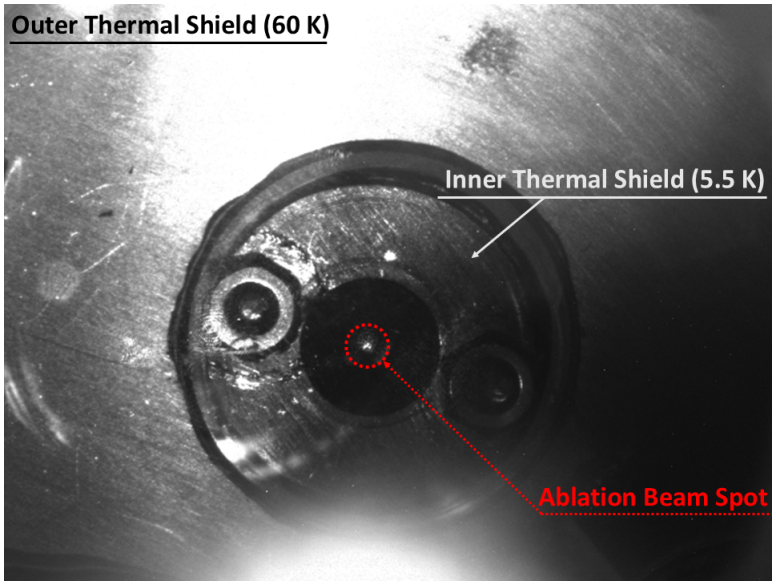


(a)

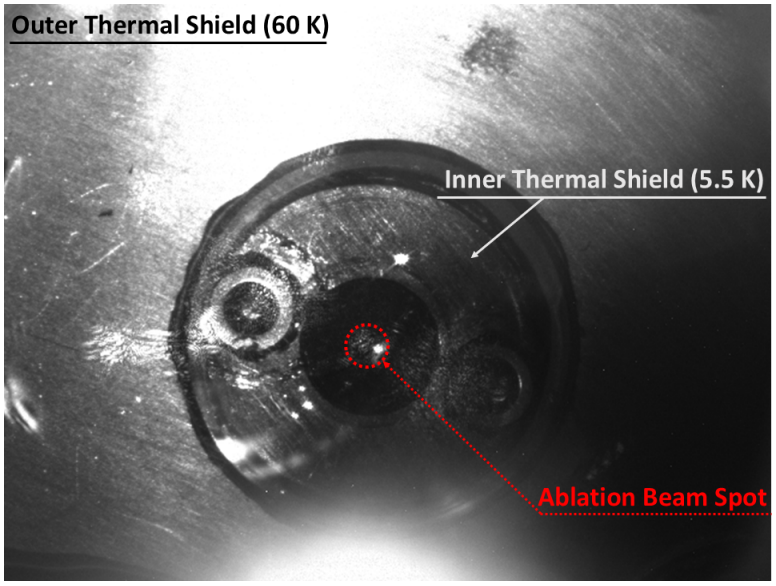


(b)

Figure 3.1: The Nd:YAG ablation spot. Panel (a) shows the ablation laser spot at its initial location. Panel (b) shows the laser spot's new location after it is moved after approximately 7,500 pulses of ablation. The pictures here are taken with the ablation laser attenuated to less than 1% of its full power.

Doppler broadening.

Figure 3.2 shows an energy-level diagram of hyperfine structures for the $X^2\Sigma_{1/2}(v = 0, N = 1)$ and $A^2\Pi_{1/2}(v = 0, j = 1/2^+)$ states. Because of Doppler broadening, the full structure is not resolved and only two features (indicated by red arrows in Figure 3.2) are observed. The levels connected by red arrows represent the energy levels in the absence of nuclear spin and these appear at the weighted average of the full hyperfine energies.

Figure 3.3 shows the strength of the absorption signal as the frequency of the absorption laser is scanned across a 4000-MHz range centred on the $X^2\Sigma_{1/2} \rightarrow A^2\Pi_{1/2}(v = 0, j = 1/2^+)$ transition. To extract a full width at half maximum (FWHM) for the Doppler-broadened resonance, two Gaussian functions are fit to the data with the distance between centres fixed to the difference in frequency between the two transition shown as red arrows in Figure 3.2. The widths of both peaks are forced to be equal in the fits, which effectively assumes that the Doppler-broadening is the same for both transitions. The fit produces a best estimate of 88 MHz for

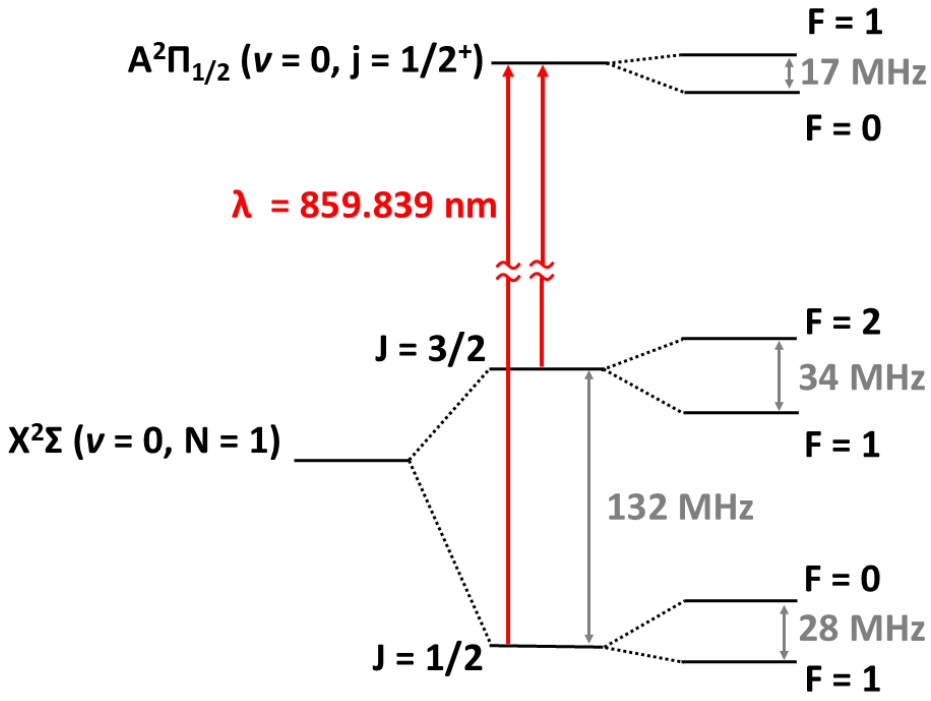


Figure 3.2: Absorption signal energy-level diagram. The red arrows depict the observed transitions during laser absorption measurements. With the exception of the energy difference of the electronic $X^2\Sigma \rightarrow A^2\Pi_{1/2}$ transition, the energy differences between states are drawn to scale. These energies have been calculated [50], and observed experimentally [58, 83].

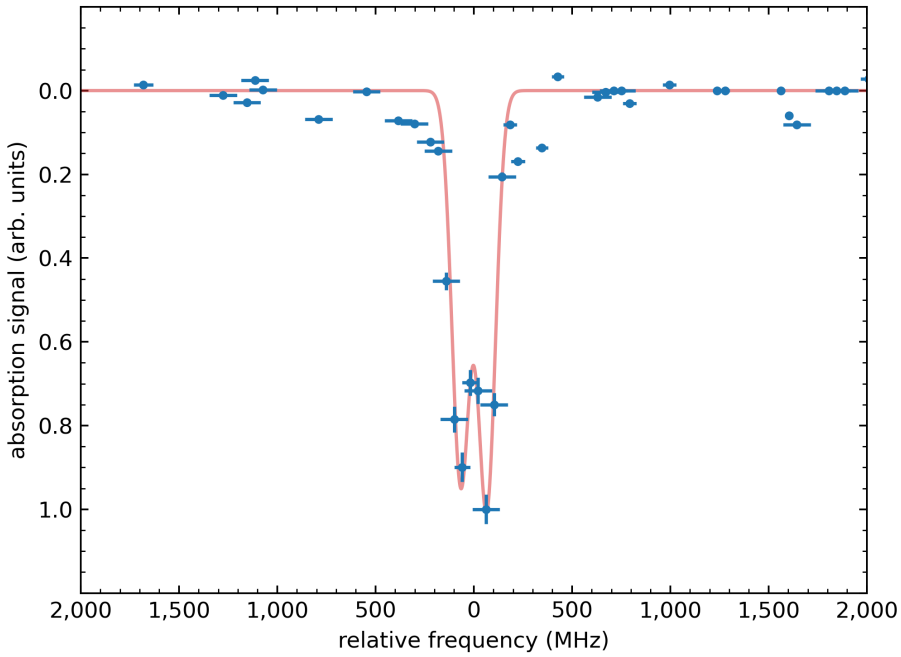


Figure 3.3: Absorption signal versus laser frequency. The observed absorption profile for the molecules exiting the cell. A line of best fit is provided by fitting to two Gaussian peaks of equal width representing the excitation from the $J = 1/2$ and $J = 3/2$ sublevels of the $X^2\Sigma(v = 0, N = 1)$ ground state to the $A^2\Pi_{1/2}(v = 0, j = 1/2^+)$ excited state.

the FWHM of each Gaussian, providing an estimate for the Doppler-broadening. This width is a slight overestimate as the separation between the underlying features is approximately 17 MHz, and so the FWHM of the Doppler-broadened resonance is estimated to be 84(10) MHz. This estimate leads to a range of transverse velocities for the BaF molecules (along the absorption beam axis):

$$v = \lambda(\pm 36(4)\ \text{MHz}) = \pm 31(4)\ \text{m/s}. \tag{3.1}$$

### 3.1.3 *Molecular-beam velocity*

To determine the forward velocity of the beam exiting the cell, the absorption signal is observed at three locations: 0.15 cm, 10 cm, and 20 cm from the output of the buffer-gas cell (as shown in Figure 3.4a). The forward velocity of the molecular beam is determined by observing the time delay between the absorption features at the three locations. The forward velocity of the BaF molecules is found to range between 150 and 300 m/s depending on the flow rate of helium and the temperature of the buffer-gas cell.

The heat deposited into the buffer-gas cell during the ablation process warms the buffer-gas cell to a temperature of 6.8 K. This heat comes from cooling the helium gas, the energy deposited by the pulsed ablation laser, and the deliberate heating of the $SF_6$ gas line. Contamination of the inner surface of the buffer-gas cell can form an insulating layer that results in a helium temperature that is warmer than the operating temperature of the apparatus due to poor thermalisation of the helium gas with the buffer-gas-cell walls. The minimum forward velocity of the BaF molecules exiting the buffer-gas cell during ablation is primarily set by the temperature of the helium gas with which the BaF molecules thermalize.

Figure 3.4b shows an average absorption signal at each of the three locations for 90 ablation laser pulses using a helium flow of 10 sccm through the buffer-gas cell. To estimate the centre of each absorption feature, a 115-$\mu$s rolling average is applied to each trace in Figure 3.4 and the arrival time for the molecules at each location is taken to be the minimum point in the rolling average. Comparing the arrival times (shown as dashed lines in Figure 3.4b) of the molecules at each of

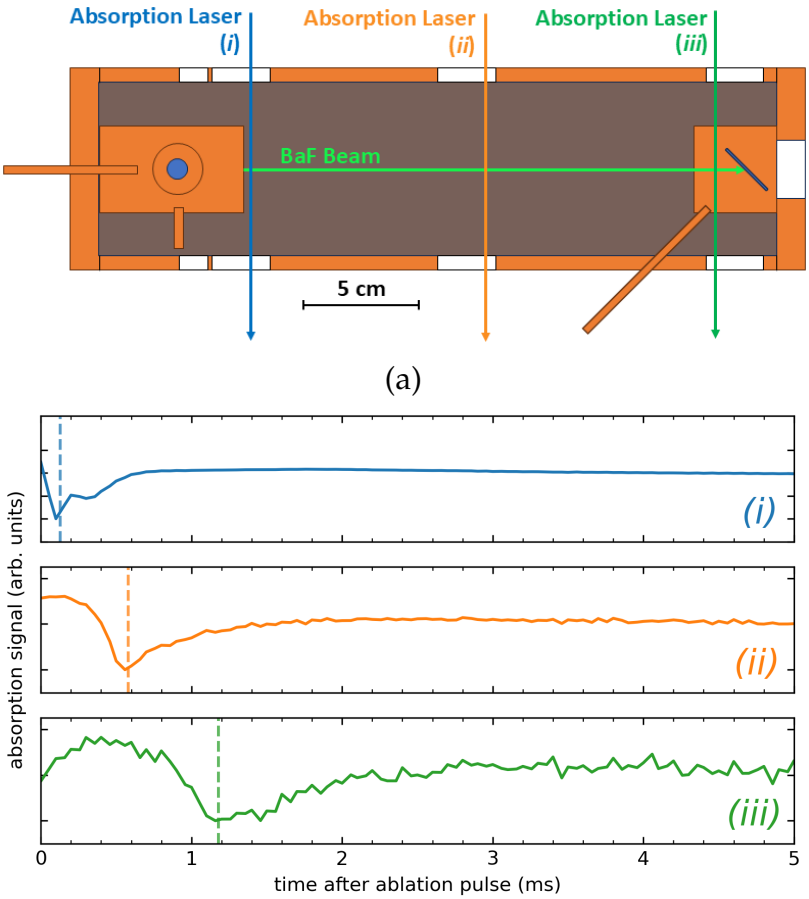


Figure 3.4: Molecular-beam velocity traces. Panel (a) shows the location of the absorption beams: 0.15 cm, 10 cm, and 20 cm from the output of the buffer-gas cell. Panel (b) shows typical absorption signals. The estimated arrival time of the molecules is marked by a dashed line in each plot. The difference between the marked arrival times is used to determine the forward velocity of the molecular beam.

the three locations yields three measurements of the forward velocity: 222 m/s, 191 m/s, and 174 m/s. The average of the measurements gives a best estimate of 190(20) m/s for the forward velocity of the beam of BaF molecules. It is observed that this velocity increases during long growths, which is likely due to the formation of an insulating layer on the surface of the buffer-gas-cell interior that prevents thermalisation with the helium gas.

### 3.1.4 *Calculation of the molecular yield*

Figure 3.5 shows the average absorption signal from 200 ablation pulses for the absorption laser near the output of the buffer-gas cell. Integrating this signal over the region represented by the red band shows that 40 million photons are absorbed by the BaF molecules exiting the cell.

The $X^2\Sigma_{1/2}(v = 0, N = 1) \rightarrow A^2\Pi_{1/2}(v = 0, j = 1/2^+)$ transition forms a closed system due to the fact that it does not lose molecules to other rotational states of the molecule, creating a optical cycling transition. Due to the low intensity of the single-frequency laser used for absorption, the laser

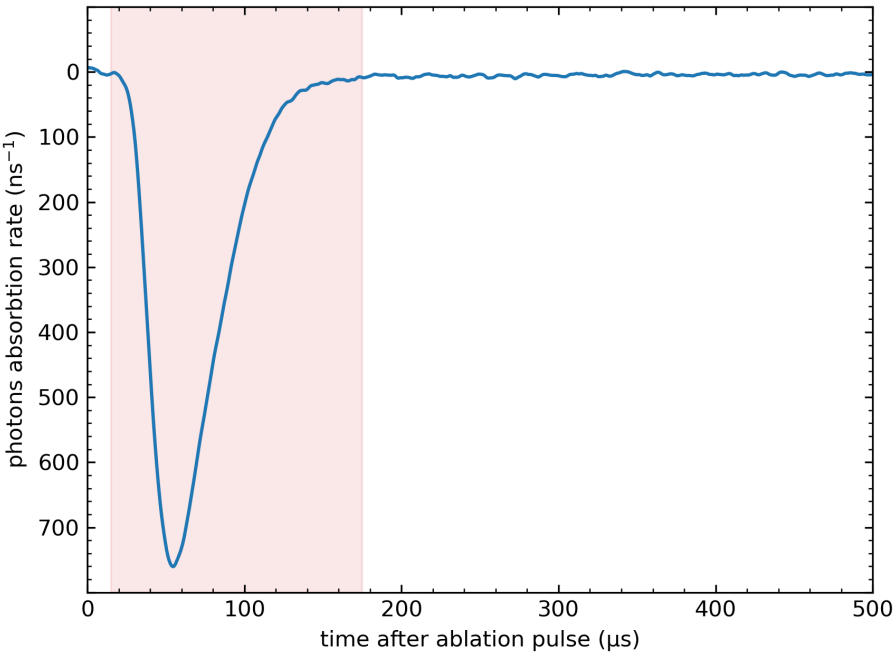


Figure 3.5: Absorption signal for determining BaF molecular yield. The absorption laser is tuned to the $X^2\Sigma_{1/2}(v = 0, N = 1) \rightarrow A^2\Pi_{1/2}(v = 0, j = 1/2^+)$ transition at a distance of 1.5 mm away from the output of the buffer-gas cell. The beam has a low intensity with 10 $\mu$W of laser power and a beam diameter of 1.75 mm. The signal is recorded with an amplified photodiode attached to an oscilloscope and averaged over 200 ablation pulses to produce the trace. The area under the curve within the highlighted region is integrated and provides a measurement of 40 million photons absorbed.

interacts with only one of the four $X^2\Sigma_{1/2}(v = 0, N = 1)$ sublevels of the hyperfine structure (shown in Figure 3.2). The BaF population is quickly pumped into another sublevel which is not in resonance with this laser frequency. This limit on the interaction of the molecules with the laser ensures that the number of photons absorbed per molecule is of order unity. The fraction of BaF molecules exiting the cell in the $X^2\Sigma_{1/2}(v = 0, N = 1)$ state is determined by the thermal distribution of the BaF molecules.

In an ideal buffer-gas cell source, the cell, helium gas, and BaF molecules are in thermal equilibrium and reach the operating temperature of the buffer-gas cell (6.8 K for this system). However, imperfect thermalisation between the cell and buffer-gas may be caused by the formation of an insulating layer of contamination of the cell created by excess ablation particulate. To obtain a more accurate estimation of the temperature of the molecules at the output of the buffer-gas cell, the result obtained in Section 3.1.2 is used, where a Doppler-broadened resonance of 84(10) MHz is observed for the $X^2\Sigma_{1/2}(v = 0, N = 1) \rightarrow A^2\Pi_{1/2}(v = 0, j = 1/2^+)$

transition.

This broadening of the transition is well beyond the natural linewidth and is caused by the transverse velocity of the molecules and from this velocity, an implicit temperature of $14(3)$ K is calculated for molecules exiting the buffer-gas cell. This temperature implies that the vast majority of the BaF molecules exiting the buffer-gas cell should be in the ground vibrational state with approximately 10% of the molecules in the $N = 1$ rotational state that the absorption laser interacts with.

To estimate the average number of photons absorbed per BaF molecule, density-matrix calculations are performed by EDM$^3$ collaborators (similar calculations by collaborators can be found in Ref. [74, 75]). These density-matrix calculations include a full Monte-Carlo simulation for a range of velocities (for molecules with a thermal distribution centred at 8.5 K combined with a forward velocity of $250(50)$ m/s) and initial positions for BaF molecules exiting the buffer-gas cell. These simulations account for the transit time of the molecules within the 1.75 mm Gaussian laser beam and provide an

estimate of 0.049 photons absorbed per BaF molecule exiting the buffer-gas cell in the correct vibrational and rotational levels of the electronic ground state.

Combining the photons absorbed per molecule in the $N = 1$ rotational state from the density-matrix calculation and the total fraction of molecules expected within this rotational level the total molecular output from the cell is calculated to be 9 billion molecules per pulse of the ablation laser.

Alternatively, it can be stated that 30 billion molecules per pulse per steradian are in the $X^2\Sigma_{1/2}(v = 0, N = 1)$ state. This estimate is within a factor of two of previously observed [73] values for a buffer-gas cell of this type.

For a solid grown over the course of 1 hour with a steady ablation rate of 5 Hz, this result indicates that a total of $10^{11}$ molecules per $mm^2$ are directed at the substrate, 20 cm downstream, during deposition.

### 3.2.1 *Deposition rate and conditions*

To better understand the ideal growth parameters, the laser-induced fluorescence produced from implanted BaF molecules within the matrix is studied as a function of various parameters associated with growth. Table 3.2 summarizes the parameter space explored and the optimal growth characteristics, as inferred from fluorescence resulting from the $X^2\Sigma_{1/2}(v = 0) \rightarrow A^2\Pi_{1/2}(v = 0)$ excitation of BaF molecules within the matrix.

### 3.2.2 *Implantation and growth procedure*

To start the growth procedure, the $SF_6$ gas line is warmed to 300 K to prevent freezing of $SF_6$ gas. Next, neon flow is established for 2 minutes (before $SF_6$ and He flows begin and before ablation starts) to form a base layer of pure neon solid on the substrate. After these 2 minutes, the flow of helium is established through the buffer-gas cell followed quickly by the start of $SF_6$ flow. Once all gas flows are established, the

| Growth Parameter | Range Explored | Optimal |
|---|---|---|
| Helium Flow (sccm) | 1 to 12 | 10 |
| $SF_6$ Flow (sccm) | 0.06 to 1 | 0.06 |
| Neon Flow (sccm) | 4 to 30 | 20 |
| Substrate temperature (K) | 6 to 11 | 6.8 |
| Growth duration (minutes) | 20 to 190 | 60 |
| Ablation Laser Pulse Rate (Hz) | 0.2 to 10 | 5 |
| Ablation Laser Pulse Energy (mJ) | 0.9 to 90 | 27 to 90 |

Table 3.2: Summary of growth parameter settings. A list of the parameter space explored during the production of BaF implanted neon matrices and the settings used for optimal growth of BaF-doped neon solids. Optimization for these parameters was done based on laser-induced fluorescence (from molecules within the matrix) and laser absorption from molecules exiting the buffer-gas cell during the growth procedure.

ablation begins by having pulses of focused Nd:YAG laser light be incident on the barium rod within the buffer-gas cell (see Figure 2.1). During the growth period parameters are adjusted (based on feedback from the laser absorption and laser-induced fluorescence signals) to optimize the implantation of BaF molecules into the neon matrix.

The ablation spot on the barium rod is relocated approximately every 25 minutes (approximately 7,500 pulses of ablation laser light) to a fresh area of barium to preserve the efficacy of the buffer-gas cell. Once the desired growth time is reached, the ablation laser and flow of $SF_6$ gas are halted. Thirty seconds after the flow of $SF_6$ is turned off, the helium flow is turned off. The neon gas flow is stopped 2 minutes after the flow of helium has been shut off to form a protective layer of pure neon solid to shield the confined BaF molecules from impurities that may accumulate on the surface over the days, weeks, or months that experiments are performed on the doped matrix. Once growth is complete, the components of the system cool to a base temperature (5 K to 6.5 K, depending on the details of the experimental setup).

During the growth, the laser-induced fluorescence signal from the solid is continuously monitored using a 300-mW, 1-mm ($1/e^2$ ) diameter excitation laser tuned to 859 nm which is on resonance with the $X^2\Sigma_{1/2}(v = 0) \rightarrow A^2\Pi_{1/2}(v = 0)$ transition for BaF molecules within a neon matrix. The QE Pro spectrometer is used to observe the laser-induced fluorescence spectrum and this spectrometer is calibrated across all wavelengths by the procedure described in Section 2.6.2. Additionally a wavelength filter is placed in front of the spectrometer to block light with wavelengths shorter than 900 nm, with an additional notch filter at 1064 nm to specifically attenuate light from the ablation laser. The observed fluorescence determines the effectiveness of the implanting procedure.

Figure 3.6 shows a signal collected from a typical growth. The dashed lines indicate the times when (1) ablation is started, (2) the ablation laser is scrolled over to a fresh spot on the surface of the barium rod, (3) the ablation laser is turned off, and (4) the neon gas flow is turned off (indicating the end of the growth procedure). The final increase in fluorescence present in Figure 3.6 results from the cooling of the matrix

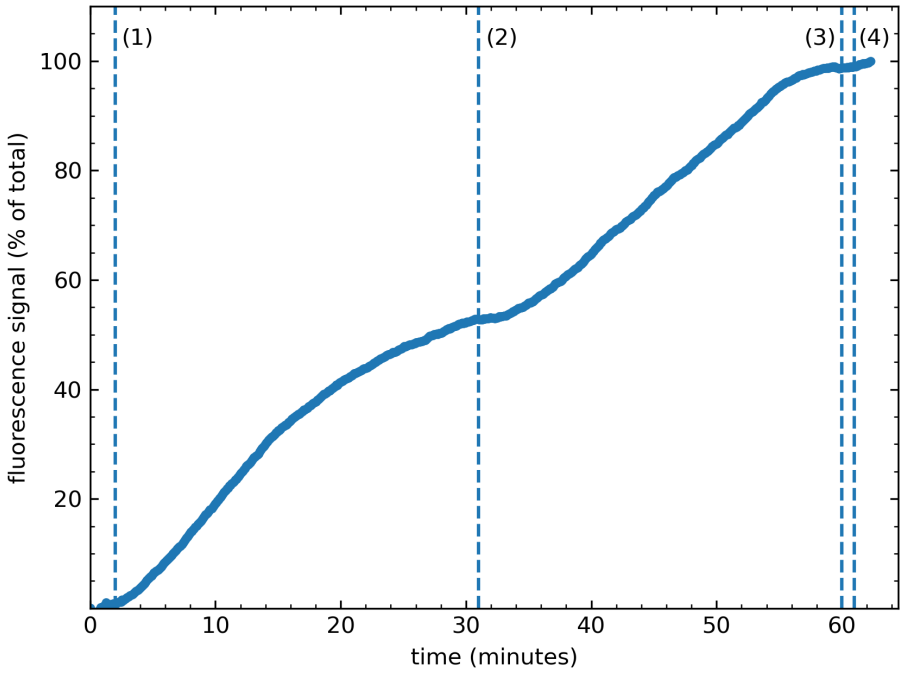


Figure 3.6: Fluorescence versus time for growth of a BaF-doped neon matrix. This data is from a typical growth of BaF-doped neon matrix. The dashed lines show events in which an intervention was performed on the matrix. From left to right these events are: (1) the ablation laser begins pulsing, (2) the ablation laser is scrolled to a fresh spot on the barium rod, (3) the ablation laser is turned off, and (4) the neon gas flow is turned off.

due to the reduced heat load after the gas flows and the $SF_6$ gas line heater are turned off.

### 3.2.3 *Fluorescence signatures from unannealed solids*

After the solid is grown and fully cooled, laser-induced fluorescence experiments continue to characterize the properties of the BaF-doped neon solid. The calibrated QE Pro spectrometer is used to observe the laser-induced fluorescence spectrum that results at each excitation wavelength. A combination of several wavelength filters is used to attenuate unwanted scattered light in a band of approximately 10 nm around the excitation-laser wavelength. The results presented here are focused on the fluorescence wavelength regions where BaF-doped-neon laser-induced fluorescence signals have been identified.

Figure 3.7 shows the fluorescence of a freshly-grown solid when excited at 859 nm, which corresponds to the $X^2\Sigma_{1/2}(v = 0) \rightarrow A^2\Pi_{1/2}(v = 0)$ transition (see Table 3.3). Slightly different growth parameters can strongly affect the observed fluorescence signatures and so a fluorescence spectrum is

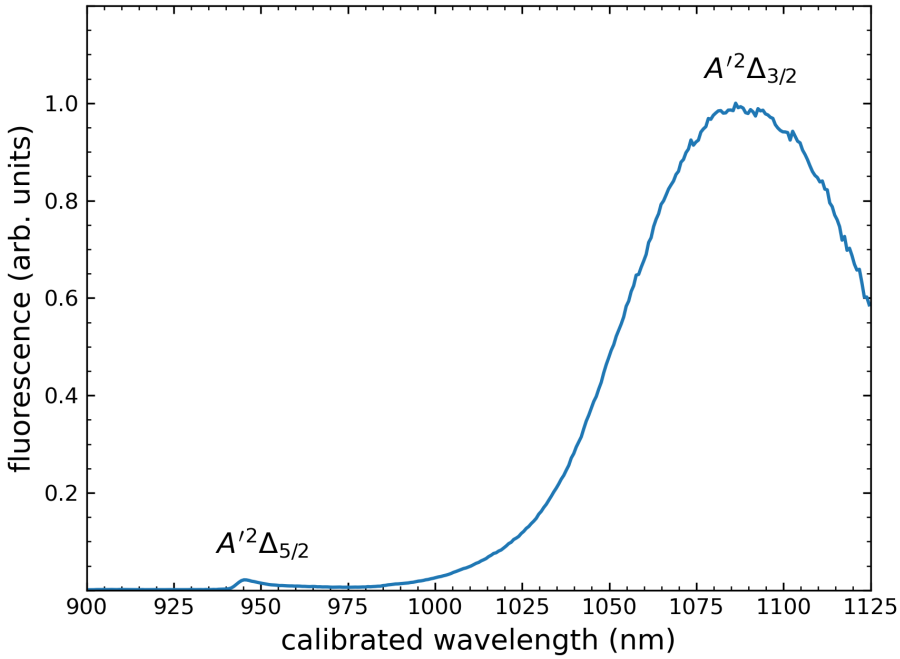


Figure 3.7: Laser-induced fluorescence from excitation to the $A^2\Pi_{1/2}(v = 0)$ state after growth. The excitation laser is tuned to 859 nm to excite the $X^2\Sigma_{1/2}(v = 0) \rightarrow A^2\Pi_{1/2}(v = 0)$ transition of BaF molecules within neon. This fluorescence is monitored during growth to measure the rate of BaF implantation within the solid. The fluorescence peaks at 950 nm and 1080 nm and are due to the $A^2\Pi_{1/2}(v = 0)$ molecules that decay through the $A'^2\Delta_{5/2}$ and $A'^2\Delta_{3/2}$ states. Note that the fluorescence ends at 1125 nm due to the limitations of the QE Pro spectrometer used for this experiment, the spectrometer is calibrated as discussed in Section 2.6.2.

taken after a fresh solid is grown to quickly ascertain its characteristics.

As a control test a growth with typical growth parameters is performed, with the exception that no $SF_6$ gas is flowing, rendering it impossible to form BaF molecules. By observing the fluorescence from this solid as a function of wavelength, laser-induced fluorescence from barium (and, possibly, other ablation by-products) is identified. The fluorescence from the control-test solid helps to identify the laser-induced fluorescence cause by laser-excitation of BaF molecules within the solid.

Figure 3.8 shows a comparison of the fluorescence spectra versus excitation wavelength for this control test (Figure 3.8a) and for a BaF-doped neon solid (Figure 3.8b). Although the control test appears to have no signal, a closer look (Figure 3.9) shows a very small fluorescence feature at approximately 905 nm that is excited by laser light at 863 nm. This feature has some overlap in its excitation profile with a nearby feature due to BaF molecules, however the overall signal is orders of magnitude smaller than the BaF laser-induced fluo-

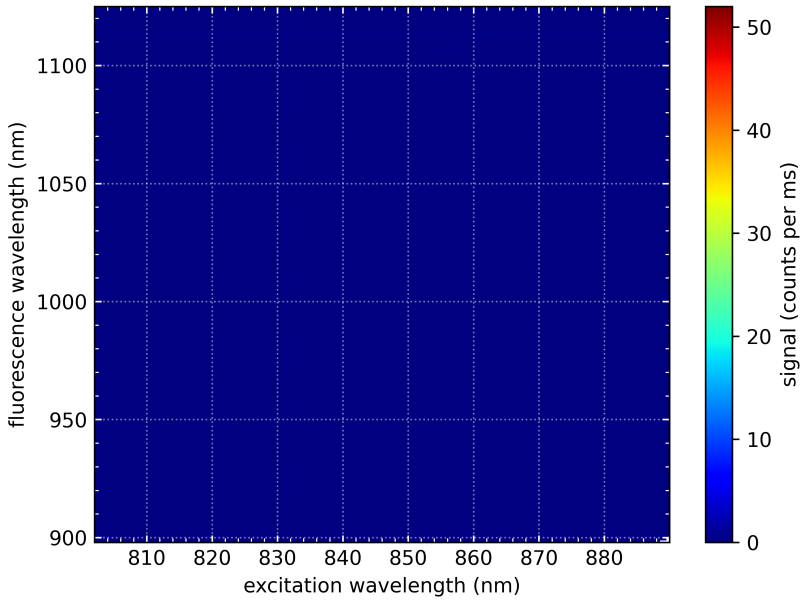


(a) A control solid without BaF

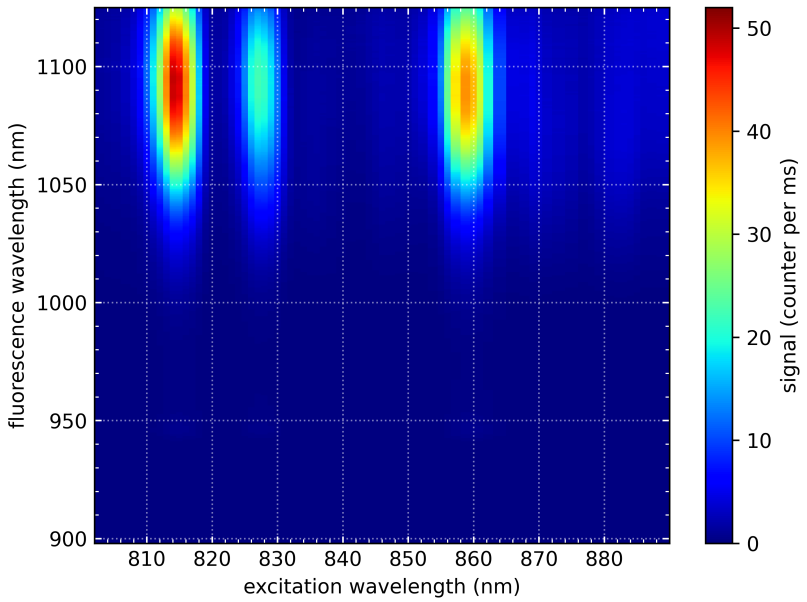


(b) A typical unannealed BaF-doped solid

Figure 3.8: Barium signals in a neon matrix. Panel (a) shows laser-induced fluorescence from the control solid in with no BaF is present. Panel (b) shows the laser-induced fluorescence with BaF-molecules in the neon solid.

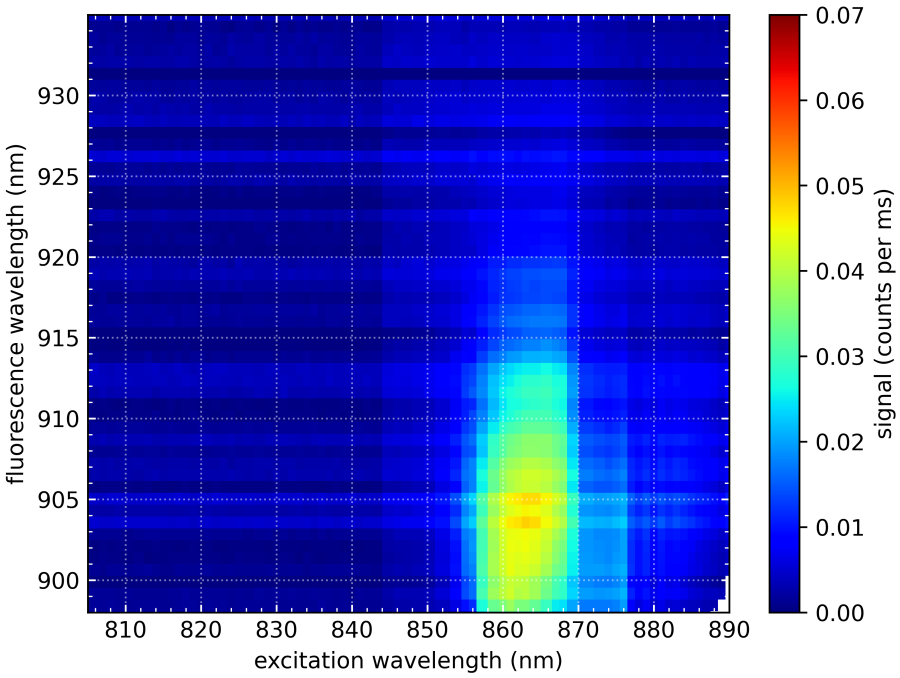


Figure 3.9: Barium signals in a neon matrix with magnified colour scaling. The fluorescence from the control solid is shown with a focus on the region containing the only discernible feature within the wavelength scan region of Figure 3.8. This figure presents the same data set as in Figure 3.8a with the colour map adjusted to highlight the much smaller laser-induced fluorescence feature attributed to barium within a neon matrix.

rescence from solids. Filtering fluorescence in this wavelength region ensures that the fluorescence from barium is minimized when studying transitions for BaF molecules within neon solids.

### 3.2.4 *Annealing procedure*

After growth, the solid is annealed by warming to 8.4 K at a constant rate of 2 K per minute. The solid is left at 8.4 K for 5 minutes, it is then cooled (at 2 K per minute) to the base temperature. The slow rates of heating and cooling prevent the solid from cracking or lifting from the sapphire substrate, which could otherwise result from the different rates of thermal expansion of the sapphire substrate and the neon matrix.

Figure 3.10 shows the integrated fluorescence (from 950 to 970 nm) versus excitation wavelength before (Figure 3.10a) and after (Figure 3.10b) a single annealing cycle. This annealing procedure changes the amount of laser-induced fluorescence observed when exciting the various transitions of BaF, notably causing the $X^2\Sigma_{1/2} \rightarrow A^2\Pi_{1/2}(v = 0)$ excitation to become the largest feature within the observed

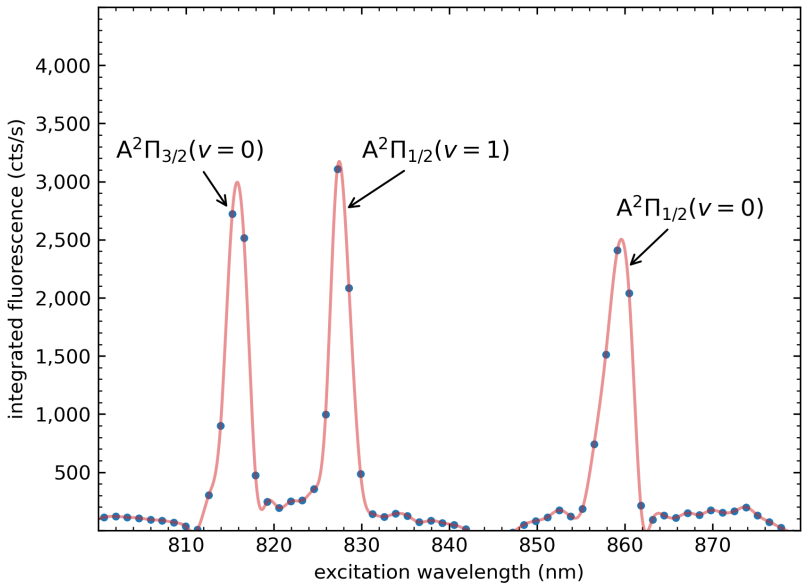


(a) fluorescence before annealing

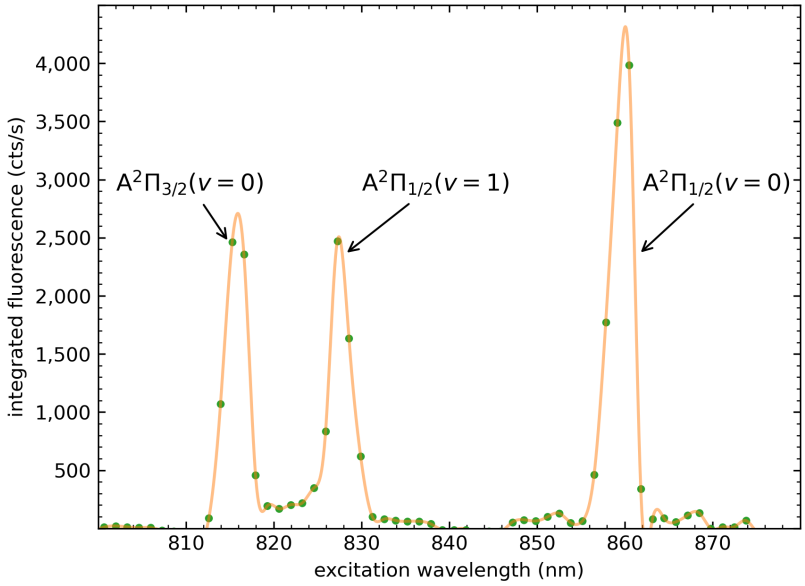


(b) fluorescence after an annealing cycle

Figure 3.10: Annealing effects on BaF fluorescence. Panel (a) shows the fluorescence signal before annealing. Panel (b) shows the fluorescence signal after a single annealing cycle. The solid lines serve as a guide for the eye.

excitation spectrum. The annealing procedure is repeated until no change in fluorescence signal is observed. Due to the differing thickness of neon solids grown, the number of cycles required to anneal the solid varies. After annealing, the solid has laser-induced fluorescence that is stable over long periods of time and many repeated experiments.

## 3.3 BaF fluorescence in neon

### 3.3.1 *Identified excited states for BaF in neon*

Once a matrix is grown and annealed, laser wavelengths ranging from 700 to 1000 nm (the range of the titanium-sapphire laser) are used to observe laser-induced fluorescence. Laser-induced fluorescence within the wavelength range of 350 to 2500 nm (with the exception of a region within approximately $\pm 10$ nm of the excitation laser light, where scattered laser light overlaps the fluorescence) is observed by implementation of the two spectrometers described in Section 2.6.2.

Figure 3.11 shows the result of an excitation laser wavelength scan for the integrated laser-induced fluorescence (as

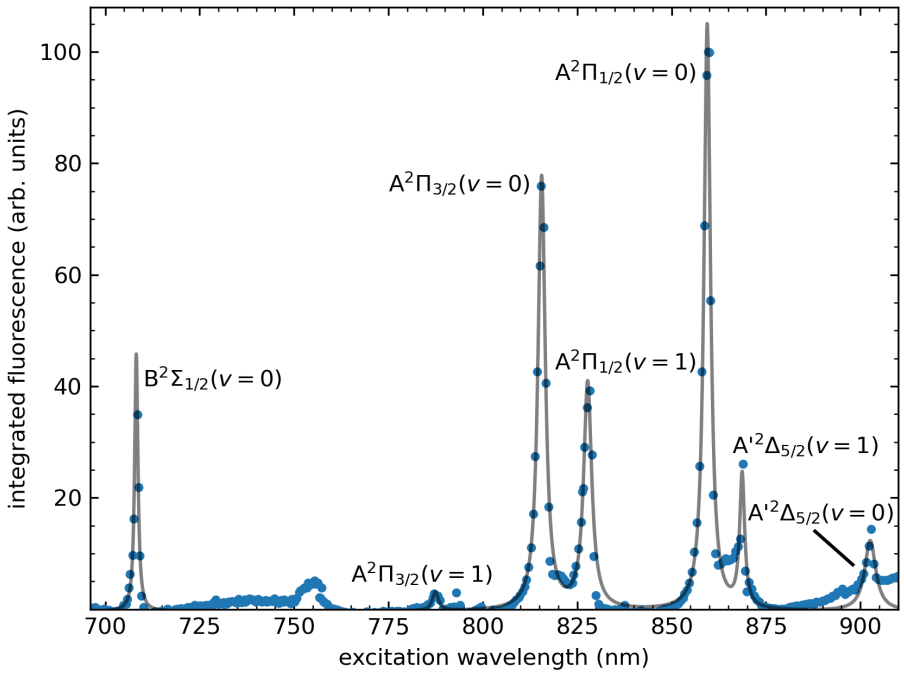


Figure 3.11: Excitation spectrum of BaF in neon. The integrated fluorescence (from 950 to 970 nm) from the BaF-doped matrix corresponds to decay from $A'^2\Delta_{5/2} \rightarrow X^2\Sigma$. Each peak is fit to a Lorentzian lineshape and these fits determine the FWHM and centres reported in Table 3.3.

measured on a QE Pro spectrometer) for the wavelength range spanning 950 to 970 nm. The excitation laser is held at a laser power of 200 mW, with a beam diameter of 45 $\mu$m. The solid line is a fit to each feature using Lorentzian lineshapes. Table 3.3 summarizes the observed excited states for BaF molecules confined within the neon matrix and the comparison to the identified states to their free-molecule counterpart.

The electronic excitation transitions for BaF molecules within neon share some characteristics. The FWHM of each excitation is comparable at approximately 30(10) $cm^{-1}$. Additionally, all higher-energy $B^2\Sigma$ and $A^2\Pi$ states have decay paths through the $A'^2\Delta_{5/2}$ and $A'^2\Delta_{3/2}$ states within the matrix as identified by fluorescence from 945 to 970 nm and 1000 to 1400 nm, respectively (similar to the fluorescence shown in Figure 3.7).

Further high-resolution spectra are taken of the $X^2\Sigma_{1/2} \rightarrow B^2\Sigma_{1/2}(v = 0)$ and $X^2\Sigma_{1/2} \rightarrow A^2\Pi_{1/2}(v = 0)$ transitions as shown in Figure 3.12. Both use the integrated fluorescence from the $A'^2\Delta_{3/2}$ state decay path (as measured with the calibrated QE Pro spectrometer, using integrated fluorescence

| Excited State | Free (nm) | Confined (nm) | Shift ($cm^{-1}$) | FWHM ($cm^{-1}$) |
|---|---|---|---|---|
| $B^2\Sigma_{1/2}$ $(v=0)$ | 712.24 | 708.22(6) | 79.65(5) | 21(3) |
| $A^2\Pi_{3/2}$ $(v=1)$ | 787.62 | 787.4(10) | 2.92(11) | 30(8) |
| $A^2\Pi_{3/2}$ $(v=0)$ | 815.50 | 815.59(6) | $-1.37(5)$ | 35(3) |
| $A^2\Pi_{1/2}$ $(v=1)$ | 828.86 | 827.78(12) | 15.52(11) | 37(6) |
| $A^2\Pi_{1/2}$ $(v=0)$ | 859.83 | 859.44(8) | 5.35(9) | 28(1) |
| $A'^2\Delta_{5/2}$ $(v=1)$ | 864.63 | 868.69(18) | $-54.10(36)$ | 21(7) |
| $A'^2\Delta_{5/2}$ $(v=0)$ | 898.40 | 902.62(15) | $-51.99(21)$ | 43(6) |

Table 3.3: Summary of identified electronic transitions for BaF within neon. the transitions are identified using laser-induced fluorescence (see Figure 3.11) of BaF molecules confined within a neon matrix. All states reported here are excited from the $X^2\Sigma_{1/2}(v=0)$ ground state. All identified states within the matrix have a FWHM consistent with $30 \pm 10$ $cm^{-1}$. The line centres for the excitation are shifted with respect to the free molecule.

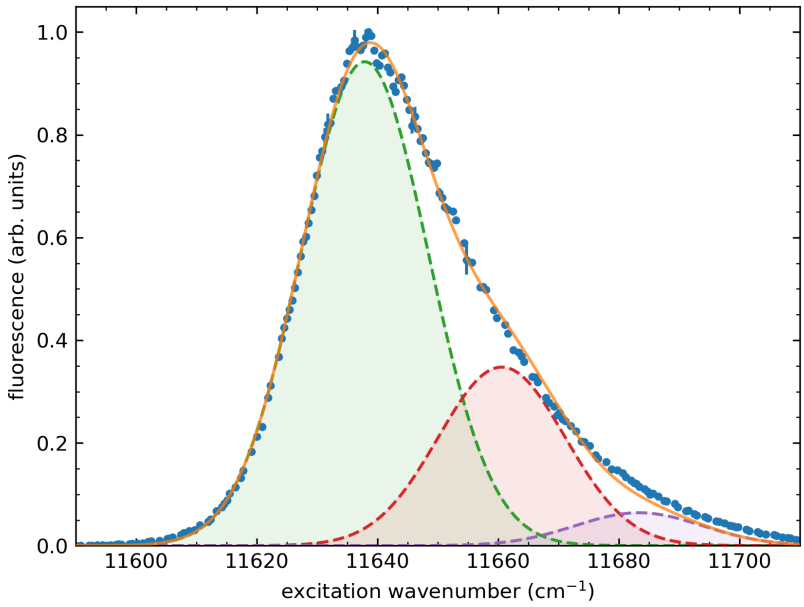


(a) $X^2\Sigma_{1/2} \rightarrow A^2\Pi_{1/2}(v = 0)$

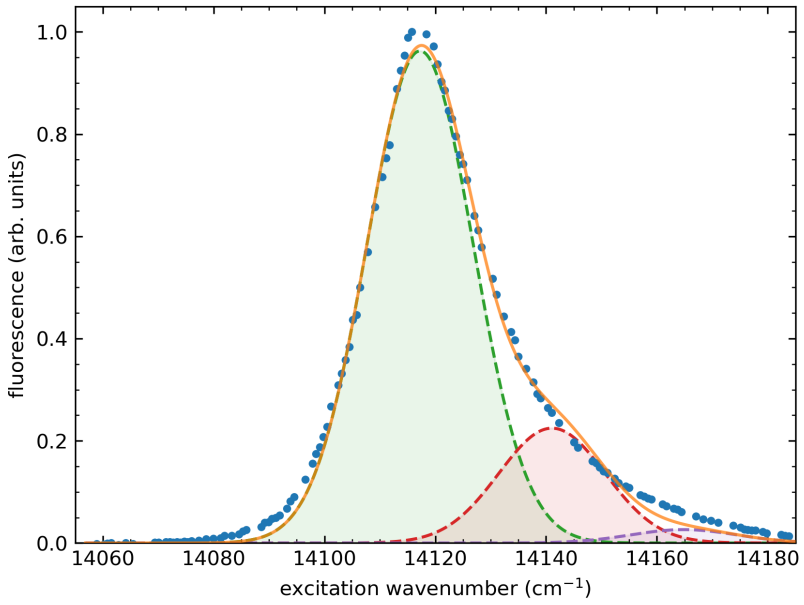


(b) $X^2\Sigma_{1/2} \rightarrow B^2\Sigma_{1/2}(v = 0)$

Figure 3.12: Excitation profiles for selected states of BaF in neon. Panel (a) shows the excitation profile for the $A^2\Pi_{1/2}(v = 0)$ state. Panel (b) shows the excitation profile for the $B^2\Sigma_{1/2}(v = 0)$ state. The solid lines are a fit of the form of Equation 3.2.

from the wavelength range spanning 1000 to 1100 nm) plotted as a function of excitation laser wavelength with a resolution of approximately 0.03 nm. The excitation profiles are fit to a model, similar to that presented in Ref. [84] by EDM$^3$ collaborators, of the form

$$f(x) = \sum_{n=0}^{2} \frac{S^n e^{\frac{-(x-v_0-nv_p)^2}{2\sigma^2}} e^{-S}}{n!\,\sigma\sqrt{2\pi}}, \tag{3.2}$$

where $S$ is the Huang-Rhys factor that parametrizes the strength of the molecules and matrix phonon mode coupling, $v_p$ is the frequency associated with a phonon mode, $\sigma$ is the width of the gaussian lineshape, $v_0$ is the frequency centre of the zero-phonon line. The parameters found in Table 3.4 are similar to the results of the parameters extracted from the comparable fit in Ref. [84] for the excitation profile of molecules excited to the $A^2\Pi_{1/2}(v = 0)$ state.

When a fit of the same form is applied to the excitation profile from the $X^2\Sigma_{1/2}(v = 0) \rightarrow B^2\Sigma_{1/2}(v = 0)$ transition (see in Figure 3.12b), the result is a somewhat poorer fit to the data. This may be an indication that more than one phonon mode plays a role for this transition.

| | $X^2\Sigma_{1/2} \rightarrow A^2\Pi_{1/2}(v=0)$ | $X^2\Sigma_{1/2} \rightarrow B^2\Sigma_{1/2}(v=0)$ |
|---|---|---|
| $S$ | $0.369(8)$ | $0.233(8)$ |
| $v_0$ ($\mathrm{cm}^{-1}$) | $11,637.9(1)$ | $14,117.3(1)$ |
| $v_p$ ($\mathrm{cm}^{-1}$) | $22.7(3)$ | $23.8(4)$ |
| $\sigma$ ($\mathrm{cm}^{-1}$) | $10.53(8)$ | $9.6(1)$ |

Table 3.4: Summary of high-resolution excitation spectrum fit parameters. These parameters correspond to a fit of the form of Equation 3.2 to the data presented in Figure 3.12. The parameters observed for the $X^2\Sigma_{1/2} \rightarrow A^2\Pi_{1/2}$ $(v=0)$ are reasonably close to those found for similar data presented in Ref. [84]

### 3.3.2 *Laser-induced fluorescence of the B-state*

When the $X^2\Sigma_{1/2} \rightarrow B^2\Sigma_{1/2}(v = 0)$ transition is excited using a single-frequency laser tuned to 708 nm, the BaF molecules confined within the neon matrix produce fluorescence at several wavelength ranges between 700 to 1400 nm, as the molecules decay back to the ground state. An energy-level diagram for the observed excitation and decay processes is shown in Figure 3.13 . The vast majority of the laser-induced fluorescence observed from excitation to the $B^2\Sigma_{1/2}(v = 0)$ is found within two fluorescence peaks, the first spanning 730 to 736 nm, due to the direct decay from the excited $B^2\Sigma_{1/2}(v = 0)$ state back down to the $X^2\Sigma_{1/2}$ ground state, this fluorescence is shown in Figure 3.14 . The remaining fluorescence is observed in a much broader fluorescence feature spanning from 980 to 1400 nm, due to decay from the intermediary $A'^2\Delta_{3/2}$ state back down to the $X^2\Sigma_{1/2}$, this fluorescence is shown in Figure 3.15.

Figure 3.14 shows the fluorescence from the direct decay of the $B^2\Sigma_{1/2}(v = 0)$ state to multiple ground state vibrational levels, as captured by the calibrated QE Pro spec-

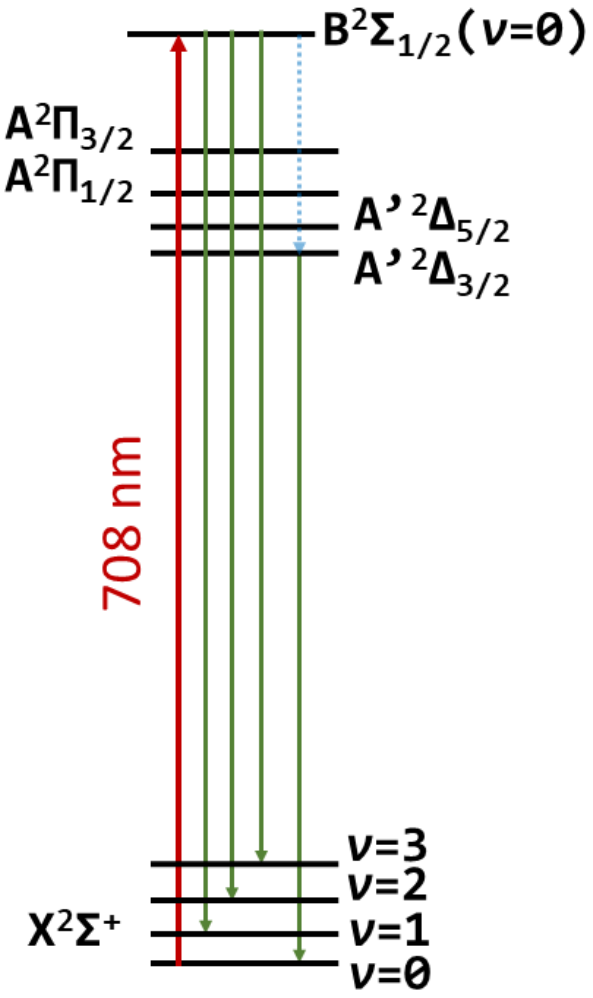


Figure 3.13: Laser-induced fluorescence energy-level diagram for B-state excitation. Fluorescence from radiative decay down to ground state vibrational levels $X^2\Sigma_{1/2}$ ($v = 1, 2, 3$) is observed. Fluorescence to the $v = 0$ vibrational level of the ground state is not observed, as it is too close in wavelength to the excitation laser. Fluorescence from the $A'^2\Delta_{3/2}(v = 0)$ state is observed at longer wavelengths. The latter fluorescence results from a non-radiative decay to the $A'^2\Delta_{3/2}(v = 0)$ state. The energy levels are not drawn to scale.

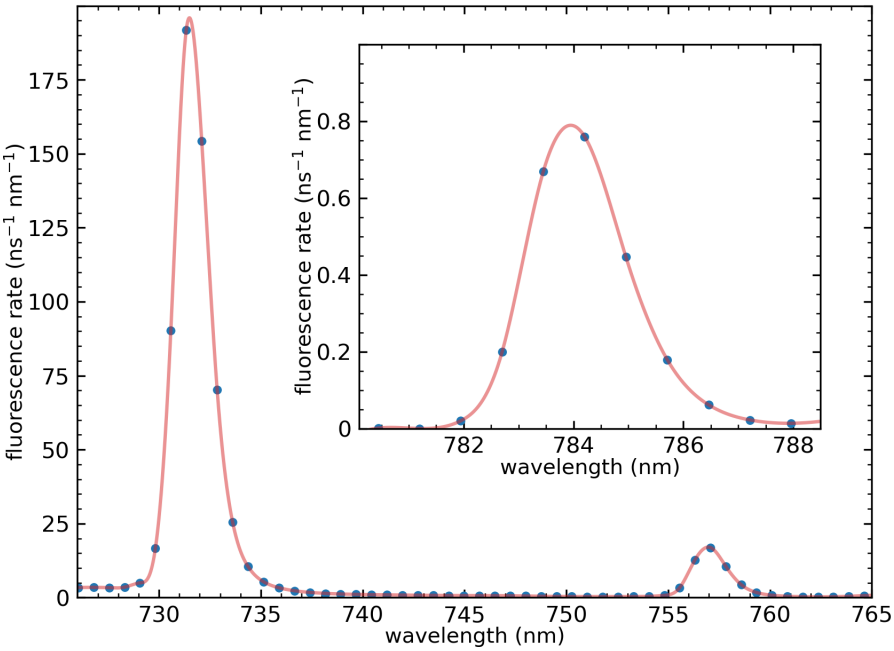


Figure 3.14: Fluorescence produced by decay from the $B^2\Sigma_{1/2}(v = 0)$ state to the $X^2\Sigma_{1/2}(v = 1, 2, 3)$ states. The solid line serves as guide for the eye. The main figure shows the strongest lines produced by decay to the $v = 1, 2$ levels of the ground state, while the inset shows the smaller fluorescence feature corresponding to decay to the $v = 3$ state. The Frank-Condon factors for vibrational transitions between the $B^2\Sigma_{1/2}(v = 0)$ and the $X^2\Sigma_{1/2}(v = 1, 2, 3)$ have been calculated theoretically, for a free BaF molecule [51] and agree with the observed ratios between the observed peak heights.

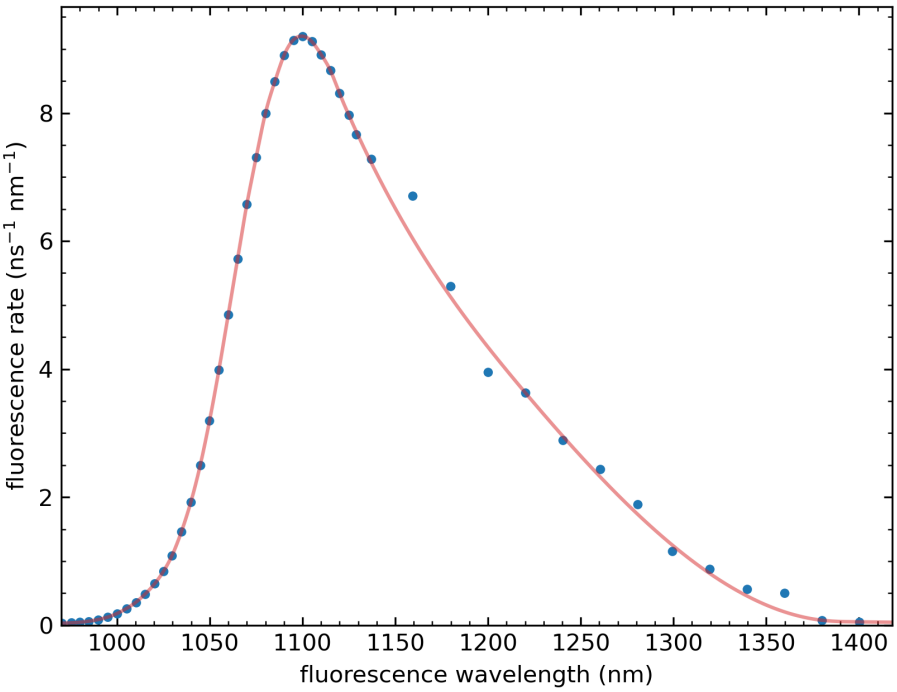


Figure 3.15: Fluorescence of the $B^2\Sigma_{1/2}(v = 0) \rightarrow A'\,^2\Delta_{3/2}$ decay. The fluorescence produced via laser excitation at 708 nm showing the radiative decay of the $A'\,^2\Delta_{3/2} \rightarrow X^2\Sigma_{1/2}$ decay, following the non-radiative $B^2\Sigma_{1/2} \rightarrow A'\,^2\Delta_{3/2}$ decay within the matrix. The solid line serves as a guide for the eye. The data presented in this figure were taken with the QE Pro ( $\lambda < 1130$ nm) and the ATP ( $\lambda > 1130$ nm) spectrometers. Both spectrometers are calibrated using a thermal light source, as discussed in Section 2.6.2.

trometer (see Section 2.6.2). The dominant fluorescence feature for decay of the $B^2\Sigma_{1/2}(v = 0)$ state to the ground $X^2\Sigma_{1/2}$ state is centred at 732 nm with, two smaller peaks at longer wavelengths (757 nm and 784 nm). The peaks shown in Figure 3.14 are identified as the decay from the $B^2\Sigma_{1/2}(v = 0)$ into vibrationally excited levels of the ground state: $X^2\Sigma_{1/2}(v = 1)$, $X^2\Sigma_{1/2}(v = 2)$, and $X^2\Sigma_{1/2}(v = 3)$. In Ref. [51], the branching ratios for the decay from the $B^2\Sigma_{1/2}(v = 0)$ state to the $X^2\Sigma_{1/2}(v = 1, 2, 3)$ electronic ground states are calculated for a free BaF molecule to be 18%, 2%, and 0.1%. Therefore, the expected relative ratios for these features are $R_{12} = 18\%/2\% = 9$, and $R_{13} = 18\%/0.1\% = 180$. Integrating the signal observed in Figure 3.14 yields a relative ratio for the observed fluorescence features of $R_{12} = 11$, and $R_{13} = 180$. The level of agreement between the neon-matrix values with those for the free molecule helps to confirm the identification of the fluorescence features. Direct decay down the $X^2\Sigma_{1/2}(v = 0)$ (which has a calculated branching ratio of 80% for a free BaF molecule) is not observed, as it is very close in wavelength to the excitation laser, and scattered light from this laser obscures the fluorescence peak.

The peaks corresponding to decay to the vibrationally excited ground state levels are found to be separated by 460(1) $cm^{-1}$ and 453(1) $cm^{-1}$ providing a measurement of the effect of the neon matrix on the separation of the $v = 1$-to-$v = 2$ and $v = 2$-to-$v = 3$ vibrational levels of the electronic ground state of the BaF molecule. The energy separation for the vibrational levels of the ground state of BaF for the free molecule can be calculated by modelling the molecule as a quantum harmonic oscillator with anharmonic corrections

$$\frac{E_n}{\hbar} = \omega_e(n+1/2) - x_e\omega_e(n+1/2)^2 + y_e\omega_e(n+1/2)^3, \quad (3.3)$$

where $\omega_e$ is the angular frequency (related to the spring constant and reduced mass of the molecule) of the harmonic oscillator while $x_e\omega_e$ and $y_e\omega_e$ are experimentally determined factors for the anharmonic terms in the series expansion. For a free BaF molecule, these values are [52] $\omega_e = 469.4161(19)$ $cm^{-1}$, $x_e\omega_e = 1.83727(76)$ $cm^{-1}$, and $y_e\omega_e = 0.003295(75)$ $cm^{-1}$. Using Equation 3.3, the spacing from the $v = 1$ to the $v = 2$ vibrational levels of the electronic ground state for the free BaF molecule is 462.11(19) $cm^{-1}$, while the separation between the $v = 2$ and the $v = 3$ vibrational levels is 458.48(19) $cm^{-1}$. The difference between the calculated vibrational spac-

ing for the free BaF molecule and the measured value of those confined within the neon matrix suggests that the matrix imparts a small shift on the ground-state vibrational levels. This method of observing the effect of the matrix is limited by the resolution and absolute accuracy of the spectrometer.

Figure 3.15 shows the laser-induced fluorescence for BaF molecules, excited with 708-nm laser light to the $B^2\Sigma_{1/2}$ state that non-radiatively decays to the $A'\Delta_{3/2}$ state (depicted in Figure 3.13 with the dashed blue arrow) before radiatively decaying to the ground state. This fluorescence is observed with the QE Pro spectrometer for wavelengths shorter than 1130 nm and the ATP8200 spectrometer for longer wavelengths, both spectrometers are calibrated, as discussed in Section 2.6.2. All of the observed fluorescence features in Figure 3.14 and Figure 3.15 have tails on the red side of the peaks that result from decay to phonon states above the $X^2\Sigma_{1/2}$ state. The fluorescence from the $B^2\Sigma_{1/2}$-to-$X^2\Sigma_{1/2}$ decay is shifted to the blue by 5 nm, while the fluorescence from the $A'^2\Delta_{3/2}$-to-$X^2\Sigma_{1/2}$ decay is shifted to the red by 150 nm and is more strongly broadened.

The decay process for BaF molecules excited to the $B^2\Sigma_{1/2}$ state is influenced by the fact that the equilibrium positions of the BaF molecule and its surrounding Ne atoms are different for the $B^2\Sigma_{1/2}$ state than for the ground electronic state (for which the positions were examined theoretically in Ref. [72]). Thus, after laser excitation, the molecule and surrounding atoms quickly adjust their positions. This movement transfers energy to the solid on a timescale that is much faster than radiative decay down to the ground state, the molecule (and surrounding neon atoms) either settle to their equilibrium positions for the $B^2\Sigma_{1/2}$ state (leading to the fluorescence of Figure 3.14) or, in the process of settling, they experience a level crossing that lands them into the lowest-lying excited electronic state of the molecule (leading to the fluorescence shown in Figure 3.15).

### 3.3.3 *The lifetime of the B-state*

Lifetimes are measured by using an acousto-optic modulator (AOM) which sends pulses of excitation-laser light and observing the time profile of the resulting fluorescence, after the laser has been turned off, using a combination of a single-

photon counter and timetagger that are capable of recording single photon arrival times with a resolution of 500 ps (see Section 2.6.4). Because the AOM has a minimum turn-off time of 11 ns, the data from the first 20 ns after the laser is turned off is ignored. The excitation laser is tuned to 708 nm to drive the $X^2\Sigma_{1/2}$ to $B^2\Sigma_{1/2}(v = 0)$ transition, with a beam diameter of 40 $\mu$m and laser power of 500 mW. Wavelength filters are placed in the fluorescence collection optics path to carefully select for fluorescence light in the wavelength region of interest.

Figure 3.16 shows laser-induced fluorescence from molecules excited to the $B^2\Sigma_{1/2}(v = 0)$ as they decay to the $X^2\Sigma(v = 1)$ ground state (depicted with the red and leftmost green arrows for excitation and decay, respectively, on the energy diagram in Figure 3.13), with the observed fluorescence fit to a single exponential function. The observed fluorescence spans from 725 to 750 nm and encompasses the fluorescence feature from the $B^2\Sigma_{1/2}(v = 0)$ state decay to the $v = 1$ vibrational level of the ground state (see Figure 3.14). The lifetime from the fit of this decay is $\tau_b = 37.4(2)$ ns, which is close to the measured value [85] of 41.7(3) ns and the calculated

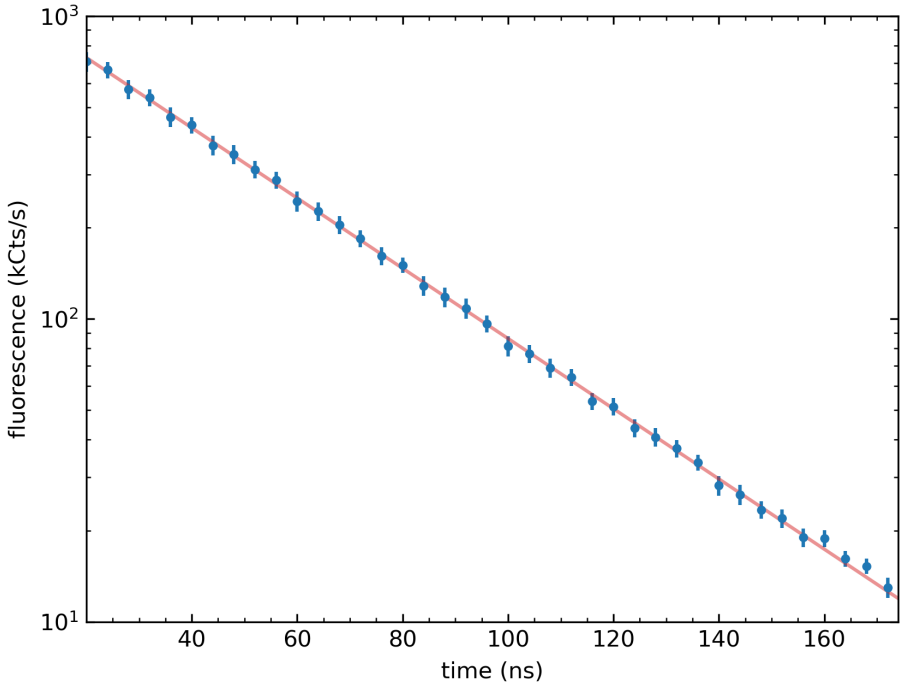


Figure 3.16: Lifetime of direct B-state decay. Fluorescence from 725 to 750 nm is observed, which corresponds to the decay from the $B^2\Sigma_{1/2}(v = 0)$ excited state to the $X^2\Sigma_{1/2}(v = 1)$ ground state. The matrix is held at 5.8 K and the laser is turned off at time $t = 0$. The solid line shows a exponential fit which gives a lifetime of $\tau_b = 37.4(2)$ ns. Note that the $y$-axis is has a logarithmic scale.

value [51] of 37.0 ns for the $B^2\Sigma_{1/2}$ state decay of the free molecule.

### 3.3.4 *Lifetime of observed fluorescence for decay through the $A'^2\Delta_{5/2}$ state*

Excitation of the BaF molecules to the $A^2\Pi_{1/2}(v = 0)$ using 859-nm laser light allows for two distinct decay paths to be observed, as shown in the energy-level diagram in Figure 3.17. The dashed arrows represent the non-radiative process that allows the excited molecules to decay to the lower-lying $A'$ states. From the $A'$ states the molecules decay radiatively (as depicted by the solid green arrows of Figure 3.17). This fluorescence is shown in Figure 3.7, where the majority of the fluorescence occurs in the region from 1000 to 1125 nm. The full fluorescence peak extends beyond the range of the QE Pro spectrometer (to approximately 1400 nm) and is similar to the fluorescence from excitation to the $B^2\Sigma_{1/2}(v = 0)$ shown in Figure 3.15. This fluorescence corresponds to the $A'^2\Delta_{3/2} \rightarrow X^2\Sigma_{1/2}$ decay (see Section 3.3.5), while the small fluorescence feature from 945 to 970 nm corresponds to the

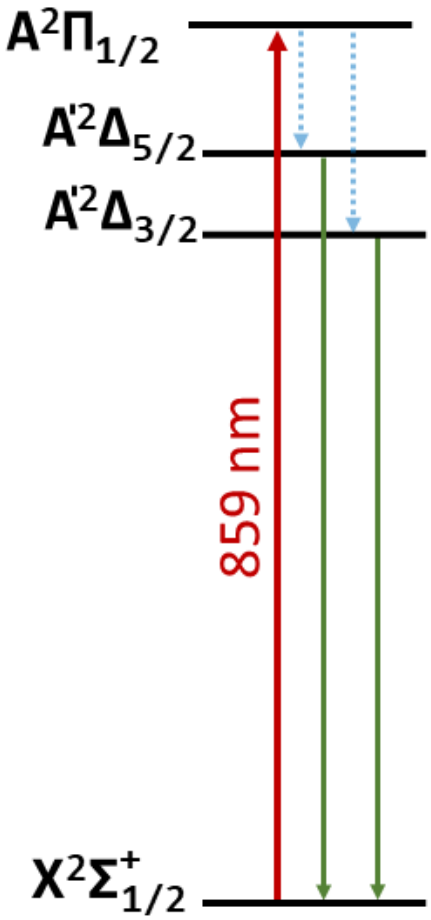


Figure 3.17: Energy-level diagram for excitation and decay of the $A^2\Pi_{1/2}(v = 0)$ state. BaF molecules excited to the $A^2\Pi_{1/2}(v = 0)$ state non-radiatively decay (depicted with the dashed blue arrows) to the $A'^2\Delta_{5/2}$ state and the $A'^2\Delta_{3/2}$ state, followed by radiative decay to the ground state (depicted with the solid green arrows). The two fluorescence features corresponding to the two decay paths are shown in Figure 3.7.

$A'^2\Delta_{5/2} \rightarrow X^2\Sigma_{1/2}$ decay.

Figure 3.18 shows the time profile of the fluorescence from BaF molecules excited to the $A^2\Pi_{1/2}(v = 0)$ state that radiatively decay from the $A'^2\Delta_{5/2}$ state. The fluorescence light is wavelength filtered such that the only light observed is within a band from 950 to 970 nm. The time-decay profile of the excitation light fits reasonably well to a single exponential with a lifetime of $3.92(7)$ $\mu$s.

### 3.3.5 *Lifetimes of observed fluorescence for decay through the $A'^2\Delta_{3/2}$ state*

As in Section 3.3.4, BaF molecules are excited to the $A^2\Pi_{1/2}(v = 0)$ state. To observe the fluorescence that results from the BaF molecules that decay non-radiatively to the $A'^2\Delta_{3/2}$ state before radiatively decaying to the ground state, wavelength filters are used to selectively examine regions within the broad fluorescence feature extending from 1000 to 1400 nm (the relevant portion of this band of fluorescence can be seen in Figure 3.7). Because the single-photon-counter used in the lifetime experiments is only sensitive to light with

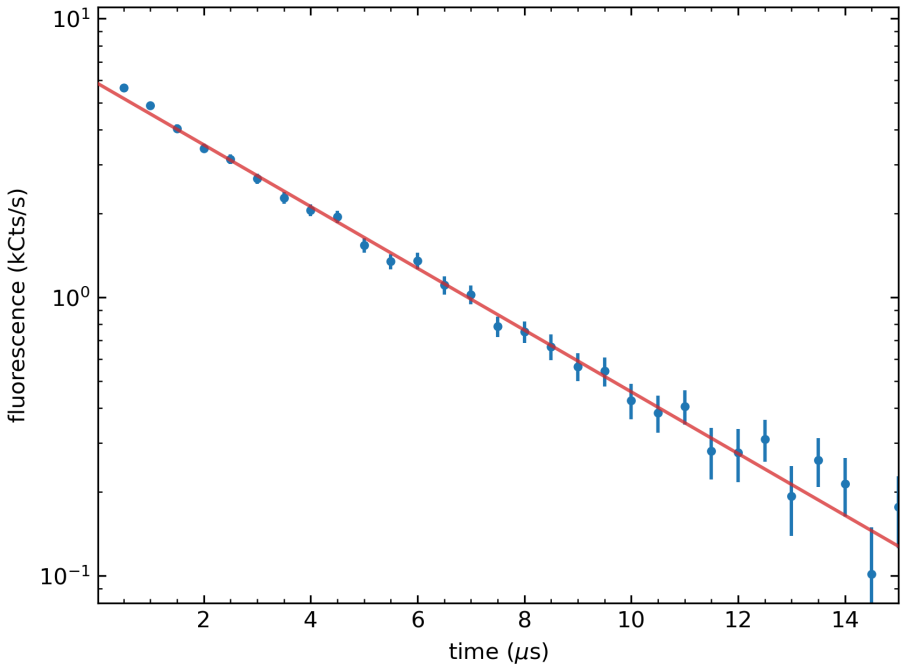


Figure 3.18: Time profile of the radiative decay from the $A'^2\Delta_{5/2}$ state. BaF molecules are excited to the $A^2\Pi_{1/2}(v = 0)$ states with 859-nm laser light and fluorescence is observed in the wavelength region from 950 to 970 nm (see Figure 3.7). The solid line represents an exponential fit with an associated lifetime of $\tau_r = 3.92(7)$ $\mu$s. Note that the $y$-axis has a logarithmic scale.

wavelengths shorter than 1100 nm only the time profile of fluorescence light for wavelengths from 1000 to 1100 nm is examined. It is observed that fluorescence light in this broad wavelength region contains more than a single lifetime and, as such, wavelength filters are used to subdivide the region into smaller, 25-nm wavelength regions.

Figure 3.19 shows time profile of the fluorescence that spans from 1075 to 1100 nm. The solid line is a fit to a sum of two independent exponential functions, with lifetimes labelled $\tau_{\text{short}}$ and $\tau_{\text{long}}$. The two exponential functions are necessary to obtain a reasonable fit to the observed fluorescence time profile. The dashed line shows an extrapolation back to $t = 20$ ns for the single exponential lifetime corresponding to $\tau_{\text{long}}$ and gives a very poor fit at short times. The lifetimes obtained from the fits are $\tau_{\text{short}} = 216(22)$ ns and $\tau_{\text{long}} = 430(24)$ ns, with each exponential contributing approximately equally to the overall fluorescence.

Figure 3.20 shows fluorescence time profile for the wavelength region from 1050 to 1075 nm and Figure 3.21 shows fluorescence time profile for the wavelength region from

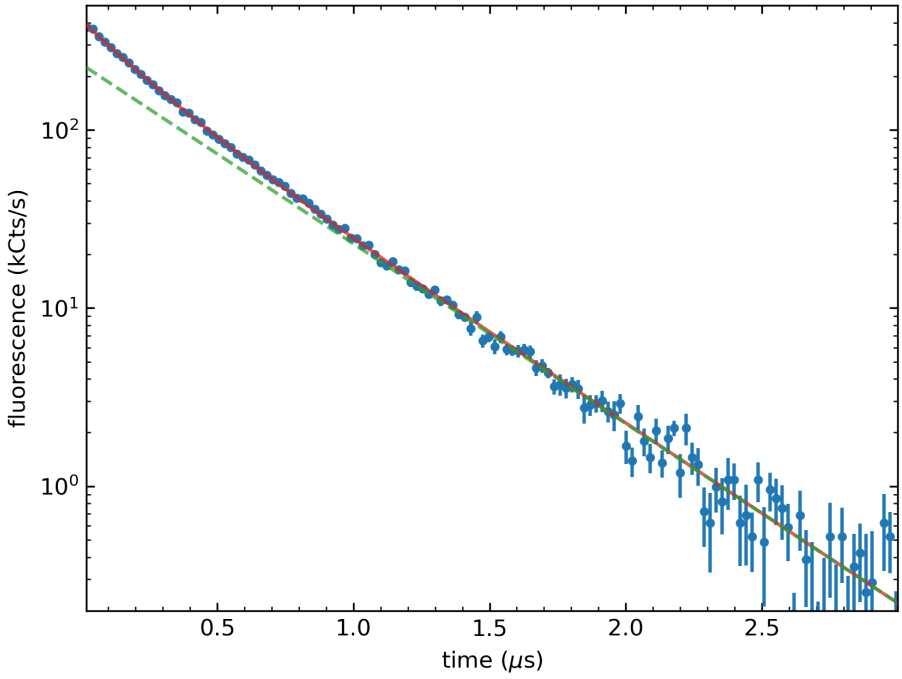


Figure 3.19: Lifetimes of the $A'^2\Delta_{3/2}$ state from fluorescence from 1075 to 1100 nm. The observed fluorescence time profile for BaF molecules excited to the $A^2\Pi_{1/2}$ state that decay from the $A'^2\Delta_{3/2}$ state with fluorescence in the wavelength range from 1075 to 1100 nm. The solid line is a fit to the sum of two exponential functions which determines the time constants $\tau_{\text{short}}$ and $\tau_{\text{long}}$. The fluorescence from each exponential contributes approximately equally to the overall fluorescence. The dashed line represents the exponential function corresponding to $\tau_{\text{long}}$. Note that the $y$-axis is has a logarithmic scale.

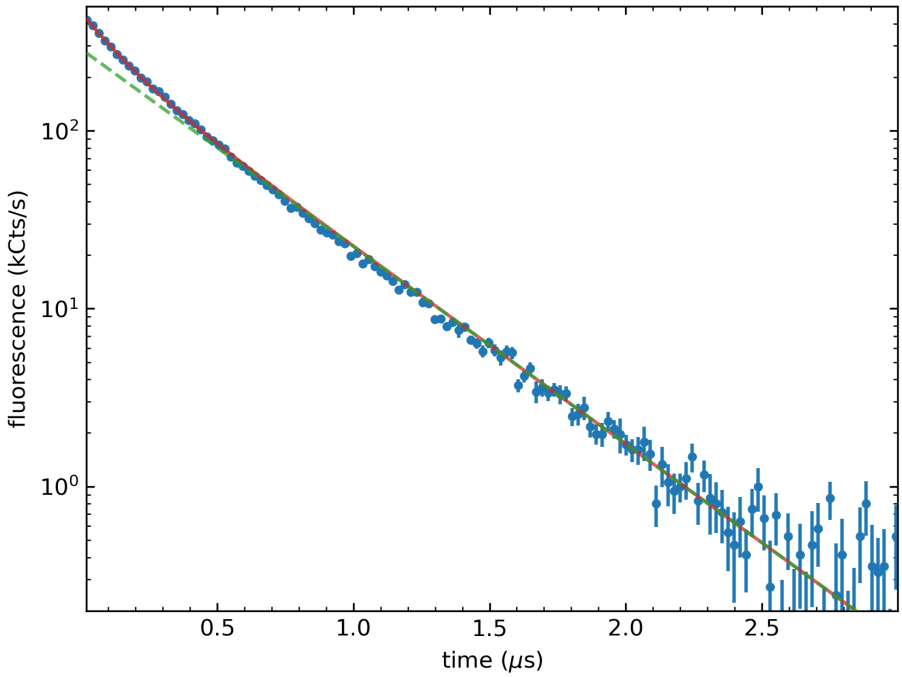


Figure 3.20: Lifetime of the $A'^2\Delta_{3/2}$ state with fluorescence from 1050 to 1075 nm. BaF molecules are initially excited to the $A^2\Pi_{1/2}(v = 0)$ state. The solid line is a fit to the sum of two exponential functions providing a $\tau_{\text{long}}$ and $\tau_{\text{short}}$. The dashed line represents the exponential function corresponding to $\tau_{\text{long}}$. Note that the $y$-axis for both figures has a logarithmic scale.

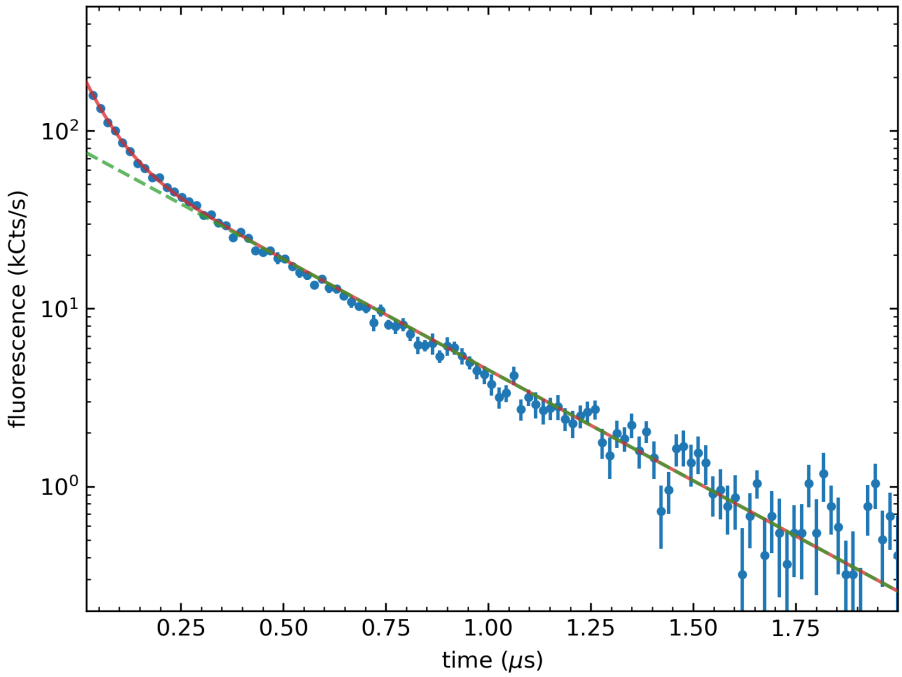


Figure 3.21: Lifetime of the $A'^2\Delta_{3/2}$ state with fluorescence from 1025 to 1050 nm. BaF molecules are initially excited to the $A^2\Pi_{1/2}(v = 0)$ state. The solid line is a fit to the sum of two exponential functions providing a $\tau_{\text{long}}$ and $\tau_{\text{short}}$. The dashed line represents the exponential function corresponding to $\tau_{\text{long}}$. Note that the $y$-axis for both figures has a logarithmic scale

1025 to 1050 nm. The solid line in Figure 3.20 represents a fit to a sum of two exponential functions whose associated lifetimes are $\tau_{\text{short}} = 139(16)$ ns and $\tau_{\text{long}} = 391(31)$ ns. Similarly, the solid line Figure 3.21 represents a fit to a sum of two exponential functions with corresponding lifetimes of $\tau_{\text{short}} = 64(2)$ ns and $\tau_{\text{long}} = 349(20)$ ns. In each case, both exponential contribute approximately equally to the observed fluorescence.

The lifetime for the decay from the $A'^2\Delta_{3/2}$ state for molecules excited into the $B^2\Sigma_{1/2}(v = 0)$ state is observed in the same way as in Section 3.3.3 with wavelength filters to observe fluorescence light from 1075 to 1100 nm. Figure 3.22 shows the time profile of this decay, with the solid line being a fit to a sum of two exponential functions with associated time constants of $\tau_{\text{short}} = 196(13)$ ns and $\tau_{\text{long}} = 431(10)$ ns. Again, the two exponential functions are found to contribute approximately equally to the overall fluorescence observed.

Table 3.5 summarizes the lifetimes obtained from the $A'^2\Delta_{3/2}$ state decay. It seems likely that the actual decay has a near continuum of lifetimes associated with the broad fluores-

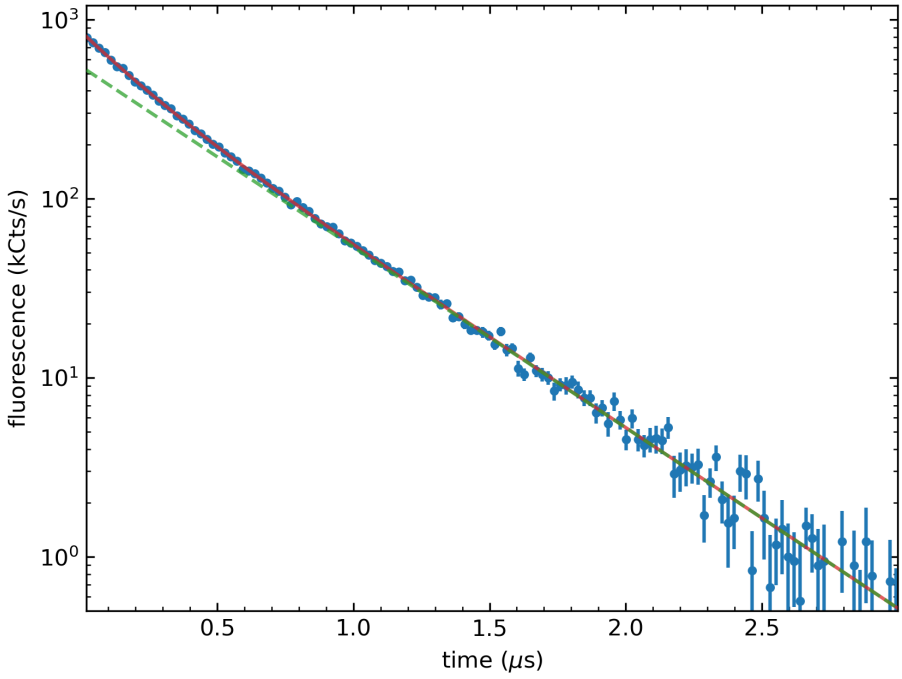


Figure 3.22: Lifetimes of the $A'^2\Delta_{3/2}$ state decay from molecules excited to the $B$ state. The observed fluorescence time profile for BaF molecules excited to the $B^2\Sigma_{1/2}(v=0)$ state that decay from the $A'^2\Delta_{3/2}$ state with fluorescence in a range from 1075 to 1100 nm. The solid line a fit to the sum of two exponential functions which determines the time constants $\tau_{\text{short}}$ and $\tau_{\text{long}}$, with the fluorescence from each exponential contributing approximately equally to the overall fluorescence. The dashed line represents the exponential function corresponding to $\tau_{\text{long}}$. Note that the $y$-axis has a logarithmic scale.

| Excited State | Fluorescence range (nm) | $\tau_{\text{short}}$ (ns) | $\tau_{\text{long}}$ (ns) |
|---|---|---|---|
| $B^2\Sigma_{1/2}(v=0)$ | 1075 – 1100 nm | 196(13) | 431(10) |
| $A^2\Pi_{1/2}(v=0)$ | 1075 – 1100 nm | 216(22) | 430(24) |
| $A^2\Pi_{1/2}(v=0)$ | 1050 – 1075 nm | 139(16) | 391(31) |
| $A^2\Pi_{1/2}(v=0)$ | 1025 – 1050 nm | 64(2) | 349(20) |

Table 3.5: Summary of the lifetimes observed for the $A'\Delta_{3/2}$ for BaF molecules within the neon matrix. The fluorescence corresponds to specific regions within the broader observed features of Figures 3.7 and 3.15.

cence feature. Assuming such a continuum of lifetimes, each 25-nm band of fluorescence would have a more limited range of lifetimes and these fit well to the sum of a short- and long-lived exponential. These two time constants increase as the observed wavelength of fluorescence becomes longer. By examining the fluorescence in finer segments the observation of a nearly smooth transition from short to long lifetimes is expected.

The observed lifetimes of the $A'^2\Delta_{3/2}$ state are found to be in good agreement for BaF molecules excited to the $A^2\Pi_{1/2}(v = 0)$ and $B^2\Sigma_{1/2}(v = 0)$ states indicating that the non-radiative decay from these states to the $A'\Delta_{3/2}$ state occurs on time scales much faster than the radiative lifetimes.

### 3.3.6 *Lifetime dependence on solid temperatures and activation energies*

To test for non-radiative decays to the ground $X^2\Sigma_{1/2}$ state, the lifetime of the laser-induced fluorescence is observed as a function of the temperature of the neon solid for several excitation and decay paths. This test is performed by

repeating the experiments of Section 3.3.3, Section 3.3.4, and Section 3.3.5, at several temperatures of the neon matrix. Temperature control of the matrix is achieved using a single cartridge heater placed on the inner layer of the cryogenic apparatus in conjunction with a proportional-integral-derivative loop using the substrate block temperature sensor (labelled *(f)* in Figure 2.5) to stabilize the temperature.

Assuming a non-radiative decay component of the lifetime is present within the matrix, the radiative decay rate $R_r$ as a function of temperature is expected to follow an Arrhenius rate equation [86]

$$R_r = \tau_r^{-1} + R_{nr} e^{-\frac{E_a}{k_B T}}, \tag{3.4}$$

where $\tau_r$ is the radiative lifetime within the matrix, $R_{nr}$ is the non-radiative decay rate, $E_a$ is the activation energy for the non-radiative decay path within the matrix, and $T$ is the temperature of the matrix.

Figure 3.23 shows two sets of data examining the lifetime of the two main decay paths for the excited $B^2\Sigma_{1/2}(v = 0)$ state of BaF in neon as a function of the temperature of the matrix.

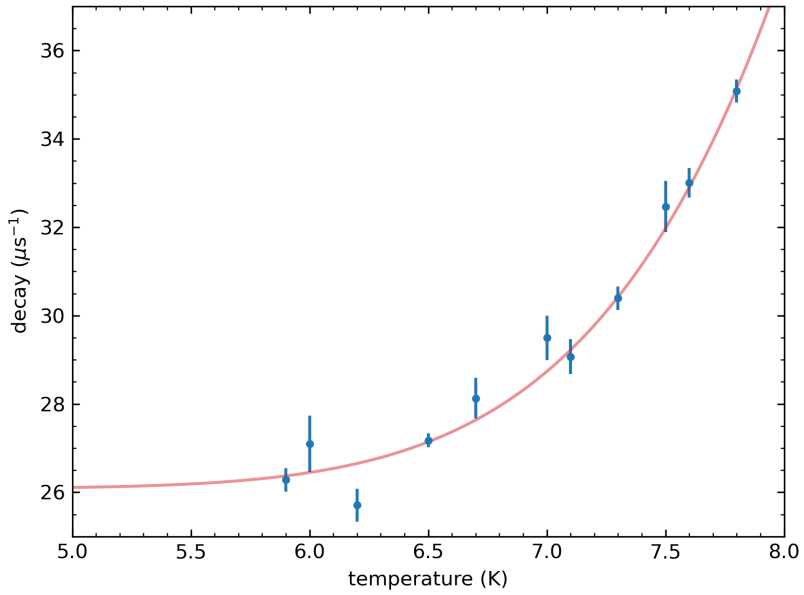


(a) $B^2\Sigma_{1/2}(v=0) \rightarrow X^2\Sigma_{1/2}(v=1)$

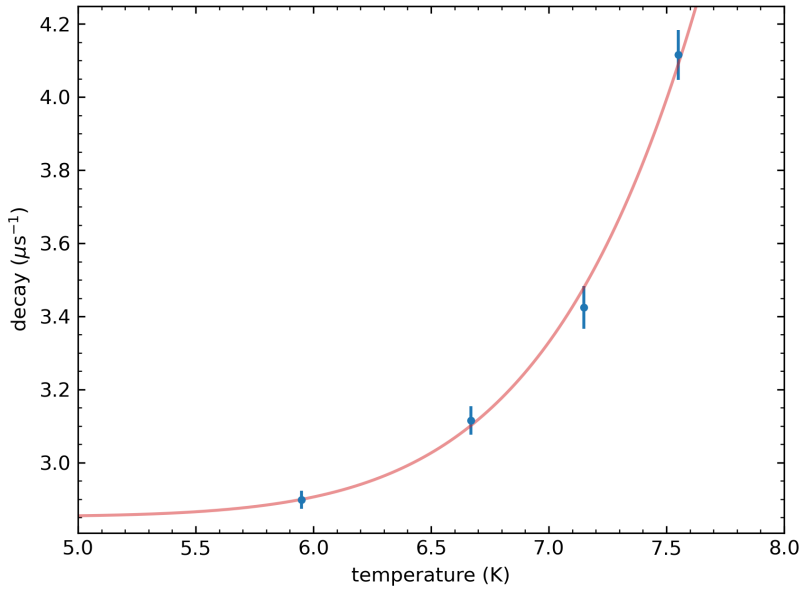


(b) $B^2\Sigma_{1/2}(v=0) \rightarrow A'^2\Delta_{3/2} \rightarrow X^2\Sigma_{1/2}$

Figure 3.23: Decay rate versus temperature for molecules excited to the $B$ state. Panel (a) shows the decay rate of the $B^2\Sigma_{1/2}(v=0)$-to-$X^2\Sigma_{1/2}(v=1)$ decay. Panel (b) shows the decay rate of the $A'^2\Delta_{3/2}$-to-$X^2\Sigma_{1/2}(v=0)$ decay. The solid lines are a fit to Equation 3.4.

For these experiments the excitation laser is tuned to 708 nm with a beam diameter of 40 $\mu$m and laser power of 400 mW. The rate of decay for the $B^2\Sigma_{1/2}(v=0)$ direct decay to the $X^2\Sigma_{1/2}(v=1)$ electronic ground state as a function of temperature is shown in Figure 3.23a using fluorescence light from 725 to 750 nm (see Figure 3.14). Figure 3.23b shows the decay rate for the decay of the $A'^2\Delta_{3/2}$ state for BaF molecules that are initially excited into the $B^2\Sigma_{1/2}(v=0)$ excited state using fluorescence light from 1075 to 1100 nm (see Figure 3.15). The solid lines in the figures represent a fit to Equation 3.4 from which the activation energy and non-radiative decay rate are extracted.

Figure 3.24 shows the lifetime of two decay paths for BaF molecules excited to the $A^2\Pi_{1/2}(v=0)$ state using 859-nm laser light as a function of the temperature of the neon matrix. Figure 3.24a uses the band of fluorescence from 950 to 970 nm, which corresponds to the decay from the $A'^2\Delta_{5/2}$ state (see Figure 3.7), while Figure 3.24b uses the band fluorescence from 1050 to 1100 nm, corresponding to the decay from the $A'^2\Delta_{3/2}$ state (see Figure 3.7). The time profiles of the fluorescence are fit to single exponential functions to ob-

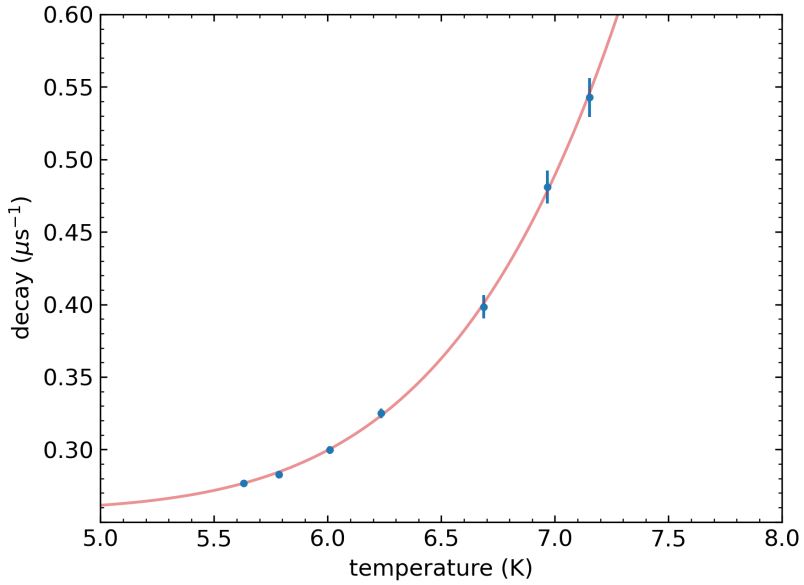


(a) $A^2\Pi_{1/2}(v=0) \rightarrow A'^2\Delta_{5/2} \rightarrow X^2\Sigma_{1/2}$

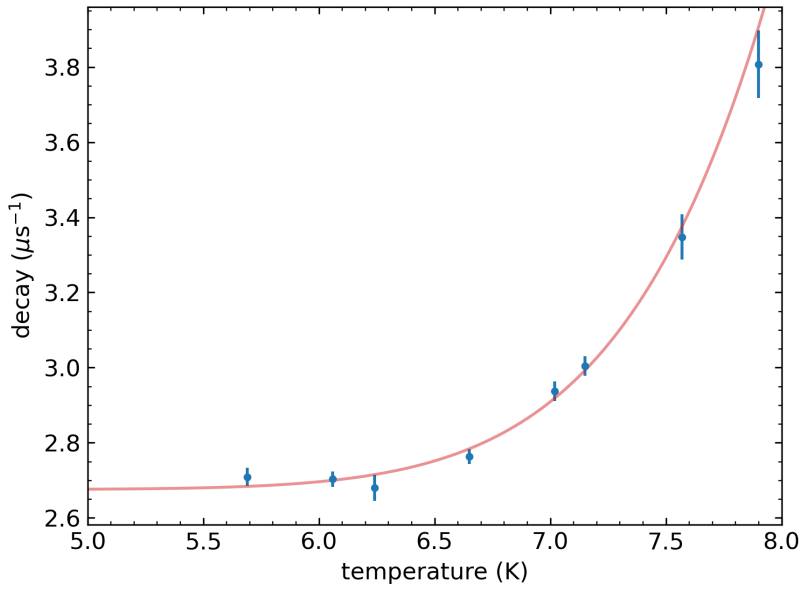


(b) $A^2\Pi_{1/2}(v=0) \rightarrow A'^2\Delta_{3/2} \rightarrow X^2\Sigma_{1/2}$

Figure 3.24: Decay rate versus temperature for molecules excited to the $A^2\Pi_{1/2}(v=0)$ state. Panel (a) shows the decay rate of the $A'^2\Delta_{5/2}$-to-$X^2\Sigma_{1/2}(v=0)$ decay. Panel (b) shows the decay rate of the $A'^2\Delta_{3/2}$-to-$X^2\Sigma_{1/2}(v=0)$ decay. The solid lines are a fit to Equation 3.4.

tain the data points shown in Figures 3.23 and 3.24. The solid lines in the figures are fit to Equation 3.4, with the relevant fit parameters reported in Table 3.6.

Equation 3.4 describes the data well, with different activation energies for each of the corresponding excitation and decay paths. Table 3.6 summarizes the activation energy obtained from each data set and decay path studied. Note that the non-radiative decay rate is reported as the value of the quantity $R_{nr}e^{\frac{E_a}{(k_B T)}}$ at a temperature of $T = 6$ K to emphasize the small contributions that the non-radiative process makes to the overall decay rate observed at the base temperature of the apparatus. This quantity is largest for the $A^2\Pi_{1/2}(v = 0) \rightarrow A'^2\Delta_{5/2} \rightarrow X^2\Sigma_{1/2}$ decay path, for which the non-radiative decay rate at 6 K implies that approximately 14% of $A'^2\Delta_{5/2}$ molecules decay non-radiatively. For the remaining excitation and decay paths studied, this relative proportion of molecules decaying non-radiatively is less than 2% at 6 K.

| Decay Path | $E_a$ ($cm^{-1}$) | $R_{nr} \cdot e^{\frac{E_a}{k_B\ 6K}}$ ($\mu s^{-1}$) | $\tau_r^{-1}$ ($\mu s^{-1}$) |
|---|---|---|---|
| $A^2\Pi_{1/2}(v=0) \rightarrow A'^2\Delta_{5/2} \rightarrow X^2\Sigma_{1/2}$ | 50(2) | 0.042(2) | 0.25(2) |
| $A^2\Pi_{1/2}(v=0) \rightarrow\ A'^2\Delta_{3/2} \rightarrow X^2\Sigma_{1/2}$ | 71(7) | 0.020(6) | 2.676(2) |
| $B^2\Sigma_{1/2}(v=0) \rightarrow\ X^2\Sigma_{1/2}(v=1)$ | 58(4) | 0.4(1) | 26.088(1) |
| $B^2\Sigma_{1/2}(v=0) \rightarrow A'^2\Delta_{3/2} \rightarrow X^2\Sigma_{1/2}$ | 64(8) | 0.05(2) | 2.852(3) |

Table 3.6: Summary of activation energies and non-radiative rates. The parameters presented are from a fit of the data to Equation 3.4. The non-radiative decay rate is reported as $R_{nr}e^{\frac{E_a}{(k_B(6\ K))}}$ to emphasize the small contributions that that non-radiative process makes to the overall decay rate observed at the 6-K base temperature of the apparatus.

## 3.4 CONCENTRATION OF BAF CONFINED WITHIN THE MATRIX

### 3.4.1 *Fluorescence from B-state excitation versus laser power*

For molecules excited to the $B^2\Sigma_{1/2}(v = 0)$ state and decaying directly to the $X^2\Sigma_{1/2}(v = 1)$ state, a nearly proportional increase in fluorescence is observed versus laser intensity, up to the maximum available intensity of 80 kW/cm$^2$, indicating that for BaF molecules confined to a neon matrix, it is difficult to saturate this transition.

Figure 3.25 shows the observed fluorescence (spanning from 725 to 750 nm) due to excitation with 708-nm laser light as a function of the intensity of this light. In Section 3.4.2 a method is formulated which uses both excitation rate of molecules and the previously determined lifetime of the direct decay to determine the number of BaF molecules implanted within the solid.

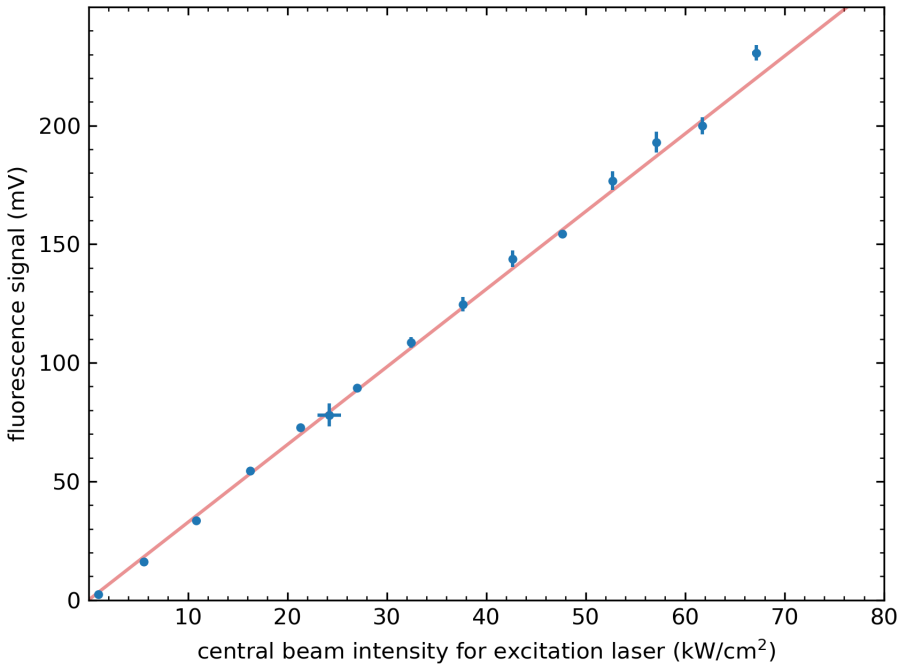


Figure 3.25: Laser-induced fluorescence versus power for excitation to the $B^2\Sigma_{1/2}(v = 0)$ state. The observed laser-induced fluorescence spans from 725 to 750 nm. The laser spot diameter is 40 $\mu$m with a maximum output power of nearly 500 mW. The data fits well to a straight line indicating that the transition is not near saturation.

### 3.4.2 *Rate equations and determination of BaF concentration*

Assuming that laser excitation to the $B^2\Sigma_{1/2}(v = 0)$ state (with decay directly back to the $X^2\Sigma_{1/2}$ state) is a closed system, the excitation is described by a rate equation:

$$\frac{db}{dt} = r(1 - b) - b/\tau_b. \tag{3.5}$$

Here, $b$ is the population in the excited state, $(1 - b)$ is the population in the ground state, and $r$ is the rate at which the ground-state population is excited. Equation 3.5, along with the constraint that $b = 0$ at $t = 0$ (when the laser is off), yields a solution

$$b(t) = \frac{r(\tau_b - e^{\frac{-t}{\tau_b}} e^{-tr}\tau_b)}{1 + r\tau_b}. \tag{3.6}$$

However, the rate of excitation is dependent on the distance from the centre of the laser beam. For a gaussian laser beam, this dependence is expressed as $r(s) = Re^{-\frac{s^2}{2\sigma^2}}$. Equation 3.6 can be integrated over the profile of the gaussian beam to obtain a solution proportional to the area of the laser beam:

$$b(t) = 2\pi \int_0^\infty \frac{r(s)\tau_b(1 - e^{\frac{-t}{\tau_b}} e^{-tr(s)})}{1 + r(s)\tau_b} sds. \tag{3.7}$$

The solution to Equation 3.7 can be written in terms of the exponential integral function:

$$b(t) = (2\pi\sigma^2)(R\tau_b + (Ei(\frac{-t}{\tau_b}) - Ei(-t(R + \tau_b^{-1}))). \quad (3.8)$$

For small excitation rate $R$, this solution can be simplified using Taylor series expansions:

$$\begin{aligned}
b(t) &= 2\pi \int_0^\infty \frac{r(s)\tau_b s ds}{1 + r(s)\tau_b} - 2\pi \int_0^\infty \frac{r(s)\tau_b e^{-t(r+\tau_b^{-1})} s ds}{1 + r(s)\tau_b} \\
&= -2\pi\sigma^2 \int_R^0 \frac{\tau_b dr}{1 + r\tau_b} + 2\pi\sigma^2 \int_R^0 \frac{\tau_b e^{-t(r+\tau_b^{-1})} dr}{1 + r\tau_b} \\
&= 2\pi\sigma^2 ln(1 + R\tau_b) \\
&\quad + \pi\sigma^2\tau_b \int_R^0 \frac{(2e^{-t/\tau_b} - 2tre^{-t/\tau_b} + t^2r^2e^{-t/\tau_b})}{1 + r\tau_b} dr + \mathcal{O}(R^3) \\
&\approx 2\pi\sigma^2 ln(1 + R\tau_b) \\
&\quad + \pi\sigma^2\tau_b e^{-t/\tau_b} \int_R^0 (2 - 2tr + t^2r^2)(1 - r\tau_b) dr + \mathcal{O}(R^3) \\
&= 2\pi\sigma^2 ln(1 + R\tau_b) \\
&\quad + 2\pi\sigma^2\tau_b e^{-t/\tau_b} \int_R^0 (2 - 2r(t + \tau_b) + r^2(t^2 + 2t\tau_b)) dr) \\
&\quad + \mathcal{O}(R^3).
\end{aligned} \quad (3.9)$$

Using the simplified expression, the definite integral is easily performed and all constants are absorbed into a single term $D$ to express the approximate solution to Equation 3.5 as

$$b(t) = D - 2\pi\sigma^2\tau_b R e^{-t/\tau_b} + \pi\sigma^2\tau_b R^2(t+\tau_b)e^{-t/\tau_b} + \mathcal{O}(R^3). \tag{3.10}$$

Defining $d(t) = b(t)/\tau_b$ yields an expression for the radiative decay rate from the $B^2\Sigma_{1/2}$ state that is proportional to the area of the laser beam:

$$d(t) = d_{ss} - 2\pi\sigma^2 R e^{-t/\tau_b} + \pi\sigma^2 R^2(t+\tau_b)e^{-t/\tau_b}) + \mathcal{O}(R^3). \tag{3.11}$$

Here, $d_{ss}$ is the steady-state value of $d(t)$, which, when neglecting the higher-order terms of $R$, becomes

$$d_{ss} = \pi\sigma^2[2R - R^2\tau_b]. \tag{3.12}$$

The ratio of the $d(t)/d_{ss}$ evaluated at a specific laser intensity (with the rate at this specified intensity denoted as $R_0$) is

$$\begin{aligned}\frac{d(t)}{d_{ss}}\Big|_{R_0} &= 1 - (\frac{2 - R_0(t+\tau_b)}{(2 - R_0\tau_b)})e^{-t/\tau_b} \\ &\approx 1 - (1 - \frac{R_0(t+\tau_b)}{2})(1 + \frac{R_0\tau_b}{2})e^{-t/\tau_b} \\ &= 1 + (\frac{R_0 t}{2} + \frac{R_0^2\tau_b(t+\tau_b)}{4} - 1)e^{-t/\tau_b}.\end{aligned} \tag{3.13}$$

If, in a second experiment, the laser power is reduced by a factor $\eta$, the difference of the ratio for the two experiments is given by

$$\frac{d(t)}{d_{ss}}\Big|_{R_0} - \frac{d(t)}{d_{ss}}\Big|_{\eta R_0} \approx \ (\frac{R_0 t}{2}(1-\eta))e^{-t/\tau_b}. \tag{3.14}$$

Figure 3.26 shows this difference for an experiment using a laser power of $P_0 = 387$ mW and a second experiment performed with $\eta P_0$, where $\eta = 0.52$. The observed difference agrees with Equation 3.14 (where $R_0$ is the only free parameter). The line of best fit provides a value of $R$ of $0.026(3)$ $\mu s^{-1}$ per kW/cm$^2$.

It should be noted, however, that this estimate for $R$ is an upper limit, as the intense excitation laser could cause warming of the matrix, either globally or locally near the site of

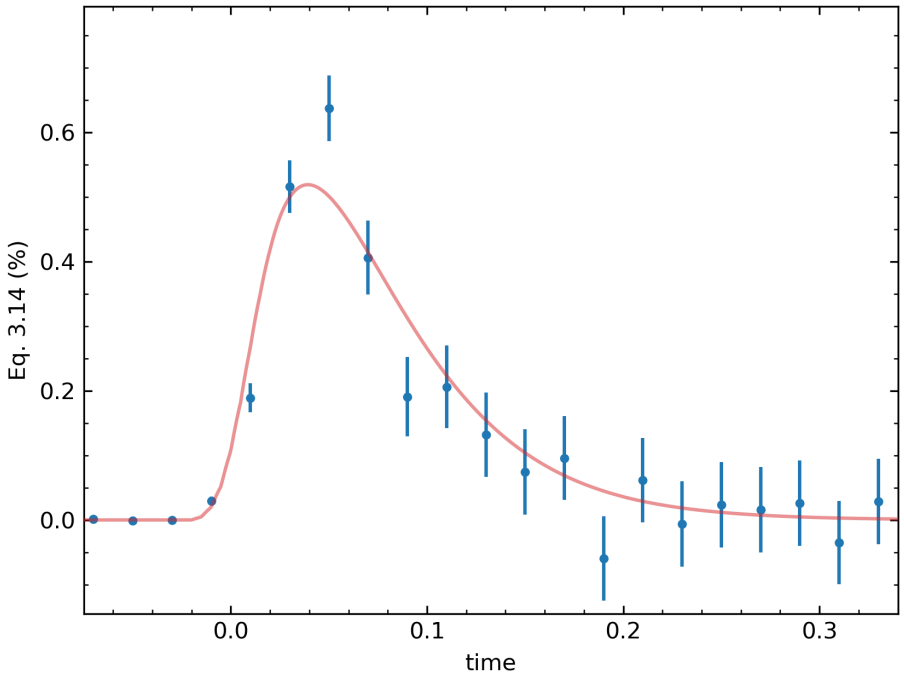


Figure 3.26: The time profile of the normalized difference of fluorescence at $P_0$ and $\eta P_0$. The fit shown is a one-parameter fit of the form of Equation 3.14, with the value of $R_0$ being the only free parameter. The graph reveals the excess fluorescence that occurs before population builds up in the $B^2\Sigma_{1/2}$ state. Note that time $t = 0$ denotes the moment that the excitation laser is turned on and the solid begins fluorescing. The fit includes a convolution with the 25-ns turn-on time for the laser.

the interacting BaF molecule, which would cause a decrease in fluorescence due the non-radiative decay's relation to temperature (see Section 3.3.6, with Figure 3.23, Figure 3.24, and Table 3.6).

The collection efficiency of the total fluorescence emitted from the BaF molecules is calculated by considering the solid angle subtended by the 2-inch-diameter in-vacuum collection lens (from the excitation laser spot, see Figure 2.1) combined with the total expected transmission and reflection efficiency of every optic along the path from the BaF molecules within the neon matrix to the photodetector (this path is shown pictorially in Figure 2.2). Approximately 1% of the emitted fluorescence light is effectively coupled into the detection systems. The quantum efficiency of the InGaAs detector is determined by sending 732-nm laser light, with a measured total power, into the detector and observing the response. The responsivity of the InGaAs detector is determined to be 0.074 $A/W$, implying a quantum efficiency of 12.5% at 732 nm.

Laser excitation of the $B^2\Sigma_{1/2}(v=0)$ state with a 400-mW laser and a beam diameter of 40 $\mu$m, generates a voltage of 0.2 V (see Figure 3.25) across the InGaAs photodetector. This detector has a gain of $10^9$ V/A. The signal of the photodetector corresponds to $1.3 \times 10^9$ electrons per second. Using this electron rate, the quantum efficiency, and the collection optics efficiency the rate of photons emitted by the fluorescing BaF molecules is calculated to be $1.6 \times 10^{12}$ photons per second. The photon emission rate accounts for only the molecules decaying to the $X^2\Sigma_{1/2}(v=1)$ state and the total photon emission rate for molecules undergoing the $B^2\Sigma_{1/2}(v=0)$-to-$X^2\Sigma_{1/2}$ decay is calculated by dividing the emission rate by the $v=1$ branching ratio of the free molecule (18% [51]). Finally, this result is divided by the experimentally determined excitation rate obtained from the fit in Figure 3.26 to determine that $8 \times 10^9$ molecules per mm$^2$ participate in the decay cycle within the sample.

A similar calculation is performed for the molecules that decay through the $A'\Delta_{3/2}$. However, a measurement using the decay through the $A'\Delta_{3/2}$ is less accurate owing to the broader fluorescence feature that contains a range of lifetimes.

This calculation places the total number of molecules (laser excited to the $B^2\Sigma_{1/2}(v=0)$ state) which decay through the $A'\Delta_{3/2}$ state at $4 \times 10^{10}$ molecules per mm$^2$, with an uncertainty of approximately 50%.

The total amount of molecules, per unit area, confined and addressable within the bulk of the matrix is the sum from the two decay paths:

$$N_{\text{total}} = (5 \pm 3) \times 10^{10}/\text{mm}^2. \tag{3.15}$$

As discussed earlier in this section, this result is a lower limit. Given that laser heating may lead to undetected non-radiative decay.

## 3.5 OPTICAL PUMPING OF BAF IN NEON

### 3.5.1 *Single-pulse experiment*

Optical pumping is observed using a circularly-polarized excitation laser that is tuned to 859 nm to excite BaF molecules to the $A^2\Pi_{1/2}(v=0)$ state and impart angular momentum in the presence of a magnetic field that is parallel to the laser

propagation direction. A simplified diagram of this process is presented in Figure 3.27, in which the relevant sublevels and decay processes are shown. The dashed line represents non-radiative decay from the $A^2\Pi_{1/2}(v = 0)$ state to the $A'^2\Delta_{3/2}$ state. The molecules then radiatively decay to the $X^2\Sigma_{1/2}$ ground state and fluorescence from 1000 to 1100 nm is observed with the single-photon counter and time tagger (see Section 2.6.4) to examine the time profile of the fluorescence. The signature of optical pumping is shown in Figure 3.28, where the laser is turned on at time $t = 0$ (using an AOM) in the presence of a 15-G magnetic field and the fluorescence, after rising to a maximum value, starts to decrease while the excitation laser remains on. The molecules cycle through the excitation process depicted in Figure 3.27, until they reach the $m_f = 1$ sublevel of the ground-state hyperfine structure and can no longer be excited to the $A^2\Pi_{1/2}(v = 0)$ state.

Only the molecules that are parallel (or anti-parallel) to the magnetic field are efficiently optically pumped. A discussion of the behaviour of molecules oriented in other directions is outside of the scope of this work. However, in Ref. [87] optical pumping is modelled by collaborators, for all orientations of

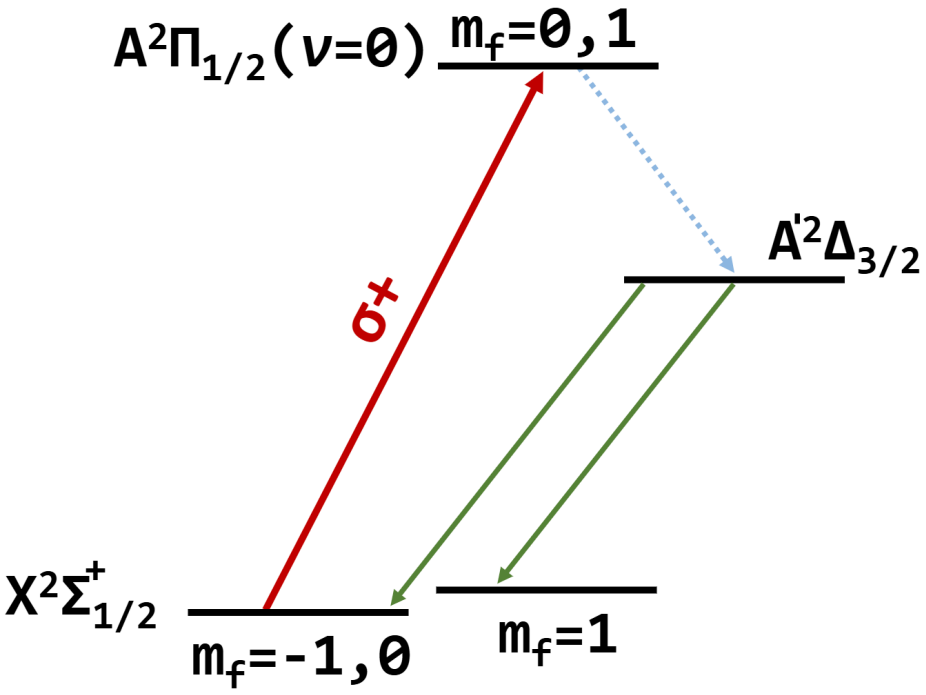


Figure 3.27: Optical pumping energy-level diagram. A simplified energy-level diagram (not to scale) of the optical-pumping process observed when exciting BaF molecules to the $A^2\Pi_{1/2}(v=0)$ and observing the fluorescence from the $A'^2\Delta_{3/2}$ state. Note that the process pictured only applies for molecules which are aligned parallel or antiparallel to the laser propagation direction.

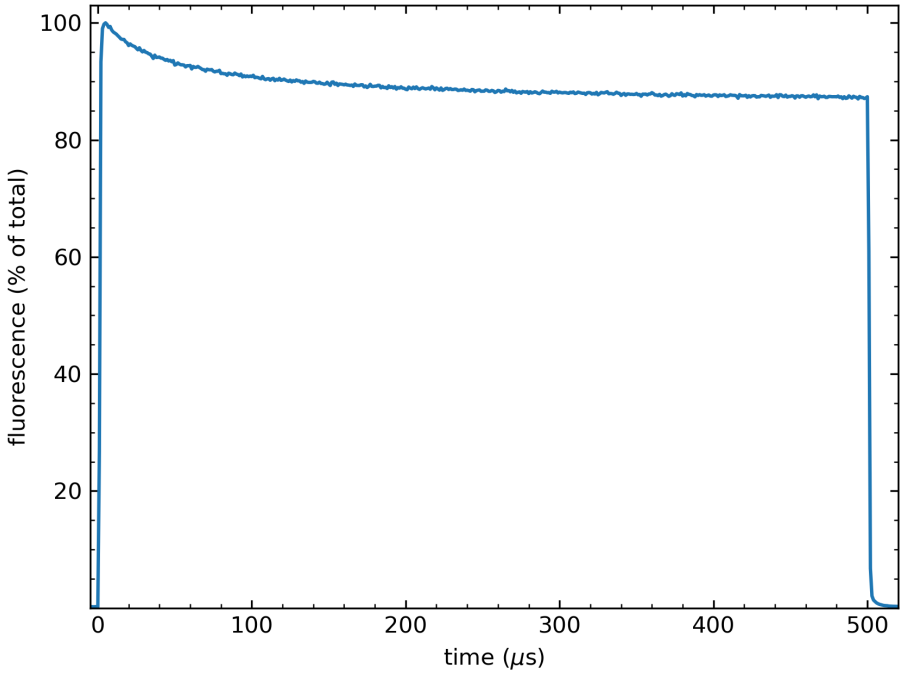


Figure 3.28: Observed signal for optical pumping. The fluorescence emitted from the solid, from 1000 to 1100 nm is shown as a function of time. The laser is turned on at time $t = 0$ and kept on until $t = 500$ $\mu$s.

BaF and these calculations show qualitative agreement with the results of Figure 3.28.

### 3.5.2 *Optical pumping with multiple laser pulses*

To demonstrate that the reduction in fluorescence versus time observed in Figure 3.28 is due to optical pumping, an experiment is performed using pulses from two laser beams. For this experiment, the excitation laser is split into the optical paths shown in Figure 3.29. Two laser beams are created as shown in the bottom part of Figure 3.29, with one beam being P-polarized and the other being S-polarized. Each beam is generated from the first-order diffraction of a dedicated AOM, which are used to pulse the beams. These two beams are coupled into polarization-maintaining fibres which transmit the light from the optics table to an optical breadboard attached to the outside of the vacuum chamber. The beams are overlapped with a polarizing beamsplitter cube on the optical breadboard. A beam sampler picks off a small portion (approximately 5%) of the laser power before passing the beams through a beam-expanding telescope and focusing lens, creating a beam spot size of 45 $\mu$m at the location of the

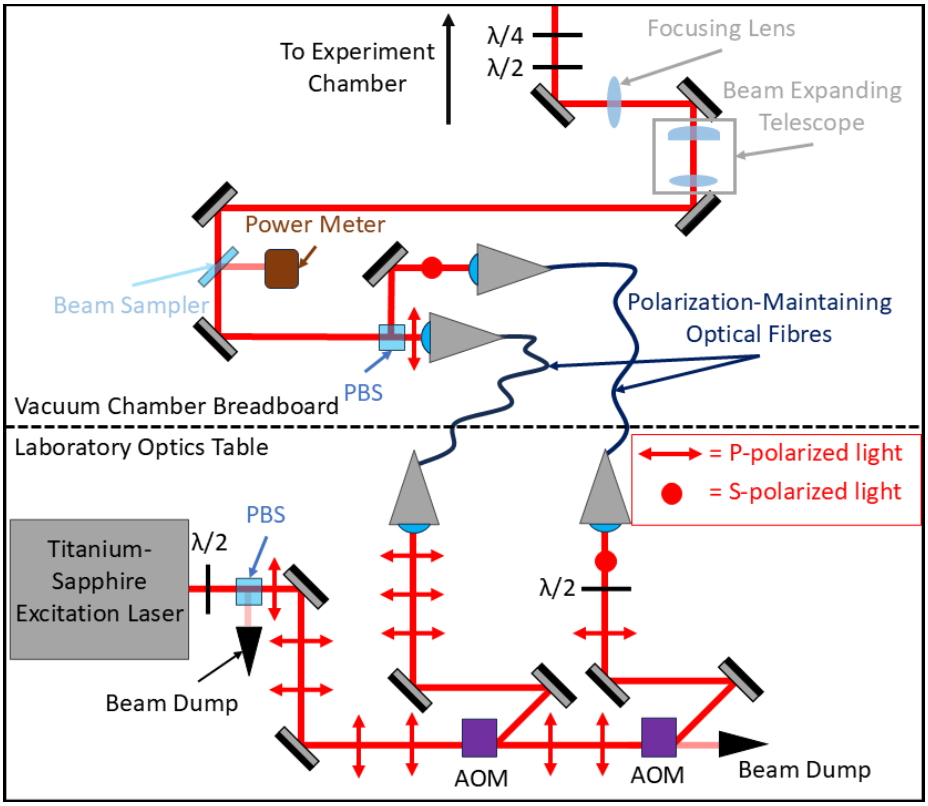


Figure 3.29: Diagram of the overlapping beams optical-pumping experiment. The dashed line represents a physical break in the laboratory across which the optical fibres transmit the laser light.

substrate. A quarter-waveplate creates $\sigma_+$- and $\sigma_-$-polarized light from the two input polarizations.

These AOMs are used to rapidly alternate between the two circular polarizations used for optical pumping. Switching from $\sigma_+$-polarized to $\sigma_-$-polarized excitation laser light (or equivalently $\sigma_-$-polarized to $\sigma_+$-polarized) allows BaF molecules which have been optically pumped into a dark state to become accessible once again to the interacting laser light.

The result from such a pulsed experiment is shown in Figure 3.30, where the fluorescence from each polarization is normalized to laser power. The experiment consists of a repeating train of 495-$\mu$s-long pulses of laser light separated by 5-$\mu$s gaps. The polarization of the four pulses used in this sequence is: $\sigma_+$, $\sigma_+$, $\sigma_-$, $\sigma_-$. This sequence is repeated for several minutes in the presence of a 15-G magnetic field. The fluorescence shown in the figure represents the average over this time. For these pulses, the excitation laser is tuned to the $X^2\Sigma_{1/2} \rightarrow A^2\Pi_{1/2}(v = 0)$ transition with a wavelength of 859 nm, beam diameter of 45 $\mu$m, and laser power of 200 mW.

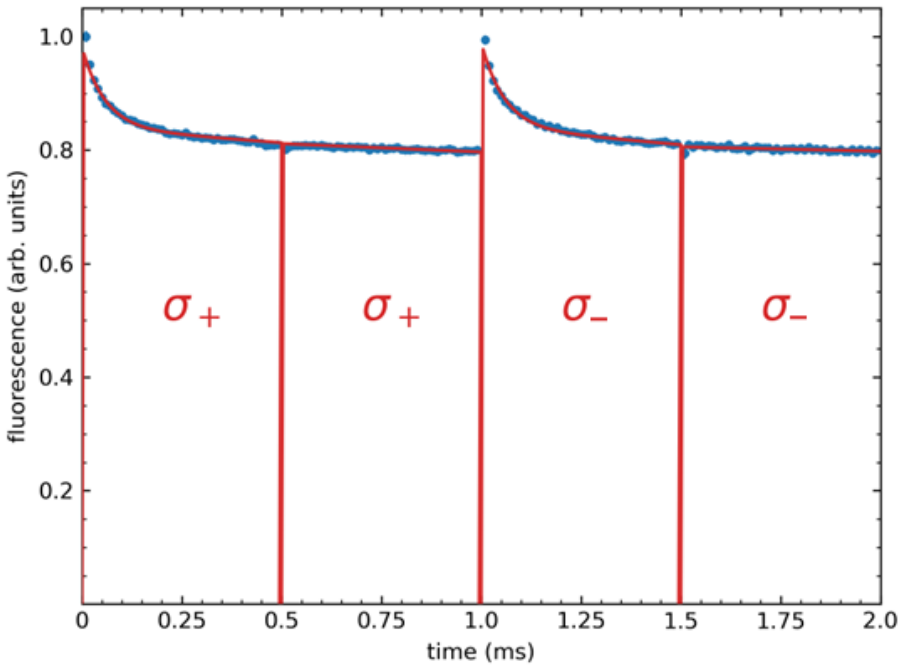


Figure 3.30: Optical pumping from pulses of laser light with differing polarization. A repeating train of 495-$\mu$s-long pulses are separated by 5-$\mu$s gaps in the presence of a 15-G magnetic field. The pulses have polarizations of $\sigma_+, \sigma_+, \sigma_-, \sigma_-$ and excite the $A^2\Pi_{1/2}(v = 0)$ transition. The graph shows the average fluorescence (averaged over several minutes) during four pulses. The fluorescence for each polarization is normalized to laser power. The solid lines are fits to Equation 3.16.

The first and third pulses cause optical-pumping (similar to that depicted in Figure 3.27). Since for these two pulses the polarization is switched (for the first pulse from $\sigma_-$ to $\sigma_+$ and for the third pulse from $\sigma_+$ to $\sigma_-$). No optical pumping is seen when subsequent pulses are of the same polarization.

The reduction in fluorescence caused by optical pumping for each pulse in Figure 3.30 is fit to a single exponential, with an added linear component to capture the longer-term behaviour:

$$f(t) = P_1 e^{-t/\tau_{op}} + mt + P_2. \tag{3.16}$$

Here, $P_1$ corresponds to the population sensitive to the faster optical-pumping effect, $P_2$ corresponds to the remaining population participating in the fluorescence, while $\tau_{op}$ and $1/m$ are the time constants associated with the faster and longer-term effects, respectively. The lifetime associated with the faster component of the optical pumping signature is found to be approximately 30 $\mu$s, which is an indication of the time it takes for BaF molecules to optically pump into the dark $X^2\Sigma_{1/2}(F = 1, m_f = \pm 1)$ state (the $\pm$ is dependent on whether the molecules see $\sigma_+$- or $\sigma_-$-polarized light). The

longer-term behaviour, described by $1/m$, is not yet well understood but is an indication that the optical-pumping model considered is incomplete in describing the mechanisms at work.

### 3.5.3 *Population shelving in the hyperfine structure*

The time constant for the molecular population to remain in the $X^2\Sigma_{1/2}(F = 1, m_f = +1)$ dark state is determined by performing an experiment with two pulses of light (both of $\sigma_+$-polarization) with a varying time gap between them. The excitation laser is setup similarly to Figure 3.29, with only a single circular polarization of $\sigma_+$ and with the pulsing of the laser light performed by a single AOM. The amount of optical pumping due to the second pulse is determined by fitting the fluorescence during the second pulse to Equation 3.16 and examining the ratio

$$\frac{P_1}{P_1 + P_2}. \tag{3.17}$$

Equation 3.17 is the ratio of the fluorescence reduction due to the faster component of decay ($P_1$) to the total fluorescence at the start of the second pulse ($P_1 + P_2$). Figure 3.31 shows the

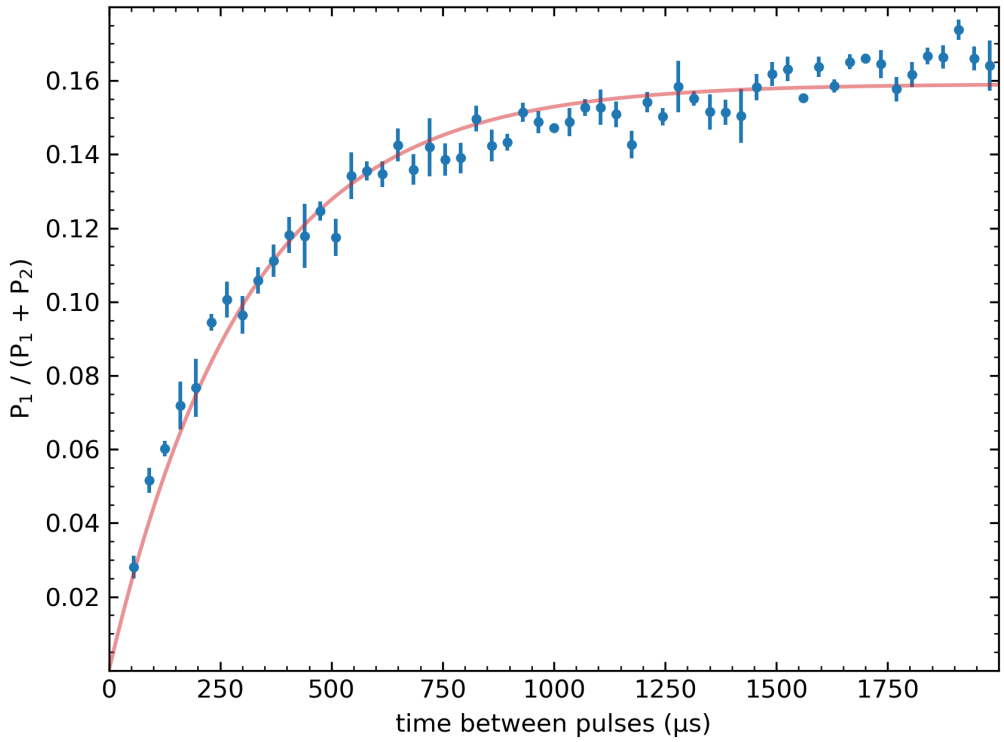


Figure 3.31: Optical pumping as a function of pulse separation. Two pulses of $\sigma_+$-polarized light are separated by time intervals spanning from 20 $\mu$s to 2 ms. The $y$-axis is $P_1/(P_1 + P_2)$ obtained from a fit of the fluorescence during the second of a pair of laser pulses (see Equation 3.17) and is a measure of how much optical pumping occurs due to the second pulse. The solid line is a fit to Equation 3.18, which yields $\tau_{\text{dark}} = 310(10)$ $\mu$s.

result of this experiment versus time gaps between the two $\sigma_+$ pulses. Note that for zero gap the ratio is zero, as the BaF is already optically pumped by the first $\sigma_+$ pulse. As the time gap increases the ratio increases (as the optically-pumped BaF population migrates from its dark state).

A two-parameter fit of the form

$$C(1 - e^{-t_{\text{gap}}/\tau_{\text{dark}}}) \tag{3.18}$$

is shown as a solid line in Figure 3.31 and gives a time constant of $\tau_{\text{dark}} = 310(10)$ $\mu$s. This time constant may be limited by the presence of stray magnetic fields across the sample. The Earth's magnetic field is the largest external source of stray magnetic field, however the stray field due to magnetic impurities (e.g., $^{21}$Ne and $O_2$) are likely playing a role. The stray magnetic fields created by impurities could cause the electrons in the BaF molecules to precess, causing changes in the hyperfine populations. Further, it could be that matrix-assisted mechanisms make it possible to move populations from one hyperfine sublevel to another without the need of stray magnetic fields. The limiting factor in the observed associated lifetime $\tau_{\text{dark}}$ is not yet known, but will

be better understood when higher-purity matrices reduce the effect of impurities and lower temperatures reduce matrix-assisted effects.

## 3.6 RADIO-FREQUENCY RESONANCE OF THE HYPERFINE STRUCTURE

### 3.6.1 *Radio-frequency resonance*

The hyperfine structure of BaF molecules within the matrix is studied by driving radio-frequency (RF) transitions. For those studies BaF molecules are optically pumped with $\sigma_+$-polarized laser light which is tuned to excite the $X^2\Sigma_{1/2} \rightarrow A^2\Pi_{1/2}(v = 0)$ transition. The $\sigma_+$-polarized laser beam optically pumps the molecules into the $X^2\Sigma_{1/2}(F = 1, m_f = 1)$ state (see Figure 3.27). These BaF molecules are transferred to the $X^2\Sigma_{1/2}(F = 0, m_f = 0)$ sublevel of the hyperfine structure with a pulse of RF field produced by coils within the vacuum system (see Figure 2.9). Figure 3.32 shows an energy-level diagram with the transitions being driven. Because BaF molecules in the $X^2\Sigma_{1/2}(F = 0, m_f = 0)$ sublevel are able to interact with the excitation laser (i.e., are no longer in a

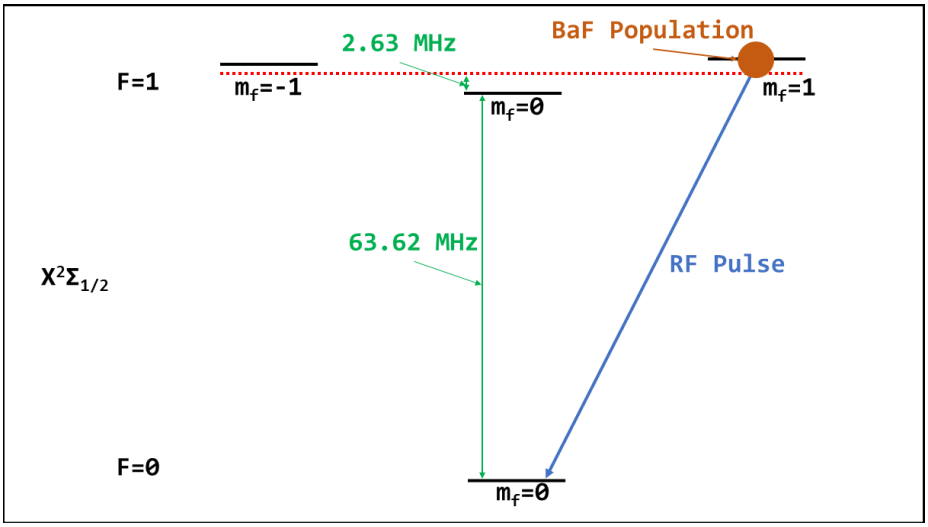


Figure 3.32: RF transition energy-level diagram. The BaF molecules are transferred from the $F = 1, m_f = 1$ sublevel (the dark state) of the ground state to the $F = 0, m_f = 0$ sublevel with an RF field. As a result, there is an increase in fluorescence, as depicted in Figure 3.33. The diagram is drawn to scale and the energy separation for a perfectly aligned [26] molecule is given by the green arrows. The dashed red line indicates the energy for the $F = 1$ hyperfine state for the free molecule. Note that the energy separation between the $m_f = 1$ and $m_f = -1$ sublevels is dependent on the magnetic field.

dark state), an increase in total fluorescence is observed after the molecules are subjected to an RF field tuned to this $X^2\Sigma_{1/2}(F=1, m_f=1) \rightarrow X^2\Sigma_{1/2}(F=0, m_f=0)$ hyperfine transition. This increased fluorescence is illustrated in Figure 3.33 (cf. Figure 3.34 , in which no RF transition is driven)

In Figure 3.33 two $\sigma_+$-polarized light pulses are shown. These pulses are used to excite the $A^2\Pi_{1/2}(v=0)$ transition and separated by a short time relative to the time constant of $\tau_{\text{dark}}$ (see Section 3.5.3), with a pulse of RF radiation inserted in the time between the pulses. Figure 3.34 shows the two light pulses in a similar experiment without the insertion of this RF pulse. Every 20 ms the two experiments are alternated and the excess fluorescence caused by the return of the optical pumping signature (when the RF pulse is present and on resonance) is measured. To increase sensitivity to the excess fluorescence caused by inserting the RF pulse, this effect is observed by using a highly-sensitive liquid-nitrogen-cooled InGaAs photodetector (see Section 2.6.3). This detector has high quantum efficiency but has a slow time constant of 3.3 ms. As a result it cannot see the time-resolved fluorescence depicted in Figures 3.33 and 3.34. However, it is sensitive to

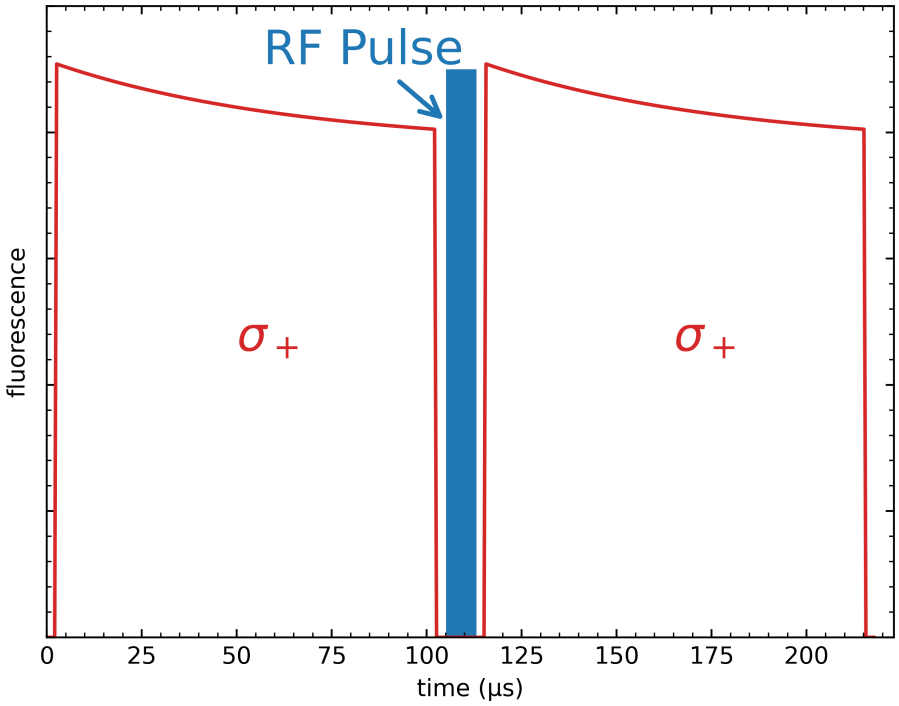


Figure 3.33: Radio-frequency resonance single-pulse experiment timing diagram. Two $\sigma_+$-polarized light pulses with a short, on-resonance RF pulse inserted between them. The RF pulse causes the optical-pumping signature to be present during the second pulse when on resonance with the $X^2\Sigma_{1/2}(F = 1, m_f = 1) \rightarrow X^2\Sigma_{1/2}(F = 0, m_f = 0)$ transition. This increase in fluorescence is in contrast to the experiment depicted in Figure 3.34 where no RF field is applied.

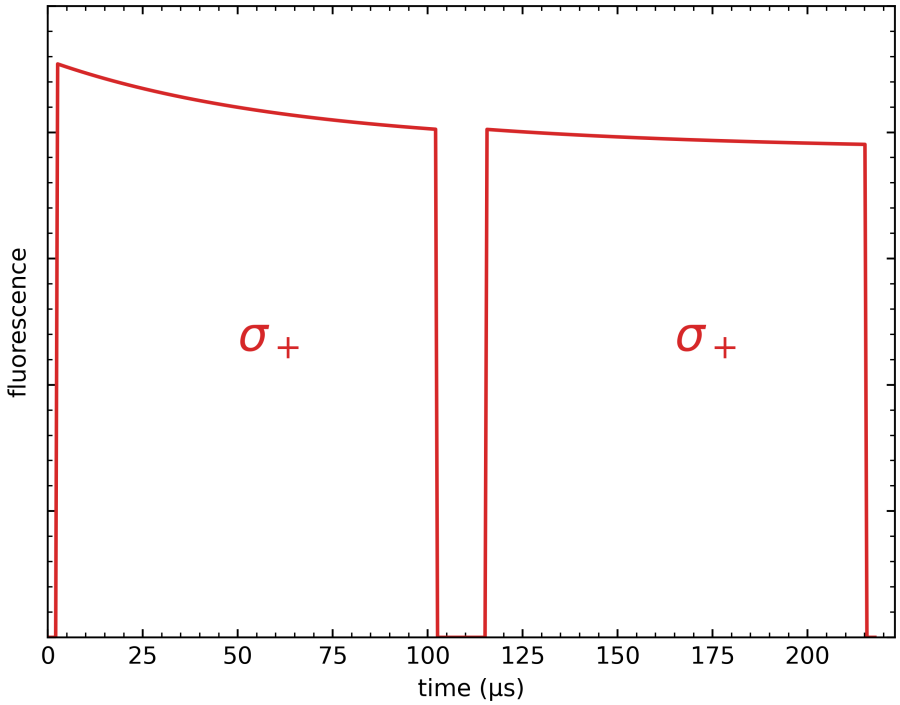


Figure 3.34: Timing diagram for the null experiment to complement the radio-frequency single-pulse experiment. This figures shows the timing for the complementary experiment to the one depicted in Figure 3.33, but with no RF field between the two pulses of laser light.

the average fluorescence and therefore capable of seeing the difference between the average fluorescence of Figures 3.33 and 3.34. The difference between this complementary pair of experiments is averaged over many 40-ms cycles.

Figure 3.35 shows the difference of fluorescence for the complementary experiments of Figures 3.33 and 3.34, with an applied magnetic field of 3 G, as a function of the RF frequency of the RF pulse. The pulses of $\sigma_+$-polarized light are 100 $\mu$s long with a 13-$\mu$s gap containing a 8-$\mu$s-long RF pulse with 36 dBm of power centred in time between the excitation-laser pulses. The laser light used in this is experiment is tuned to 859 nm, with a beam diameter of 45 $\mu$m at the location of the substrate and a power of 50 mW. This lower intensity of laser light is used to minimize local warming that could take place at the location of the laser spot and is found to provide a larger peak in the RF resonance response. As illustrated in Figures 3.33 and 3.34, an excess of fluorescence from the optical pumping signature is observed when the RF pulse is tuned to the $X^2\Sigma_{1/2}(F = 1, m_f = 1) \rightarrow X^2\Sigma_{1/2}(F = 0, m_f = 0)$ transition, resulting in the broad resonance centred at 69 MHz shown in Figure 3.35. The resonance feature is much broader

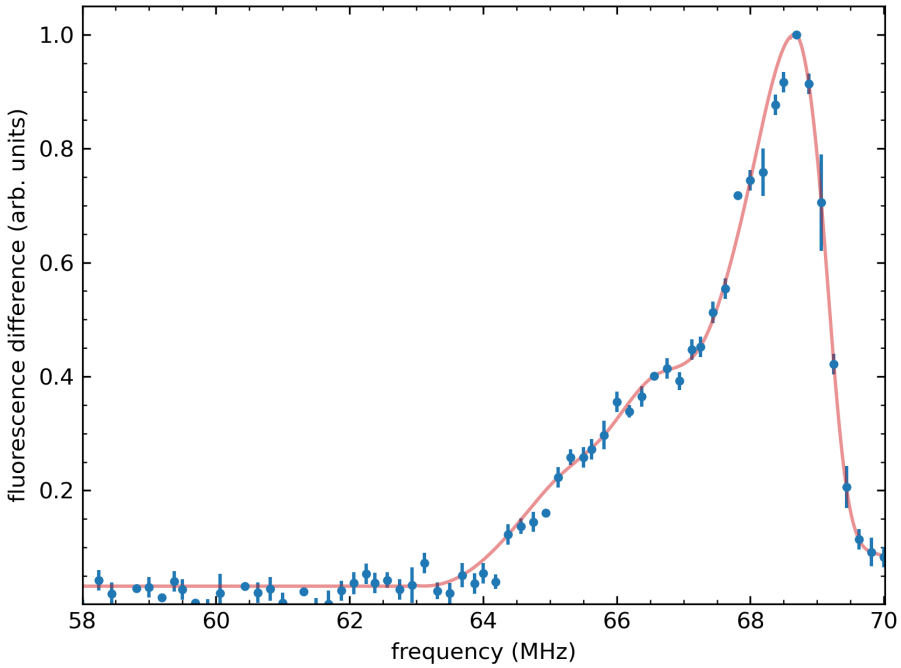


Figure 3.35: RF resonance of the hyperfine transition as a function of RF frequency. The difference in average fluorescence for the experiments depicted in Figures 3.33 and 3.34 versus RF field frequency. The solid line serves as a guide for the eye. The RF field transfers the molecular population from the dark $F = 1, m_f = 1$ state to the $F = 0, m_f = 0$ state, thus increasing the observed fluorescence. At an applied magnetic field of 3 G a clear resonance is seen with a peak at approximately 69 MHz.

than the 125-kHz limit for the 8-$\mu$s-long RF pulse used to drive the transition, likely indicating inhomogeneity in the magnetic field at the location of the BaF molecules within the sample. Such inhomogeneity could be caused by the presence of impurities with magnetic dipole moments. Molecular orientations within the sample (relative to the applied magnetic field) also leads to a broadened resonance width, but it is predicted [88] to be much smaller than the observed width.

### 3.6.2 *Dependence on magnetic field*

Figure 3.36 shows the centre of the observed RF resonance for the $F = 1, m_f = 1 \rightarrow F = 0, m_f = 0$ transition as a function of applied magnetic field. Each point in Figure 3.36 is obtained from a spectrum similar to Figure 3.35 and the centre of resonance for the observed transition is determined by applying a rolling average of 0.5 MHz to the observed spectrum, where the maximum value of the difference in fluorescence is taken to be the centre. The excitation laser setup and characteristics are the same as in Section 3.6.1.

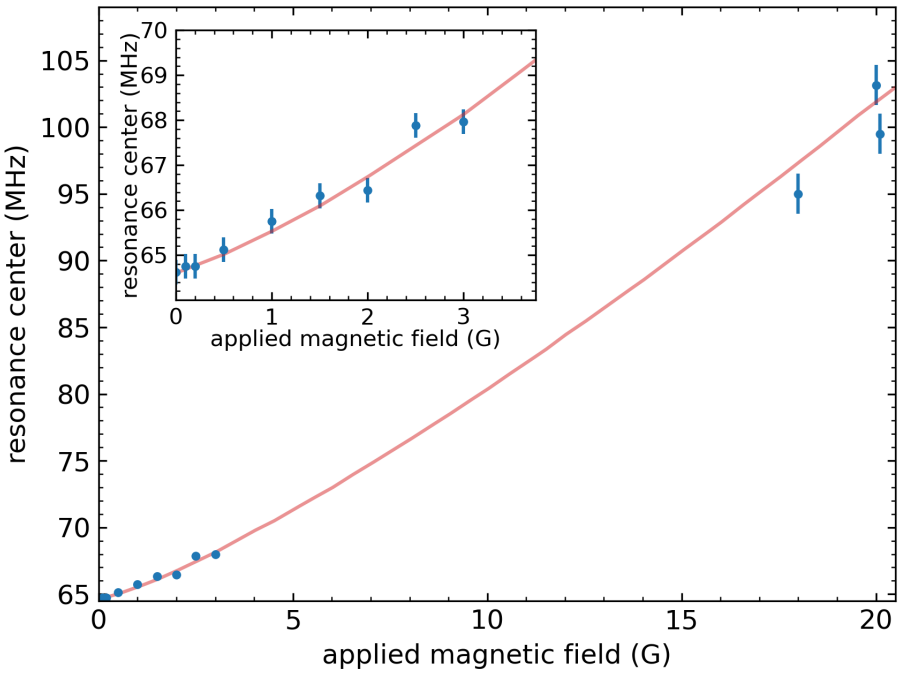


Figure 3.36: RF resonance centre as a function of applied magnetic field. Each point in the figure comes from a spectrum similar to that shown in Figure 3.35. The solid line represents the calculated energies of the observed hyperfine transition versus the applied magnetic field for an isotropic distribution of BaF molecule orientations. The inset shows an expanded view of the data for magnetic fields $< 3.5$ G.

The energies of the hyperfine states for a BaF molecule in its ground electronic $X^2\Sigma_{1/2}$ state can be obtained by diagonalizing the effective Hamiltonian

$$H = b\vec{I}\cdot\vec{S} + cI_kS_k - g\mu_B B_z S_z, \tag{3.19}$$

where $b$ and $c$ are hyperfine constants, $B$ is the applied magnetic field, $S$ is the electron spin, $I$ is the nuclear spin of the molecule, $\hat{k}$ is the direction of the molecular axis, and $\hat{z}$ is the direction of the applied magnetic field. For a free BaF molecule the hyperfine constants of Equation 3.19 are $b = h \times 63.509(32)$ MHz and $c = h \times 8.224(58)$ MHz [46]. The resultant energies of Equation 3.19 depend on the angle between $\hat{k}$ and $\hat{z}$. The solid line in Figure 3.36 is the result of calculations performed by EDM$^3$ collaborators for an isotropic distribution of BaF molecules, with the hyperfine constants of Equation 3.19 set to $b = h \times 61$ MHz and $c = h \times 8.4$ MHz. These values are similar to the values $b = h \times 59$ MHz and $c = h \times 8.4$ MHz obtained in Ref. [67], where the BaF molecules studied are also confined within neon matrices. The difference in the measured hyperfine constants of Equation 3.19 for the confined molecule compared to

the free molecule indicate that the matrix exerts an influence on the hyperfine structure of BaF.

### 3.6.3 *Two-pulse experiments*

A two-RF-pulse experiment is used to observe narrower widths and to measure lifetimes for populations in the $X^2\Sigma_{1/2}(F = 0, m_f = 0)$ state. Two RF pulses are used to drive the $X^2\Sigma_{1/2}(F = 1, m_f = 1) \rightarrow X^2\Sigma_{1/2}(F = 0, m_f = 0)$ transition and then return the BaF molecules to the optically-dark $m_f = 1$ sublevel. This process is shown on an energy-level diagram in Figure 3.37. Figure 3.37a shows the first step in which the molecular population that has been optically pumped into the $X^2\Sigma_{1/2}(F = 1, m_f = 1)$ hyperfine sublevel is transferred to the $X^2\Sigma_{1/2}(F = 0, m_f = 0)$ sublevel using a pulse of RF radiation (labelled pulse (i)). A second RF pulse (labelled pulse (ii)) transfers the molecules back to the optically-dark $X^2\Sigma_{1/2}(F = 1, m_f = 1)$ sublevel.

Figure 3.38 shows a timing diagram of pulses in complementary experiments, the first with a single RF pulse inserted between the pulses of $\sigma_+$-polarized light and the second with

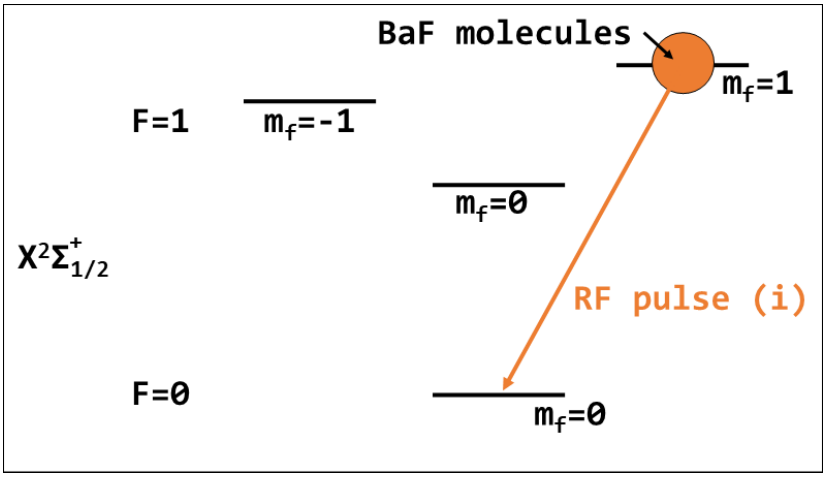


(a)

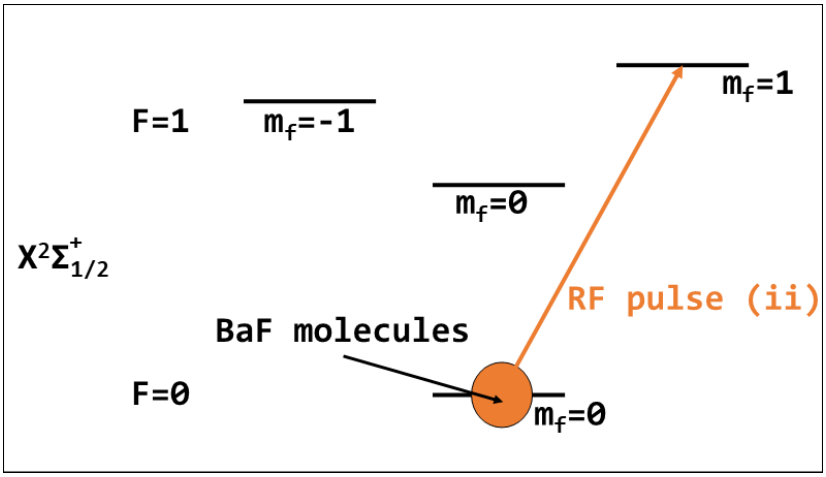


(b)

Figure 3.37: Energy-level diagram for two RF pulses on a population of optically-pumped BaF molecules. Panel (a) shows the effect on a single on-resonance pulse of RF radiation that transfers the BaF molecules from the $X^2\Sigma_{1/2}(F = 1, m_f = 1)$ sublevel to the $X^2\Sigma_{1/2}(F = 0, m_f = 0)$ sublevel. Panel (b) shows the effect of a subsequent pulse that returns the population to the $X^2\Sigma_{1/2}(F = 1, m_f = 1)$ sublevel.

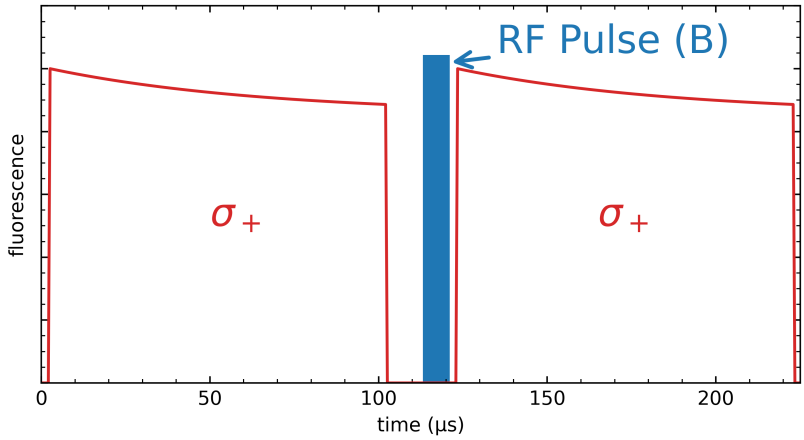


(a)

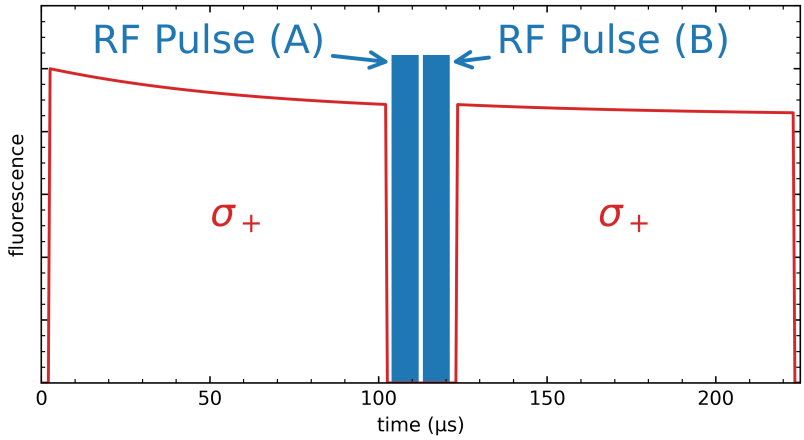


(b)

Figure 3.38: Timing diagram for the two-pulse RF resonance experiments. In panel (a), a single RF pulse (labelled (B)) is inserted just before the second light pulse, causing the return of the optical-pumping signature. In panel (b), two RF pulses are inserted between light pulses. The additional RF pulse occurs just after the first optical pulse. The difference in the average fluorescence between the two complementary experiments shows the reduction of fluorescence for BaF molecules that interact with both RF pulses.

two pulses of RF radiation inserted. Figure 3.38a is a diagram with a single RF pulse (labelled as RF pulse (B)) inserted just before the second pulse of $\sigma_+$-polarized light. When RF pulse (B) is on resonance with the $X^2\Sigma_{1/2}(F = 1, m_f = 1) \rightarrow (F = 0, m_f = 0)$ transition (Figure 3.37a), the optical-pumping signature returns to the fluorescence profile of the second pulse of laser light. Figure 3.38b depicts the case in which two RF pulses (labelled as (A) and (B)) are inserted in the time between the pulses of light. When both RF pulse (A) and (B) are both on resonance with the hyperfine transition, pulse (A) transfers the BaF population to the $F = 0, m_f = 0$ sublevel (as in Figure 3.37a) and pulse (B) transfers this population back to the $F = 1, m_f = 1$ dark state (as in Figure 3.37b). The two pulses therefore cause a reduction in fluorescence (relative to that for a single pulse), as illustrated in Figure 3.38.

The reduction in fluorescence is determined by examining the difference of the fluorescence signals normalized by the average fluorescence signal observed in the complementary experiments depicted in Figure 3.38:

$$\frac{S_2 - S_1}{(S_1 + S_2)/2}. \tag{3.20}$$

Here, $S_1$ is the fluorescence signal observed for the experiment containing only RF pulse (B) (shown in Figure 3.38a), and $S_2$ is the fluorescence signal observed for the experiment in with both RF pulses (shown in Figure 3.38b).

Figure 3.39 shows the ratio given in Equation 3.20 as the RF frequency of pulse (B) is tuned over a range centred at 66.25 MHz. During the experiment RF pulse (A) is kept at a fixed frequency of 66.25 MHz, which is the previously identified centre of resonance for the $X^2\Sigma_{1/2}(F = 1, m_f = 1) \rightarrow X^2\Sigma_{1/2}(F = 0, m_f = 0)$ transition for an applied magnetic field of 1.5 G. This experiment uses 100-$\mu$s pulses of $\sigma_+$-polarized light separated by 21 $\mu$s, with two 8-$\mu$s-long RF pulses of 36 dBm of power 1.25 $\mu$s after the first laser pulse and 1.25 $\mu$s before the second laser pulse. The resonance of the two-pulse experiment has a FWHM of 580(20) kHz, which is narrower than the resonance observed with a single RF pulse (see Figure 3.35). This narrowing is a result of the fact that the first RF pulse selects only a subset of BaF molecules that interact with both RF pulses.

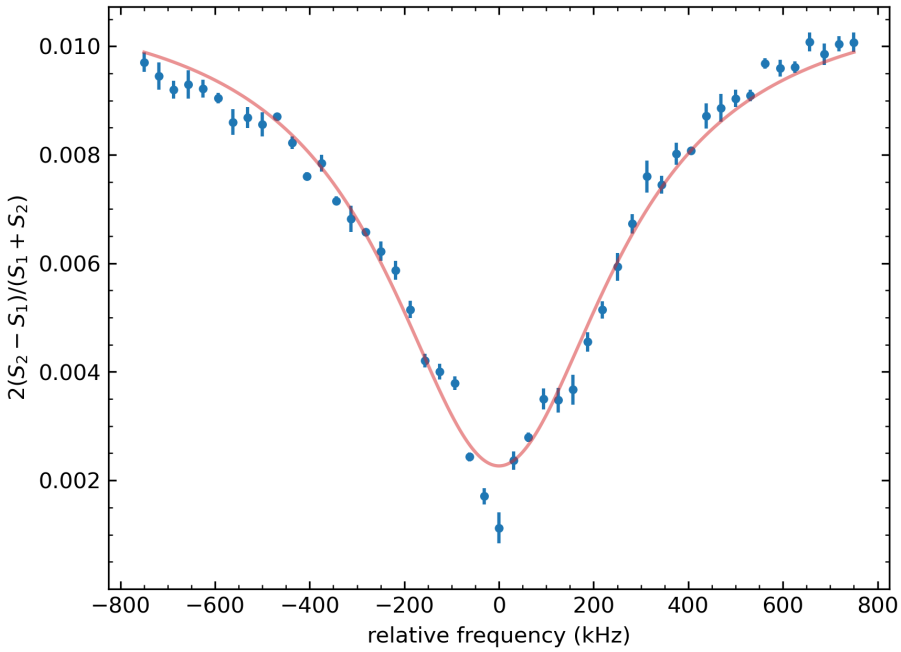


Figure 3.39: Resonance structure produced with two pulses of RF at 36 dBm. The ratio given in Equation 3.20 is shown versus the frequency of RF pulse (B). The resonance is narrower than that of the single-pulse experiment, indicating that a subset of the molecules interact with both RF pulses. The solid line is a fit to a Lorentzian with a FWHM of 580(20) kHz.

The observed width of the two-pulse resonance is narrowed by reducing the RF power, indicating that the observed resonance is power-broadened. The width of the resonance is also limited by $1/T$ (where $T$ is the RF pulse duration), and so the RF power must be reduced and the pulse length increased to obtain the narrowest resonances. Figure 3.40 shows the observed resonance with 6 dBm of power and with an RF pulse duration of 48 $\mu$s (with the time between pulses of excitation laser light adjusted to 101 $\mu$s). A Lorentzian lineshape fit indicates a FWHM of $48(9)$ kHz.

Figure 3.41 shows the observed FWHM of the two-pulse (for pulse durations of ranging from $T = 16$ $\mu$s to $T = 48$ $\mu$s) versus the RF pulse power. As the power of the RF is reduced, the amplitude of the observed resonance diminishes, requiring more averaging time to see the signal. Measurements performed with RF pulse powers of 4 dBm, 6 dBm, and 7 dBm are consistent with a resonance width of $50(10)$ kHz, providing some indication that the resonance is not further reduced at lower powers, and does not reach the expected $1/T = 21$ kHz limit.

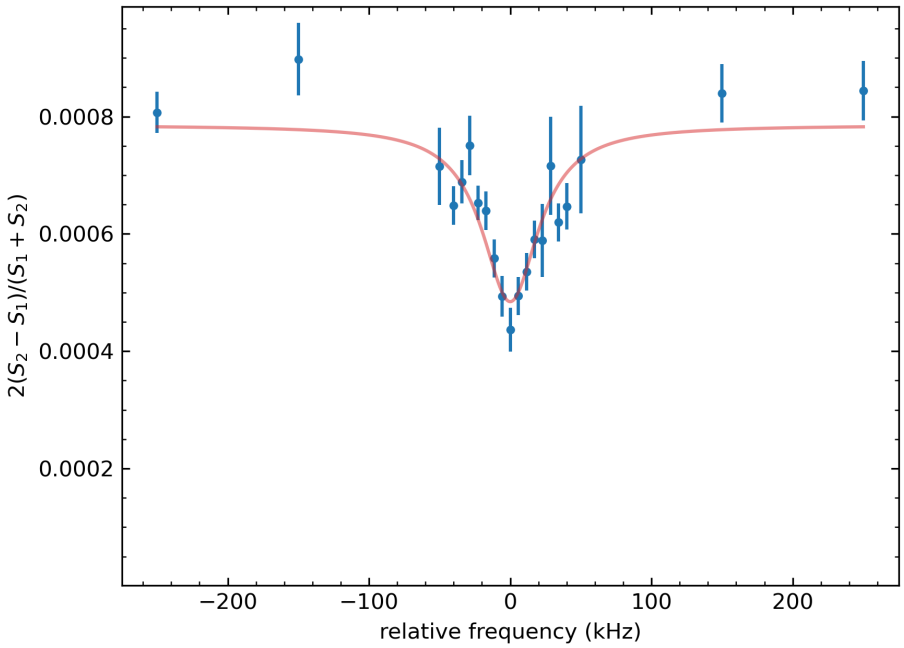


Figure 3.40: Resonance structure produced with two pulses of RF at 6 dBm. The ratio given in Equation 3.20 is shown versus the frequency of RF pulse (B). The solid line is a fit to a Lorentzian with a FWHM of 48(9) kHz.

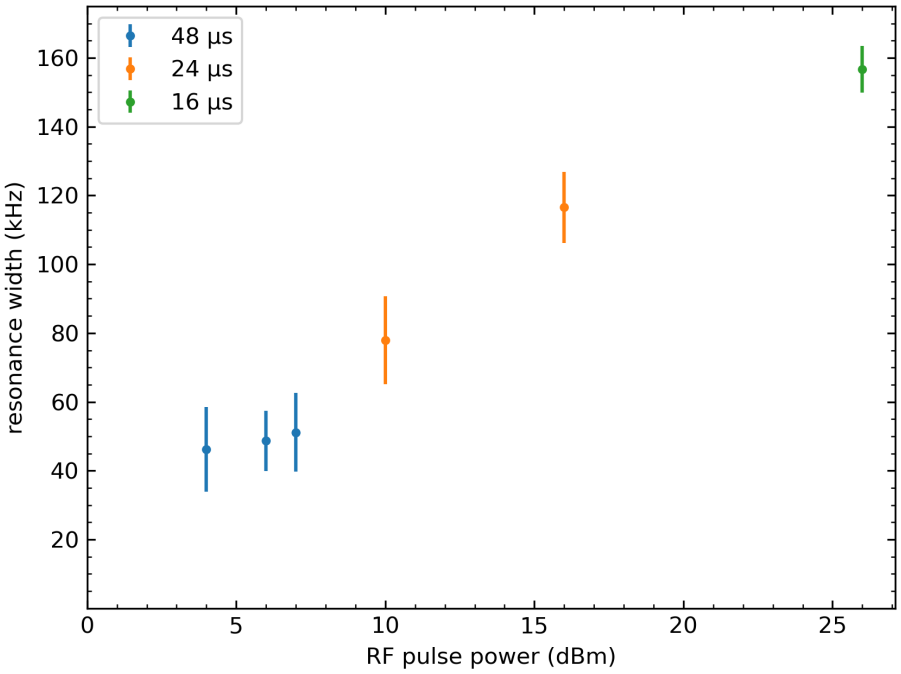


Figure 3.41: RF resonance FWHM versus RF power for the two-pulse experiment. The FWHM decreases as the RF power is decreased until, at low powers, approximately equal resonance widths are found. The FWHM is obtained from a Lorentzian fit for all the data at the corresponding power. The length of RF pulse used in each experiment is indicated by the colour of the data point. Note that the power is reported in dBm, which is a logarithmic unit.

### 3.6.4 *Time constant for population remaining the $F = 0$ hyperfine sublevel*

The time constant associated with the BaF population's ability to remain in the $X^2\Sigma_{1/2}(F = 0, m_f = 0)$ ground state is observed by performing a two-pulse experiment as described in Section 3.6.3, with the power and duration of the RF pulses held constant (at 26 dBm and 8 $\mu$s, respectively) but the time in between the pulses varied. As in the previous section, the frequency of RF pulse (B) (of Figure 3.38) is scanned across a frequency region centred at 66.25 MHz (while pulse (A) is held at a constant 66.25 MHz) with a 1.5-G applied magnetic field. As in the previous section, the first pulse of RF field is 1.25 $\mu$s after a pulse of laser light and the second pulse of RF field is 1.25 $\mu$s before the next pulse of laser light. Figure 3.42 shows the result for these experiments as a function of time between RF pulses. Each data point on Figure 3.42 is obtained from a Lorentzian fit (similar to Figure 3.40) and gives the percentage decrease that occurs when pulse (B) is on resonance. This percentage gives an estimate of the percentage of BaF molecules that interact with both RF pulses. Varying the time between the pulses allows for a de-

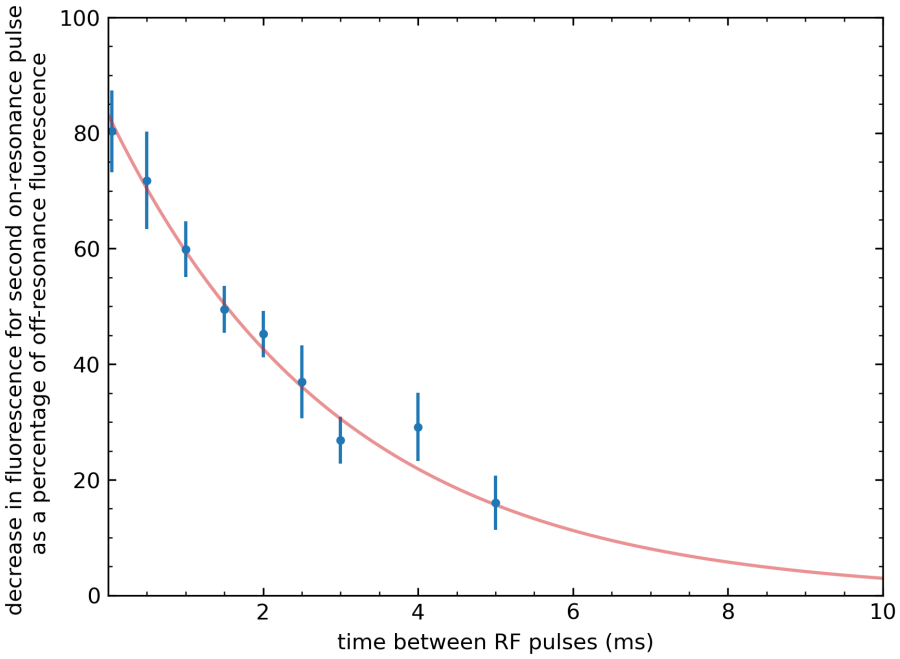


Figure 3.42: Two-pulse RF experiment at 5.8 K versus the time gap between pulses. Each point on this figure represents an experiment result (similar to that shown in Figure 3.39) for a specific time gap between RF pulses with the substrate held at a temperature of 5.8 K. The $y$-axis is the decrease in fluorescence for a second pulse on resonance as a percentage of off-resonance fluorescence. The solid line is an exponential fit which returns a time constant of $\tau_0 = 3.0(2)$ ms.

termination of the time constant for molecules remaining in the $F = 0, m_f = 0$ sublevel. This time constant is found from an exponential fit (shown in Figure 3.42) to be $\tau_0 = 3.0(2)$ ms.

This time constant is an order of magnitude larger than the time constant ($\tau_{\text{dark}}$, from the fit in Figure 3.31) that is associated with the time population remains in the $F = 1, m_f = 1$ sublevel. The larger time constant is likely due to the fact that the $X^2\Sigma_{1/2}(F = 0, m_f = 0)$ sublevel is farther displaced in energy from the other hyperfine states (see Figure 3.32).

The thermal phonons of the matrix provide the excess energy needed to redistribute hyperfine populations and so it is expected that the observed time constant would increase drastically for solids at colder temperatures. Figure 3.43 shows the observed time constant ($\tau_0$) versus temperature (with each point representing a full experiment similar to that of Figure 3.42). Because of the reduction in both fluorescence and time constant, measurements at higher temperatures take progressively longer times for obtaining similar uncertainty. The data shown represent several days of continuous mea-

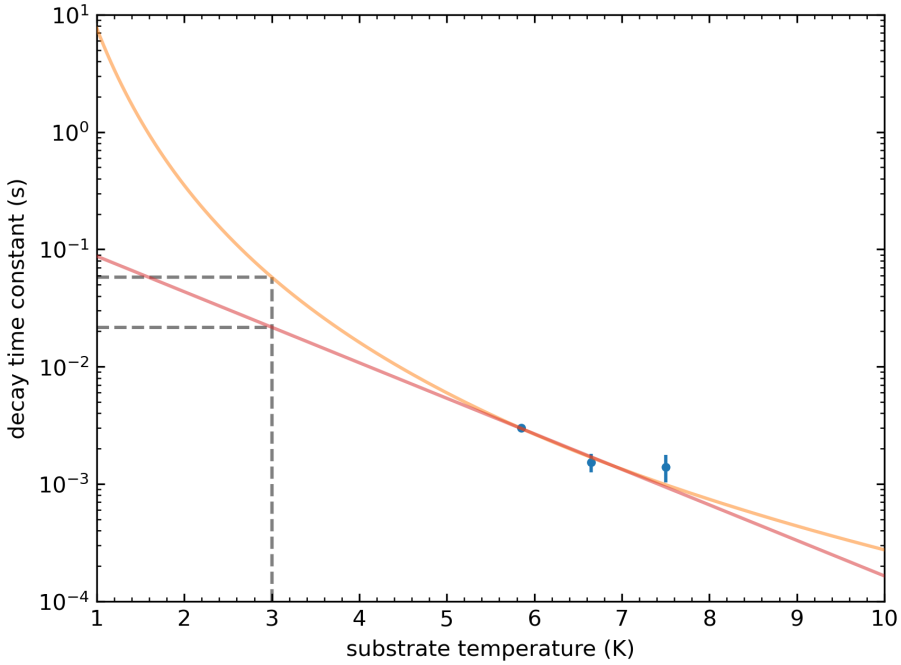


Figure 3.43: Decay time constant for two-pulse RF experiments versus temperature. The time constants from experiments similar to that shown in Figure 3.42 at three different temperatures. The red line is an exponential fit to the data while the orange solid line is a power-law fit.

surements.

Both a power-law and a exponential fit are shown for the limited data of Figure 3.43. A power-law fit of the form $\tau_0(T) = AT^B$, shown in orange yields $B = -4(1)$ and an exponential fit of the form $\tau_0(T) = Ce^{-DT}$, shown in red yields $D = 1.4(4)\ K^{-1}$. With the limited data taken, neither relation can be excluded. Regardless, the trend suggests that considerable improvement can be made in the ability to control the BaF populations at colder temperatures. With the current cryocooler, temperatures of 3 K are possible with well-controlled thermal loads. Dashed lines in Figure 3.43 are drawn to show the time constant at 3 K would likely lie between $\tau_0 = 20$ ms and $\tau_0 = 60$ ms. A forced-evaporation helium cooling system could achieve temperatures as cold as 1 K, leading to a time constant that is of order 1 s.

# 4 CONCLUSION AND OUTLOOK

## 4.1 CONCLUSION

This work reports on the progress towards a measurement of $d_e$ using the EDM$^3$ method. A measurement of the electron's electric dipole moment is a search for large CP-violating processes which could lead to an understanding of the imbalance of matter and antimatter in the universe. A measurement of $d_e \geq 10^{-35}$ $e$ cm would represent the first detection of BSM physics. A first measurement using the EDM$^3$ method is estimated to have a two-orders-of-magnitude better precision than current methods of measuring $d_e$, with the possibility of further improvement to bridge the gap between the current most precise measurement and the theoretical expectation of the Standard Model.

A complete description of the experimental apparatus is given in Chapter 2. This apparatus combines a helium-buffer-gas cooled laser-ablation source to produce BaF molecules and the growth of cryogenic neon matrices by vapour deposition.

Chapter 3 reports the results of experiments performed, with a goal of demonstrating steps necessary for a measurement of $d_e$. In Section 3.1.4 the buffer-gas cooled laser-ablation source is shown to produce approximately 9 billion BaF molecules per ablation laser pulse. During a typical, hour-long, growth an estimate is made that $10^{11}$ per mm$^2$ molecules are directed at the substrate. Assuming a capture efficiency of near unity and volume of solid neon of approximately 1 mm$^3$, the number of confined BaF molecules within the matrix would represent a BaF:Ne concentration of 1 ppb, which is the target concentration for a first measurement. The ideal ablation parameters the source presented in this work are reported in Section 3.1, while growth and annealing procedures are described in Section 3.2.

In Section 3.3 several electronic excited states for BaF molecules within the neon matrix are identified and characterized by their respective excitation and fluorescence profiles. In Section 3.3.2 the observed laser-induced fluorescence resulting from excitation to the $B^2\Sigma_{1/2}(v = 0)$ state is reported and two dominant decay paths are observed corresponding to $B^2\Sigma_{1/2}(v = 0) \rightarrow X^2\Sigma_{1/2}(v = 1)$ and $B^2\Sigma_{1/2}(v = 0) \rightarrow A'^2\Delta_{3/2} \rightarrow X^2\Sigma_{1/2}$ decays. Decays to the $X^2\Sigma_{1/2}(v = 2)$ and $X^2\Sigma_{1/2}(v = 3)$ states from molecules excited to the $B^2\Sigma_{1/2}(v = 0)$ state are also observed and provide measurements of the effect of the neon matrix on the separation of the $v = 1$-to-$v = 2$ and $v = 2$-to-$v = 3$ vibrational levels of the electronic ground state of the BaF molecule.

In Sections 3.3.3, 3.3.4, and 3.3.5 several lifetimes associated with the decay of laser-excited BaF molecules are observed and, in Section 3.3.6, these decays are shown to be dominated by the observed radiative decay process. In Section 3.4.2 an estimate is made of the total density of BaF molecules within the matrix using laser-induced fluorescence of the $X^2\Sigma_{1/2} \rightarrow B^2\Sigma_{1/2}(v = 0)$ excitation. It is found

that $N_{\text{total}} = (5 \pm 3) \times 10^{10}/\text{mm}^2$ BaF molecules are confined within the solid indicating a BaF to neon ratio of approximately 1 ppb, which is the desired concentration for a measurement at a precision of $5 \times 10^{-32}$ $e$ cm.

In Section 3.5, optical pumping BaF molecules is demonstrated (via laser-excitation to the $A^2\Pi_{1/2}(v = 0)$ excited state) into the $X^2\Sigma_{1/2}(F = 1, m_f = 1)$ hyperfine sublevel using circularly polarized laser light. In Section 3.6.1, RF fields are used to transfer the BaF population from the $X^2\Sigma_{1/2}(F = 1, m_f = 1)$ sublevel to the $X^2\Sigma_{1/2}(F = 0, m_f = 0)$ sublevel and in Section 3.6.3 a sequence of two pulses of RF field is used to transfer the BaF population back into the optically-dark $X^2\Sigma_{1/2}(F = 1, m_f = 1)$ sublevel. BaF molecules that are transferred into the $X^2\Sigma_{1/2}(F = 0, m_f = 0)$ sublevel by the first RF pulse are found to remain in this sublevel for times longer than 3 ms for matrices at 5.8 K.

## 4.2 FUTURE DIRECTIONS

The purity of the BaF-doped neon matrix will need to be improved, as known ablation by-products (e.g., Ba and $BaF_2$)

currently embed themselves within the solid alongside the BaF molecules. To remove impurities produced from laser ablation, a modification to the apparatus to include an electrostatic deflector [76] is underway. This deflector targets the $X^2\Sigma_{1/2}(v = 0, N = 1)$ rotational state of the BaF molecule, redirecting the BaF molecules produced from the buffer-gas-cooled laser-ablation cell along a trajectory inaccessible to other undeflected ablation products.

Improvements to the growth and annealing procedures will also be required to optimize the sample. A possibility for an improvement of growth procedure is the formation of a perfect crystal of neon from a seed layer, initially formed from a liquid [66, 89], which may prove to create more uniform trapping sites for BaF molecules within the host matrix.

Modifications that reduce the thermal load on the cryogenic apparatus to achieve a base temperature of 3 K (the minimum operating temperature of the cryocooler in this system) are underway. These modifications includes further limiting black-body radiation from room-temperature components that surround the apparatus and reducing the partial

pressure of helium gas between the inner and outer layers of the cryogenic apparatus after growth. A lower temperature of 1 K will require a new cryogenic refrigeration system.

To perform a measurement of the electron's electric dipole moment using the EDM$^3$ method, further steps must be demonstrated. The ability to place the molecules into an even and odd superposition of the $m_f = 1$ and $m_f = -1$ hyperfine states via $\hat{X}$- or $\hat{Y}$-polarized RF pulses and allowing the system to evolve freely for times of $t_p \approx 10$ ms remains to be demonstrated. Coherence of the molecules, determined by the homogeneity of the environment, including the local magnetic fields experienced by the BaF molecules has not yet been demonstrated. It will be necessary to obtain isotopically pure $^{20}$Ne to limit the presence of $^{21}$Ne and $^{22}$Ne. Producing uniform neon matrices with homogeneous magnetic fields across the small sample volume will be necessary to achieve the coherence times required for a high-precision measurement.

# BIBLIOGRAPHY


[1] A. C. Vutha, M. Horbatsch, and E. A. Hessels. "Oriented Polar Molecules in a Solid Inert-Gas Matrix: A Proposed Method for Measuring the Electric Dipole Moment of the Electron." In: *Atoms* 6.1 (2018). ISSN: 2218-2004. DOI: 10.3390/atoms6010003. URL: https://www.mdpi.com/2218-2004/6/1/3.

[2] O. W. Greenberg. "*CPT* Violation Implies Violation of Lorentz Invariance." In: *Phys. Rev. Lett.* 89 (23 2002), p. 231602. DOI: 10.1103/PhysRevLett.89.231602. URL: https://link.aps.org/doi/10.1103/PhysRevLett.89.231602.

[3] T. D. Lee and C. N. Yang. "Question of Parity Conservation in Weak Interactions." In: *Phys. Rev.* 104 (1 1956), pp. 254–258. DOI: 10.1103/PhysRev.104.254. URL: https://link.aps.org/doi/10.1103/PhysRev.104.254.

[4] C. S. Wu, E. Ambler, R. W. Hayward, D. D. Hoppes, and R. P. Hudson. "Experimental Test of Parity Conservation in Beta Decay." In: *Phys. Rev.* 105 (4 1957), pp. 1413–1415. DOI: 10.1103/PhysRev.105.1413. URL: https://link.aps.org/doi/10.1103/PhysRev.105.1413.

[5] T. D. Lee, Reinhard Oehme, and C. N. Yang. "Remarks on Possible Noninvariance under Time Reversal and Charge Conjugation." In: *Phys. Rev.* 106 (2 1957), pp. 340–345. DOI: 10.1103/PhysRev.106.340. URL: https://link.aps.org/doi/10.1103/PhysRev.106.340.

[6] Andrei D Sakharov. "Violation of CP invariance, C asymmetry, and baryon asymmetry of the universe." In: *Soviet Physics Uspekhi* 34.5 (1991), p. 392. DOI: 10.1070/PU1991v034n05ABEH002497. URL: https://dx.doi.org/10.1070/PU1991v034n05ABEH002497.

[7] Makoto Kobayashi and Toshihide Maskawa. "CP-Violation in the Renormalizable Theory of Weak Interaction." In: *Progress of Theoretical Physics* 49.2 (1973), pp. 652–657. ISSN: 0033-068X. DOI: 10.1143/PTP.49.652. eprint: https://academic.oup.com/ptp/article-pdf/49/2/

652/5257692/49-2-652.pdf. URL: https://doi.org/10.1143/PTP.49.652.

[8] Michael Dine and Alexander Kusenko. "Origin of the matter-antimatter asymmetry." In: *Rev. Mod. Phys.* 76 (1 2003), pp. 1–30. DOI: 10.1103/RevModPhys.76.1. URL: https://link.aps.org/doi/10.1103/RevModPhys.76.1.

[9] E. M. Purcell and N. F. Ramsey. "On the Possibility of Electric Dipole Moments for Elementary Particles and Nuclei." In: *Phys. Rev.* 78 (6 1950), pp. 807–807. DOI: 10.1103/PhysRev.78.807. URL: https://link.aps.org/doi/10.1103/PhysRev.78.807.

[10] Tanya S. Roussy, Luke Caldwell, Trevor Wright, William B. Cairncross, Yuval Shagam, Kia Boon Ng, Noah Schlossberger, Sun Yool Park, Anzhou Wang, Jun Ye, and Eric A. Cornell. "An improved bound on the electron's electric dipole moment." In: *Science* 381.6653 (2023), pp. 46–50. DOI: 10.1126/science.adg4084. eprint: https://www.science.org/doi/pdf/10.1126/science.adg4084. URL: https://www.science.org/doi/abs/10.1126/science.adg4084.

[11] Yohei Ema, Ting Gao, and Maxim Pospelov. "Standard Model Prediction for Paramagnetic Electric Dipole Moments." In: *Phys. Rev. Lett.* 129 (23 2022), p. 231801. DOI: 10.1103/PhysRevLett.129.231801. URL: https://link.aps.org/doi/10.1103/PhysRevLett.129.231801.

[12] Yasuhiro Yamaguchi and Nodoka Yamanaka. "Large Long-Distance Contributions to the Electric Dipole Moments of Charged Leptons in the Standard Model." In: *Phys. Rev. Lett.* 125 (24 2020), p. 241802. DOI: 10.1103/PhysRevLett.125.241802. URL: https://link.aps.org/doi/10.1103/PhysRevLett.125.241802.

[13] Sebastian A. R. Ellis and Gordon L. Kane. "Theoretical prediction and impact of fundamental electric dipole moments." In: *Journal of High Energy Physics* 2016.1 (2016), p. 77. ISSN: 1029-8479.

[14] Pavel Fileviez Pérez and Alexis D. Plascencia. "Electric dipole moments, new forces and dark matter." In: *Journal of High Energy Physics* 2021.3 (2021), p. 185. ISSN: 1029-8479.

[15] Marco Ardu, Moinul Hossain Rahat, Nicola Valori, and Oscar Vives. "Electric Dipole Moments as indi-

rect probes of dark sectors." In: *Journal of High Energy Physics* 2024.11 (2024), p. 49. ISSN: 1029-8479.

[16] V. Andreev, D. G. Ang, D. DeMille, J. M. Doyle, G. Gabrielse, J. Haefner, N. R. Hutzler, Z. Lasner, C. Meisenhelder, B. R. O'Leary, C. D. Panda, A. D. West, E. P. West, and X. Wu (A. C. M. E. Collaboration). "Improved limit on the electric dipole moment of the electron." In: *Nature* 562.7727 (2018), pp. 355–360. ISSN: 1476-4687. DOI: 10.1038/s41586-018-0599-8. URL: https://doi.org/10.1038/s41586-018-0599-8.

[17] William B. Cairncross, Daniel N. Gresh, Matt Grau, Kevin C. Cossel, Tanya S. Roussy, Yiqi Ni, Yan Zhou, Jun Ye, and Eric A. Cornell. "Precision Measurement of the Electron's Electric Dipole Moment Using Trapped Molecular Ions." In: *Phys. Rev. Lett.* 119 (15 2017), p. 153001. DOI: 10.1103/PhysRevLett.119.153001. URL: https://link.aps.org/doi/10.1103/PhysRevLett.119.153001.

[18] J. Baron, W. C. Campbell, D. DeMille, J. M. Doyle, G. Gabrielse, Y. V. Gurevich, P. W. Hess, N. R. Hutzler, E. Kirilov, I. Kozyryev, B. R. O'Leary, C. D. Panda, M. F. Parsons, E. S. Petrik, B. Spaun, A. C. Vutha, and

A. D. West (The ACME Collaboration). "Order of Magnitude Smaller Limit on the Electric Dipole Moment of the Electron." In: *Science* 343.6168 (2014), pp. 269–272. DOI: 10.1126/science.1248213. eprint: https://www.science.org/doi/pdf/10.1126/science.1248213. URL: https://www.science.org/doi/abs/10.1126/science.1248213.

[19] J. J. Hudson, D. M. Kara, I. J. Smallman, B. E. Sauer, M. R. Tarbutt, and E. A. Hinds. "Improved measurement of the shape of the electron." In: *Nature* 473.7348 (2011), pp. 493–496. ISSN: 1476-4687. DOI: 10.1038/nature10104.

[20] B. C. Regan, Eugene D. Commins, Christian J. Schmidt, and David DeMille. "New Limit on the Electron Electric Dipole Moment." In: *Phys. Rev. Lett.* 88 (7 2002), p. 071805. DOI: 10.1103/PhysRevLett.88.071805.

[21] J. J. Hudson, B. E. Sauer, M. R. Tarbutt, and E. A. Hinds. "Measurement of the Electron Electric Dipole Moment Using YbF Molecules." In: *Phys. Rev. Lett.* 89 (2 2002), p. 023003. DOI: 10.1103/PhysRevLett.89.023003. URL: https://link.aps.org/doi/10.1103/PhysRevLett.89.023003.

[22] Eugene D. Commins, Stephen B. Ross, David DeMille, and B. C. Regan. "Improved experimental limit on the electric dipole moment of the electron." In: *Phys. Rev. A* 50 (4 1994), pp. 2960–2977. DOI: 10.1103/PhysRevA.50.2960. URL: https://link.aps.org/doi/10.1103/PhysRevA.50.2960.

[23] K. Abdullah, C. Carlberg, E. D. Commins, Harvey Gould, and Stephen B. Ross. "New experimental limit on the electron electric dipole moment." In: *Phys. Rev. Lett.* 65 (19 1990), pp. 2347–2350. DOI: 10.1103/PhysRevLett.65.2347. URL: https://link.aps.org/doi/10.1103/PhysRevLett.65.2347.

[24] D. Cho, K. Sangster, and E. A. Hinds. "Tenfold improvement of limits on T violation in thallium fluoride." In: *Phys. Rev. Lett.* 63 (23 1989), pp. 2559–2562. DOI: 10.1103/PhysRevLett.63.2559. URL: https://link.aps.org/doi/10.1103/PhysRevLett.63.2559.

[25] S. A. Murthy, D. Krause, Z. L. Li, and L. R. Hunter. "New limits on the electron electric dipole moment from cesium." In: *Phys. Rev. Lett.* 63 (9 1989), pp. 965–968. DOI: 10.1103/PhysRevLett.63.965. URL: https://link.aps.org/doi/10.1103/PhysRevLett.63.965.

[26] A. C. Vutha, M. Horbatsch, and E. A. Hessels. "Orientation-dependent hyperfine structure of polar molecules in a rare-gas matrix: A scheme for measuring the electron electric dipole moment." In: *Phys. Rev. A* 98 (3 2018), p. 032513. DOI: 10.1103/PhysRevA.98.032513. URL: https://link.aps.org/doi/10.1103/PhysRevA.98.032513.

[27] G.K. Koyanagi, R.L. Lambo, A. Ragyanszki, R. Fournier, M. Horbatsch, and E.A. Hessels. "Accurate calculation of the interaction of a barium monofluoride molecule with an argon atom: A step towards using matrix isolation of BaF for determining the electron electric dipole moment." In: *Journal of Molecular Spectroscopy* 391 (2023), p. 111736. ISSN: 0022-2852. DOI: https://doi.org/10.1016/j.jms.2023.111736. URL: https://www.sciencedirect.com/science/article/pii/S0022285223000012.

[28] Andrew N. Kanagin, Sameer K. Regmi, Pawan Pathak, and Jonathan D. Weinstein. "Optical pumping of rubidium atoms frozen in solid argon." In: *Phys. Rev. A* 88 (6 2013), p. 063404. DOI: 10.1103/PhysRevA.88.063404.

URL: https://link.aps.org/doi/10.1103/PhysRevA.88.063404.

[29] S. I. Kanorsky, S. Lang, S. Lücke, S. B. Ross, T. W. Hänsch, and A. Weis. "Millihertz magnetic resonance spectroscopy of Cs atoms in body-centered-cubic $^4$He." In: *Phys. Rev. A* 54 (2 1996), R1010–R1013. DOI: 10.1103/PhysRevA.54.R1010. URL: https://link.aps.org/doi/10.1103/PhysRevA.54.R1010.

[30] R. Lambo, C.-Y. Xu, S. T. Pratt, H. Xu, J. C. Zappala, K. G. Bailey, Z.-T. Lu, P. Mueller, T. P. O'Connor, B. B. Kamorzin, D. S. Bezrukov, Y.-Q. Xie, A. A. Buchachenko, and J. T. Singh. "High-resolution spectroscopy of neutral Yb atoms in a solid Ne matrix." In: *Phys. Rev. A* 104 (6 2021), p. 062809. DOI: 10.1103/PhysRevA.104.062809. URL: https://link.aps.org/doi/10.1103/PhysRevA.104.062809.

[31] Barry Davis and John G. McCaffrey. "Luminescence of Atomic Barium in Rare Gas Matrices: A Two-Dimensional Excitation/Emission Spectroscopy Study." In: *The Journal of Physical Chemistry A* 122.37 (2018), pp. 7339–7350. ISSN: 1089-5639.

[32] Ugne Dargyte, David M. Lancaster, and Jonathan D. Weinstein. "Optical and spin-coherence properties of rubidium atoms trapped in solid neon." In: *Phys. Rev. A* 104 (3 2021), p. 032611. DOI: 10.1103/PhysRevA.104.032611. URL: https://link.aps.org/doi/10.1103/PhysRevA.104.032611.

[33] David M. Lancaster, Ugne Dargyte, and Jonathan D. Weinstein. "Optical spin readout of single rubidium atoms trapped in solid neon." In: *Phys. Rev. Res.* 6 (1 2024), p. L012048. DOI: 10.1103/PhysRevResearch.6.L012048. URL: https://link.aps.org/doi/10.1103/PhysRevResearch.6.L012048.

[34] H. S. Nataraj, B. K. Sahoo, B. P. Das, and D. Mukherjee. "Intrinsic Electric Dipole Moments of Paramagnetic Atoms: Rubidium and Cesium." In: *Phys. Rev. Lett.* 101 (2008), p. 033002.

[35] W. H. Flygare. "Molecular Rotation in the Solid State. Theory of Rotation of Trapped Molecules in Rare-Gas Lattices." In: *The Journal of Chemical Physics* 39.9 (1963), pp. 2263–2273. ISSN: 0021-9606. DOI: 10.1063/1.1701428. eprint: https://pubs.aip.org/aip/jcp/article-

pdf/39/9/2263/18831616/2263_1_online.pdf. URL: https://doi.org/10.1063/1.1701428.

[36] Toni Kiljunen, Burkhard Schmidt, and Nikolaus Schwentner. "Aligning and orienting molecules trapped in octahedral crystal fields." In: *Phys. Rev. A* 72 (5 2005), p. 053415. DOI: 10.1103/PhysRevA.72.053415. URL: https://link.aps.org/doi/10.1103/PhysRevA.72.053415.

[37] Toni Kiljunen, Burkhard Schmidt, and Nikolaus Schwentner. "Time-dependent alignment of molecules trapped in octahedral crystal fields." In: *The Journal of Chemical Physics* 124.16 (2006), p. 164502. ISSN: 0021-9606. DOI: 10.1063/1.2189239. eprint: https://pubs.aip.org/aip/jcp/article-pdf/doi/10.1063/1.2189239/15384475/164502_1_online.pdf. URL: https://doi.org/10.1063/1.2189239.

[38] T. Kiljunen and B. Schmidt. "Alignement and orientation of molecules in matrices." In: vol. 87. Berlin, Heidelberg: Springer Berlin Heidelberg, 2007, pp. 337–352. ISBN: 978-3-540-68038-3. DOI: 10.1007/978-3-540-68038-3_4. URL: https://doi.org/10.1007/978-3-540-68038-3_4.

[39] M. Abe, V. S. Prasannaa, and B. P. Das. "Application of the finite-field coupled-cluster method to calculate molecular properties relevant to electron electric-dipole-moment searches." In: *Phys. Rev. A* 97 (3 2018), p. 032515. DOI: 10.1103/PhysRevA.97.032515. URL: https://link.aps.org/doi/10.1103/PhysRevA.97.032515.

[40] M. Abe, G. Gopakumar, M. Hada, B. P. Das, H. Tatewaki, and D. Mukherjee. "Application of relativistic coupled-cluster theory to the effective electric field in YbF." In: *Phys. Rev. A* 90 (2 2014), p. 022501. DOI: 10.1103/PhysRevA.90.022501. URL: https://link.aps.org/doi/10.1103/PhysRevA.90.022501.

[41] Sudip Sasmal, Himadri Pathak, Malaya K. Nayak, Nayana Vaval, and Sourav Pal. "Relativistic coupled-cluster study of RaF as a candidate for the parity- and time-reversal-violating interaction." In: *Phys. Rev. A* 93 (6 2016), p. 062506. DOI: 10.1103/PhysRevA.93.062506. URL: https://link.aps.org/doi/10.1103/PhysRevA.93.062506.

[42] Masahiro Fukuda, Kota Soga, Masato Senami, and Akitomo Tachibana. "Local spin dynamics with the electron

electric dipole moment." In: *Phys. Rev. A* 93 (1 2016), p. 012518. DOI: 10.1103/PhysRevA.93.012518. URL: https://link.aps.org/doi/10.1103/PhysRevA.93.012518.

[43] V. S. Prasannaa, A. C. Vutha, M. Abe, and B. P. Das. "Mercury Monohalides: Suitability for Electron Electric Dipole Moment Searches." In: *Phys. Rev. Lett.* 114 (18 2015), p. 183001. DOI: 10.1103/PhysRevLett.114.183001. URL: https://link.aps.org/doi/10.1103/PhysRevLett.114.183001.

[44] Ch. Ryzlewicz and T. Törring. "Formation and microwave spectrum of the 2-radical barium-monofluoride." In: *Chemical Physics* 51.3 (1980), pp. 329–334. ISSN: 0301-0104. DOI: https://doi.org/10.1016/0301-0104(80)80107-8. URL: https://www.sciencedirect.com/science/article/pii/0301010480801078.

[45] Ch. Ryzlewicz, H.-U. Schütze-Pahlmann, J. Hoeft, and T. Törring. "Rotational spectrum and hyperfine structure of the 2 radicals BaF and BaCl." In: *Chemical Physics* 71.3 (1982), pp. 389–399. ISSN: 0301-0104. DOI: https://doi.org/10.1016/0301-0104(82)85045-3. URL:

https://www.sciencedirect.com/science/article/pii/0301010482850453.

[46] W. E. Ernst, J. Kändler, and T. Törring. "Hyperfine structure and electric dipole moment of BaF $X^2\Sigma^+$." In: *The Journal of Chemical Physics* 84.9 (1986), pp. 4769–4773. ISSN: 0021-9606. DOI: 10.1063/1.449961. eprint: https://pubs.aip.org/aip/jcp/article-pdf/84/9/4769/18958039/4769_1_online.pdf. URL: https://doi.org/10.1063/1.449961.

[47] Timothy C. Steimle, Sarah Frey, Anh Le, David DeMille, David. A. Rahmlow, and Colan Linton. "Molecular-beam optical Stark and Zeeman study of the $A\ ^2\Pi$–$X\ ^2\Sigma^+$ (0,0) band system of BaF." In: *Phys. Rev. A* 84 (1 2011), p. 012508. DOI: 10.1103/PhysRevA.84.012508. URL: https://link.aps.org/doi/10.1103/PhysRevA.84.012508.

[48] Gang Jiang Shuying Kang Fangguang Kuang and Jiguang Du. "The suitability of barium monofluoride for laser cooling from ab initio study." In: *Molecular Physics* 114.6 (2016), pp. 810–818. DOI: 10.1080/00268976.2015.1121294. URL: https://doi.org/10.1080/00268976.2015.1121294.

[49] Liang Xu, Bin Wei, Yong Xia, Lian-Zhong Deng, and Jian-Ping Yin. "BaF radical: A promising candidate for laser cooling and magneto-optical trapping*." In: *Chinese Physics B* 26.3 (2017), p. 033702. DOI: 10.1088/1674-1056/26/3/033702. URL: https://dx.doi.org/10.1088/1674-1056/26/3/033702.

[50] Tao Chen, Wenhao Bu, and Bo Yan. "Structure, branching ratios, and a laser-cooling scheme for the $^{138}$BaF molecule." In: *Phys. Rev. A* 94 (6 2016), p. 063415. DOI: 10.1103/PhysRevA.94.063415. URL: https://link.aps.org/doi/10.1103/PhysRevA.94.063415.

[51] Yongliang Hao et al. "High accuracy theoretical investigations of CaF, SrF, and BaF and implications for laser-cooling." In: *The Journal of Chemical Physics* 151.3 (2019), p. 034302. ISSN: 0021-9606. DOI: 10.1063/1.5098540. eprint: https://pubs.aip.org/aip/jcp/article-pdf/doi/10.1063/1.5098540/13941645/034302_1_online.pdf. URL: https://doi.org/10.1063/1.5098540.

[52] A. Bernard, C. Effantin, E. Andrianavalona, J. Vergès, and R.F. Barrow. "Laser-induced fluorescence of BaF: Further results for six electronic states." In: *Journal of*

*Molecular Spectroscopy* 152.1 (1992), pp. 174–178. ISSN: 0022-2852. DOI: https://doi.org/10.1016/0022-2852(92)90127-A. URL: https://www.sciencedirect.com/science/article/pii/002228529290127A.

[53] Tao Chen, Wenhao Bu, and Bo Yan. "Radiative deflection of a BaF molecular beam via optical cycling." In: *Phys. Rev. A* 96 (5 2017), p. 053401. DOI: 10.1103/PhysRevA.96.053401. URL: https://link.aps.org/doi/10.1103/PhysRevA.96.053401.

[54] P. Aggarwal, V. R. Marshall, H. L. Bethlem, A. Boeschoten, A. Borschevsky, M. Denis, K. Esajas, Y. Hao, S. Hoekstra, K. Jungmann, T. B. Meijknecht, M. C. Mooij, R. G. E. Timmermans, A. Touwen, W. Ubachs, S. M. Vermeulen, L. Willmann, Y. Yin, and A. Zapara. "Lifetime measurements of the $A\ ^2\Pi_{1/2}$ and $A\ ^2\Pi_{3/2}$ states in BaF." In: *Phys. Rev. A* 100 (5 2019), p. 052503. DOI: 10.1103/PhysRevA.100.052503. URL: https://link.aps.org/doi/10.1103/PhysRevA.100.052503.

[55] Felix Kogel, Marian Rockenhäuser, Ralf Albrecht, and Tim Langen. "A laser cooling scheme for precision measurements using fermionic barium monofluoride (137Ba19F) molecules." In: *New Journal of Physics* 23.9

(2021), p. 095003. DOI: 10.1088/1367-2630/ac1df2. URL: https://dx.doi.org/10.1088/1367-2630/ac1df2.

[56] Wenhao Bu, Yuhe Zhang, Qian Liang, Tao Chen, and Bo Yan. "Saturated absorption spectroscopy of buffer-gas-cooled Barium monofluoride molecules." In: *Frontiers of Physics* 17.6 (2022), p. 62502. ISSN: 2095-0470. DOI: 10.1007/s11467-022-1194-x. URL: https://doi.org/10.1007/s11467-022-1194-x.

[57] T Courageux, A Cournol, D Comparat, B Viaris de Lesegno, and H Lignier. "Efficient rotational cooling of a cold beam of barium monofluoride." In: *New Journal of Physics* 24.2 (2022), p. 025007. DOI: 10.1088/1367-2630/ac511a. URL: https://dx.doi.org/10.1088/1367-2630/ac511a.

[58] Marian Rockenhäuser, Felix Kogel, Einius Pultinevicius, and Tim Langen. "Absorption spectroscopy for laser cooling and high-fidelity detection of barium monofluoride molecules." In: *Phys. Rev. A* 108 (6 2023), p. 062812. DOI: 10.1103/PhysRevA.108.062812. URL: https://link.aps.org/doi/10.1103/PhysRevA.108.062812.

[59] B. J. Heidenreich, O. T. Elliott, N. D. Charney, K. A. Virgien, A. W. Bridges, M. A. McKeon, S. K. Peck, D.

Krause, J. E. Gordon, L. R. Hunter, and S. K. Lamoreaux. "Limit on the Electron Electric Dipole Moment in Gadolinium-Iron Garnet." In: *Phys. Rev. Lett.* 95 (25 2005), p. 253004. DOI: 10.1103/PhysRevLett.95.253004. URL: https://link.aps.org/doi/10.1103/PhysRevLett.95.253004.

[60] Y. J. Kim, C.-Y. Liu, S. K. Lamoreaux, G. Visser, B. Kunkler, A. N. Matlashov, J. C. Long, and T. G. Reddy. "New experimental limit on the electric dipole moment of the electron in a paramagnetic insulator." In: *Phys. Rev. D* 91 (10 2015), p. 102004. DOI: 10.1103/PhysRevD.91.102004. URL: https://link.aps.org/doi/10.1103/PhysRevD.91.102004.

[61] D. N. Batchelder, D. L. Losee, and R. O. Simmons. "Isotope Effects in the Lattice Constant and Thermal Expansion of $^{20}$Ne and $^{22}$Ne Single Crystals." In: *Phys. Rev.* 173 (3 1968), pp. 873–880. DOI: 10.1103/PhysRev.173.873. URL: https://link.aps.org/doi/10.1103/PhysRev.173.873.

[62] Juris Meija, Tyler B. Coplen, Michael Berglund, Willi A. Brand, Paul De Bièvre, Manfred Gröning, Norman E. Holden, Johanna Irrgeher, Robert D. Loss, Thomas Wal-

czyk, and Thomas Prohaska. “Isotopic compositions of the elements 2013 (IUPAC Technical Report).” In: *Pure and Applied Chemistry* 88.3 (2016), pp. 293–306. DOI: doi:10.1515/pac-2015-0503. URL: https://doi.org/10.1515/pac-2015-0503.

[63] Robin K Harris, Edwin D Becker, Sonia M Cabral de Menezes, Robin Goodfellow, and Pierre Granger. “NMR Nomenclature: Nuclear Spin Properties and Conventions for Chemical Shifts: IUPAC Recommendations 2001.” In: *Solid State Nuclear Magnetic Resonance* 22.4 (2002), pp. 458–483. ISSN: 0926-2040. DOI: https://doi.org/10.1006/snmr.2002.0063. URL: https://www.sciencedirect.com/science/article/pii/S0926204002900639.

[64] W.M. Haynes. *CRC Handbook of Chemistry and Physics*. CRC Press, 2016. ISBN: 9781498754293.

[65] Gerald L. Pollack. “The Solid State of Rare Gases.” In: *Rev. Mod. Phys.* 36 (3 1964), pp. 748–791. DOI: 10.1103/RevModPhys.36.748. URL: https://link.aps.org/doi/10.1103/RevModPhys.36.748.

[66] Y. Endoh, G. Shirane, and J. Skalyo. “Lattice dynamics of solid neon at 6.5 and 23.7 K.” In: *Phys. Rev. B* 11 (4

1975), pp. 1681–1688. DOI: 10.1103/PhysRevB.11.1681. URL: https://link.aps.org/doi/10.1103/PhysRevB.11.1681.

[67] L. B. Knight Jr., W. C. Easley, W. Weltner Jr., and M. Wilson. "Hyperfine Interaction and Chemical Bonding in MgF, CaF, SrF, and BaF molecules." In: *The Journal of Chemical Physics* 54.1 (1971), pp. 322–329. ISSN: 0021-9606.

[68] Paul H. Kasai, Earl B. Whipple, and William Weltner Jr. "ESR of Cu(NO3)2 and CuF2 Molecules Oriented in Neon and Argon Matrices at 4°K." In: *The Journal of Chemical Physics* 44.7 (1966), pp. 2581–2591. ISSN: 0021-9606.

[69] Youngwook Park, Hani Kang, and Heon Kang. "Brute Force Orientation of Matrix-Isolated Molecules: Reversible Reorientation of Formaldehyde in an Argon Matrix toward Perfect Alignment." en. In: *Angew Chem Int Ed Engl* 56.4 (2016), pp. 1046–1049.

[70] M. Arndt, S. I. Kanorsky, A. Weis, and T. W. Hänsch. "Long Electronic Spin Relaxation Times of Cs Atoms in Solid $^4$He." In: *Phys. Rev. Lett.* 74 (8 1995), pp. 1359–

1362. DOI: 10.1103/PhysRevLett.74.1359. URL: https://link.aps.org/doi/10.1103/PhysRevLett.74.1359.

[71] N. Bar-Gill, L. M. Pham, A. Jarmola, D. Budker, and R. L. Walsworth. "Solid-state electronic spin coherence time approaching one second." In: *Nature Communications* 4.1 (2013), p. 1743. ISSN: 2041-1723.

[72] R. L. Lambo, G. K. Koyanagi, M. Horbatsch, R. Fournier, and E. A. Hessels. "Calculation of the local environment of a barium monofluoride molecule in a neon matrix." In: *Molecular Physics* 121.22 (2023), e2232051. DOI: 10.1080/00268976.2023.2232051. eprint: https://doi.org/10.1080/00268976.2023.2232051. URL: https://doi.org/10.1080/00268976.2023.2232051.

[73] S. Truppe, M. Hambach, S. M. Skoff, N. E. Bulleid, J. S. Bumby, R. J. Hendricks, E. A. Hinds, B. E. Sauer, and M. R. Tarbutt. "A buffer gas beam source for short, intense and slow molecular pulses." In: *Journal of Modern Optics* 65.5-6 (2018), pp. 648–656. DOI: 10.1080/09500340.2017.1384516. eprint: https://doi.org/10.1080/09500340.2017.1384516. URL: https://doi.org/10.1080/09500340.2017.1384516.

[74] A. Marsman, M. Horbatsch, and E. A. Hessels. "Deflection of barium monofluoride molecules using the bichromatic force: A density-matrix simulation." In: *Phys. Rev. A* 108 (1 2023), p. 012811. DOI: 10.1103/PhysRevA.108.012811. URL: https://link.aps.org/doi/10.1103/PhysRevA.108.012811.

[75] A. Marsman, D. Heinrich, M. Horbatsch, and E. A. Hessels. "Large optical forces on a barium monofluoride molecule using laser pulses for absorption and stimulated emission: A full density-matrix simulation." In: *Phys. Rev. A* 107 (3 2023), p. 032811. DOI: 10.1103/PhysRevA.107.032811. URL: https://link.aps.org/doi/10.1103/PhysRevA.107.032811.

[76] H.-M. Yau, Z. Corriveau, N. T. McCall, J. Perez Garcia, D. Heinrich, R. L. Lambo, G. K. Koyanagi, M. C. George, C. H. Storry, M. Horbatsch, and E. A. Hessels. *Specular reflection of polar molecules from a simple multi-cylinder electrostatic mirror: a method for separating BaF molecules produced in a buffer-gas-cooled laser-ablation source from other ablation products*. 2024. arXiv: 2410.04598 [physics.atom-ph].

[77] J. S. Bumby. “Progress towards a source of cold, slow molecules for tests of fundamental physics.” In: 2017.

[78] Moritz Hambach. “Development of a magneto-optical trap for CaF molecules.” In: 2017.

[79] Michael Trigatzis. “An ultracold molecular beam for measuring the electric dipole moment of the electron.” In: 2020.

[80] N. E. Bulleid. “Slow, cold beams of polar molecules for precision measurements.” In: 2013.

[81] Tao Chen, Wenhao Bu, and Bo Yan. “Erratum: Structure, branching ratios, and a laser-cooling scheme for the $^{138}$BaF molecule [Phys. Rev. A 94, 063415 (2016)].” In: *Phys. Rev. A* 100 (2 2019), p. 029901. DOI: 10.1103/PhysRevA.100.029901. URL: https://link.aps.org/doi/10.1103/PhysRevA.100.029901.

[82] Ralf Albrecht, Michael Scharwaechter, Tobias Sixt, Lucas Hofer, and Tim Langen. “Buffer-gas cooling, high-resolution spectroscopy, and optical cycling of barium monofluoride molecules.” In: *Phys. Rev. A* 101 (1 2020), p. 013413. DOI: 10.1103/PhysRevA.101.013413. URL: https://link.aps.org/doi/10.1103/PhysRevA.101.013413.

[83] Wenhao Bu, Yuhe Zhang, Qian Liang, Tao Chen, and Bo Yan. "Saturated absorption spectroscopy of buffer-gas-cooled Barium monofluoride molecules." In: *Frontiers of Physics* 17.6 (2022), p. 62502. ISSN: 2095-0470. DOI: 10.1007/s11467-022-1194-x. URL: https://doi.org/10.1007/s11467-022-1194-x.

[84] S. J. Li, H. D. Ramachandran, R. Anderson, and A. C. Vutha. "Optical control of BaF molecules trapped in neon ice." In: *New Journal of Physics* 25.8 (2023), p. 082001. DOI: 10.1088/1367-2630/ace9f3. URL: https://dx.doi.org/10.1088/1367-2630/ace9f3.

[85] L.-E. Berg, T. Olsson, J.-C. Chanteloup, A. Hishikawa, and P. Royen. "Lifetime measurements of excited molecular states using a Ti:sapphire laser." In: *Molecular Physics* 79.4 (1993), pp. 721–725. eprint: https://doi.org/10.1080/00268979300101571. URL: https://doi.org/10.1080/00268979300101571.

[86] A. Ramsthaler-Sommer, K. E. Eberhardt, and Ulrich Schurath. "Radiative decay and radiationless relaxation of NH/ND(a1) isolated in rare gas matrices." In: *The Journal of Chemical Physics* 85.7 (Oct. 1986), pp. 3760–3769. ISSN: 0021-9606. DOI: 10.1063/1.450949. eprint:

https://pubs.aip.org/aip/jcp/article-pdf/85/7/3760/18960748/3760_1_online.pdf. URL: https://doi.org/10.1063/1.450949.

[87] D. Heinrich, Z. Corriveau, J. Perez Garcia, N.T. McCall, H.-M. Yau, R.L. Lambo, T. Chauhan, G.K. Koyanagi, A. Marsman, M.C. George, C.H. Storry, M. Horbatsch, and E.A. Hessels. "Optical pumping of matrix-isolated barium monofluoride: dependence on the orientation of the BaF molecular axis." In: *arXiv:2410.04605* (2024).

[88] A. Marsman, M. Horbatsch, and E.A. Hessels. (not yet published).

[89] A. Bernè, G. Boato, and M. De Paz. "Experiments on solid argon." In: *Il Nuovo Cimento B (1965-1970)* 46.2 (1966), pp. 182–209. ISSN: 1826-9877.

## COLOPHON

This document was typeset using the typographical look-and-feel `classicthesis` developed by André Miede and Ivo Pletikosić. The style was inspired by Robert Bringhurst's seminal book on typography *"The Elements of Typographic Style"*. `classicthesis` is available for both LaTeX and LyX:

`https://bitbucket.org/amiede/classicthesis/`